

Evaluation of PTPRZ1 and TMEM158 as potential new targets for a CAR-T-Cell-based approach for the treatment of glioblastoma

Dissertation
zur Erlangung des akademischen Grades
Dr. rer. med.
an der Medizinischen Fakultät
der Universität Leipzig

eingereicht von:

Christoph Bach

Geburtsdatum/Geburtsort:

12.01.1990 in Dormagen

Angefertigt am:

Klinik und Poliklinik für Neurochirurgie und dem Fraunhofer-Institut für Zelltherapie und Immunologie IZI

Betreuer:

Prof. Dr. Frank Gaunitz

Dr. Jana Burkhardt

Prof. Dr. Jürgen Meixensberger

Beschluss über die Verleihung des Doktorgrades vom: 19.09.2023

Table of Contents

Table of Contents	2
Abbreviations	5
1 Introduction.....	9
1.1 Glioblastoma	9
1.1.1 Classification and epidemiology	9
1.1.2 Risk factors and symptoms.....	9
1.1.3 Histopathology	10
1.1.4 Molecular pathology	10
1.1.5 Standard treatment.....	11
1.2 Immunotherapies against GBM.....	12
1.2.1 Modern immunotherapy approaches and clinical studies against GBM	12
1.2.2 History and structure of chimeric antigen receptors	13
1.2.3 Clinical studies of CAR therapies	15
1.2.4 Hurdles for treatment of Glioblastoma by immunotherapies	17
1.2.5 Novel targets for CAR therapies against Glioblastoma	17
1.3 PTPRZ1.....	18
1.4 TMEM158	21
2 Aim of the work.....	24
3 Materials & Methods	25
3.1 Materials.....	25
3.1.1 Chemicals.....	25
3.1.2 Self-made buffers and media	27
3.1.3 Kits	28
3.1.4 Antibodies and labeled peptides.....	29
3.1.5 Important devices.....	30
3.1.6 Cells and bacteria	31
3.1.7 Enzymes.....	31
3.1.8 Vectors.....	32
3.1.9 Primer (Supplier: Eurofins Genomics, Ebersberg, Germany)	32
3.1.10 Consumables	32
3.2 <i>In silico</i> analysis of public gene expression data	33
3.3 Cultivation of adherent cell lines.....	33
3.4 Freezing and thawing of cells	34
3.5 Purification of RNA and cDNA synthesis	35
3.6 Real-time quantitative PCR	36

3.7	Protein extraction and BCA assay.....	36
3.8	SDS-PAGE and Western Blot.....	37
3.9	Knockdown of TMEM158	38
3.10	Flow cytometric analysis of cell surface proteins.....	39
3.11	Restriction digestion, agarose gel electrophoresis and gel-extraction of plasmid DNA	40
3.12	Ligation and transformation of chemo-competent bacteria	41
3.13	Identification of clones with correct plasmids	42
3.14	Site-directed mutagenesis.....	43
3.15	Isolation of plasmid DNA in 300 ml scale (Maxiprep)	44
3.16	Recombinant TMEM158-hFc production and peptide binding assays	45
3.17	Peptide binding assay.....	47
3.18	Design and cloning of CAR.....	48
3.19	Production of viral particles	51
3.20	Virus titration	52
3.21	Stimulation, transduction and cultivation of PBMC and primary T cells	53
3.22	Luciferase-based cytotoxicity assay	54
3.23	Statistics and software	55
4	Results	56
4.1	Gene-expression, patient survival and stem cell marker correlation in public expression datasets of <i>TMEM158</i>	56
4.2	Gene-expression analysis of <i>TMEM158</i> in a clinically relevant patient subgroup.....	58
4.3	Gene-expression, patient survival and stem cell marker correlation in public expression datasets of <i>PTPRZ1</i>	60
4.4	Gene-expression analysis of <i>PTPRZ1</i> in a clinically relevant patient subgroup	61
4.5	Protein expression and knockdown of TMEM153 expression in GBM cell lines	63
4.6	Binding of BINP to GBM cell lines.....	65
4.7	Protein expression of integrin $\alpha V\beta 3$ on GBM cell lines.....	68
4.8	Production of recombinant TMEM158-hFc protein and binding by BINP	69
4.9	Production of BINP-CAR-T cells and their transduction efficiency.....	71
4.10	Cytotoxicity of BINP-CAR-T cells against cell lines.....	73
5	Discussion	79
5.1	Gene- and protein-expression of <i>TMEM158</i>	79
5.2	Production of recombinant TMEM158	81
5.3	Production and cytotoxicity of BINP-CAR-T cells.....	82
5.4	Gene- and protein-expression of <i>PTPRZ1</i>	87
5.5	Outlook.....	89
6	Summary.....	92

7	References.....	95
8	Appendix.....	113
8.1	Maps of lentiviral packaging vectors.....	113
8.2	Expression of TMEM158 and PTPRZ1 in glioma and non-glioma tumor entities and overall survival in GBM.....	114
8.3	Titration of anti-TMEM158 Western blot antibodies.....	115
8.4	Western Blot of TMEM158 before and after deglycosylation	116
8.5	Histograms of flow cytometry measurements of BINP and scBINP stained T98G cells at different time points after staining	117
8.6	Flow cytometry analysis of TMEM158 knockdown.....	118
8.7	Cytotoxicity of BINP-WT-CAR-T cells against non-brain tumor cell lines	119
8.8	Murine model of GBM and targeting by BINP-CAR-T cells.....	120
8.9	Modelling of BINP binding to TMEM158.....	121
8.10	Alignment of human and murine TMEM158 sequence	122
8.11	Murine model of GBM and targeting by anti-PTPRZ1-CAR-T cells.....	123
9	List of Tables.....	124
10	List of Figures.....	124
11	Declaration of independent work	130
12	Curriculum vitae	131
13	List of publications.....	133
14	Acknowledgements	134

Abbreviations

(T)-flask	tissue flask
aHER2	anti-human epidermal growth factor receptor 2
ALK	anaplastic lymphoma kinase
AMPA	α -amino-3-hydroxy-5-methyl-4-isoxazolepropionic acid receptors
ANOVA	analysis of variance
APC	allophycocyanin
APS	ammonium persulfate
ATCC	American Type Culture Collection
B7-H3	B7 homolog 3 protein
BCAT1	branched-chain amino acid transaminase 1
BCMA	B cell maturation antigen
BINP	brain injury-derived neurotrophic peptide
BSA	bovine serum albumin
CAIX	carbonic anhydrase IX
CAR	chimeric antigen receptors
CD	cluster of differentiation
cDNA	complementary DNA
CM	co-stimulatory molecule
CMV	cytomegalovirus
CRC	colorectal carcinoma
CS	chondroitin sulfate
CSPG4	chondroitin sulfate proteoglycan 4
Ct	cycle of threshold
CTLA	cytotoxic T-lymphocyte-associated
DC	dendritic cells
DFS	disease-free survival
DLBCL	diffuse large B-cell lymphoma
DMEM	Dulbecco's Modified Eagle Medium
DNA	deoxyribonucleic acid
dNTP	deoxynucleoside triphosphate
DPBS	Dulbecco's phosphate-buffered saline
DsiRNA	double stranded small interfering RNA
DSMZ	German Collection of Microorganisms and Cell cultures
E:T	effector-to-target
EDTA	ethylenediaminetetraacetic acid
EF1a	elongation factor 1a
EGFR	epidermal growth factor receptor
EMT	epithelial–mesenchymal transition
EphA2	ephrin type-A receptor 2
ErbB2	erb-b2 receptor tyrosine kinase
FACS	fluorescence activated cell sorting
FAK	focal adhesion kinase
FBS	fetal bovine serum

Fc	fraction crystallizable
FC	flow cytometry
FGF	fibroblast growth factor
FGFR	fibroblast Growth Factor Receptor
FITC	fluorescein isothiocyanate
FNIII	fibronectin III
FPKM	fragments per kilobase of exon per million
FSC	forward scatter
GAPDH	glyceraldehyde 3-phosphate dehydrogenase
GBM	glioblastoma
GEPIA	gene Expression Profiling Interactive Analysis
GTEx	genotype-Tissue Expression
HB-GAM	heparin-binding growth-associated molecule
HE	haematoxylin and eosin
HEPES	4-(2-hydroxyethyl)-1-piperazineethanesulfonic acid
HIF	hypoxia-inducible factor
HR	hazard ratio
hFc	human fraction crystallizable
IDH	isocitrate-dehydrogenase 1
IgG	immunoglobulin G
IL	interleukin
IL13R α 2	interleukin-13 receptor subunit alpha-2
ITAM	immunoreceptor tyrosine-based activation motif
JAK	Janus kinase
L1CAM	L1 cell adhesion molecule
LB	lysogeny broth
LC MS	liquid chromatography – mass spectrometry
LGG	low-grade gliomas
MET	N-methyl-N'-nitroso-guanidine human osteosarcoma transforming gene
MFI	median fluorescence intensity
MGMT	O6 Methylguanine DNA Methyltransferase
MHC	major histocompatibility complex
MMP-2	matrix metalloproteinase-2
MOI	multiplicity of infection
MRI	magnetic resonance imaging
mRNA	messenger RNA
NBL	neuroblastoma
NCAM	neural cell adhesion molecule
NEAA	non-essential amino acids
Δ NGFR	truncated p75 nerve growth factor receptor
NMDAR	N-methyl-D-aspartate receptor
NRCAM	neuronal cell adhesion molecule
NRG	NOD rag gamma
NRP1	neuropilin 1

OS	overall survival
P/S	penicillin/streptomycin
p40BBP	40 kDa BINP-binding protein
PAGE	polyacrylamide gel electrophoresis
PBMC	peripheral blood mononuclear cell
PBS	phosphate-buffered saline
PBST	phosphate-buffered saline tween20
PCPG	paraganglioma
PD	programmed cell death protein
PDGFRA	platelet derived growth factor receptor alpha
PE	phycoerythrin
PEI	polyethylenimine
PES	polyethersulfone
PET	positron emission tomography
PFA	paraformaldehyde
PFS	progression-free survival
PI3	phosphoinositide 3
PNGase	peptide-N4-(N-acetyl-beta-glucosaminy)asparagine amidase
PROM1	prominin 1
PTM	post-translational modification
PTN	pleiotrophin
PTPRZ1	receptor type tyrosine-protein phosphatase zeta
PVDF	polyvinylidene difluoride
Rac1	Ras-related C3 botulinum toxin substrate 1
rGBM	recurrent GBM
RGD	glycine/aspartic/arginine acid
RIPA	radioimmunoprecipitation assay (buffer)
RIS1	Ras induced senescence 1
RNA	ribonucleic acid
RPL32	60S ribosomal protein L32
RPMI	Roswell Park Memorial Institute
rSD	robust standard deviation
RTK	receptor tyrosine kinase
RT-qPCR	real-time quantitative polymerase chain reaction
scFv	single chain variable fragments
SDS	sodium dodecyl sulfate
SOC	super optimal broth with catabolite repression
SP	signal peptide
SSC	side scatter
STAT3	signal transducer and activator of transcription 3
TAE	TRIS-acetate-EDTA
TAM	tumor associated macrophages
TARGET	therapeutically applicable research to generate effective treatments
TCGA	the cancer genome atlas
TCR	T cell receptor

TEMED	tetramethylethylenediamine
TG	TRIS/glycine
TGF- β	transforming growth factor β
TGS	TRIS/glycine/SDS
TMEM158	transmembrane protein 158
TMZ	temozolomide
TNBC	triple-negative breast cancer
TNF α	tumor necrosis factor- α
TPM	transcripts per million
TRIS	tris(hydroxymethyl)aminomethane
TRUCK	T cells redirected for universal cytokine-mediated killing
TTF	tumor treating fields
VEGF	vascular endothelial growth factor
WHO	world health organization
WPRE	woodchuck hepatitis virus posttranscriptional response element
WT	wild type

1 Introduction

1.1 Glioblastoma

1.1.1 Classification and epidemiology

Glioblastoma (GBM) is the most frequent and lethal malignant primary brain tumor in adults, accounting for 48.6 % of all malignant gliomas in the US². According to the World Health Organization (WHO), GBM is classified as a grade IV glioma, originally based on histopathological criteria like nuclear atypia, mitotic activity, vascular proliferation, necrosis and proliferative potential. Recently, molecular markers are also taken into account to classify brain tumors (see 1.1.5)². GBM emerges with an incidence of 3.2 per 100,000 population in the USA. In Europe an incidence rate of 3.91 is estimated³. The incidence of GBM is about 1.6-times higher among men than women. GBM is diagnosed at a median age of 65 years with a peak between 75 and 84 years. GBM appears mostly within the frontal lobe (27 %), temporal lobe (20 %) and parietal lobe (13 %)⁴. Less frequently, it is found in the occipital lobe (3 %), spinal cord (4 %) or cerebellum (3 %). In children, GBM often forms in the brainstem.

1.1.2 Risk factors and symptoms

One of the few known risk factors for GBM is ionizing radiation, which is often applied for treatment of other tumors or diseases. Several other environmental factors have been suggested to be associated with formation of GBM but results of studies remain inconclusive thus far, be it exposure to pesticides or vinyl chloride, petroleum refining, smoking or manufacturing of synthetic rubber. Additionally, genetic diseases including neurofibromatosis 1 and 2, tuberous sclerosis, Li-Fraumeni syndrome, retinoblastoma, and Turcot syndrome are associated with an increased risk for development of GBM, although in less than 1 % of GBM patients an underlying hereditary disease has been diagnosed⁵.

Typical first symptoms of GBM include increased intracranial pressure, nausea, headache, vomiting, confusion, memory loss, personality changes and epileptic seizures^{4,6-8}. In the last phase of GBM also drowsiness, dysphagia, progressive neurological and cognitive deficits, incontinence and decrease or loss of consciousness are reported⁹. The cause of death is usually brain herniation, seizure, hemorrhage, cerebral edema or indirectly tumor-related causes as infections or pulmonary embolism^{9,10}.

1.1.3 Histopathology

Characteristic histopathological features of GBM are necrosis and microvascular proliferation¹¹. Further features of GBM and anaplastic gliomas (WHO grade III) are anaplasia, high mitotic rates and invasiveness¹¹. As immunohistochemical markers, glial fibrillary acidic protein is analyzed to confirm astrocytic lineage and MIB-1/Ki-67 is stained to quantify proliferation. Three rare histopathological forms of GBM, gliosarcoma, giant cell glioblastoma and epithelioid glioblastoma, are differentiated by WHO definition. Gliosarcoma is characterized by a metaplastic mesenchymal component¹² while giant cell glioblastoma exhibit multinucleated cells with a diameter of more than 500 μm ¹³. Epithelioid glioblastoma is characterized by large epithelioid cells with abundant eosinophilic cytoplasm, vesicular chromatin, prominent nucleoli and variably present rhabdoid cells¹⁴.

1.1.4 Molecular pathology

The molecular pathology of GBM has gained importance during the last decades with a hope to help determining prognosis and fitting therapeutic approaches⁶. To differentiate between GBM and grade IV astrocytoma, expression of isocitrate-dehydrogenase 1 (IDH) is analyzed. While IDH-wild-type (IDH^{WT}) is found mainly in GBM, a mutated version (IDH^{mut}) is typically found in grade IV astrocytomas that descended from lower grade gliomas. IDH^{mut} is also often found in young patients and is associated with an increased overall survival (OS)¹⁵. Another important molecular marker is the methylation of the O⁶-Methylguanine-DNA Methyltransferase (MGMT) promoter. This deoxyribonucleic acid (DNA)-repair enzyme removes alkyl groups from DNA and thereby undermines the therapeutic effect of alkylating chemotherapeutics like temozolomide (TMZ). Gliomas with an epigenetically silenced MGMT promoter are more susceptible to chemotherapy and show a better response to ionizing radiation¹⁶. Furthermore, 67.3 % of GBMs exhibit mutations in at least one receptor tyrosine kinase (RTK) signaling pathway¹⁷. These pathways are involved in the regulation of cell proliferation, survival, differentiation and angiogenesis^{17,18}. In 57 % of all GBMs, the epidermal growth factor receptor (EGFR) shows either mutations, rearrangements, altered splicing or focal amplification¹⁷.

In addition, mutations are found in Platelet Derived Growth Factor Receptor Alpha (PDGFRA) (13.1 % of GBMs), in the Fibroblast Growth Factor Receptor (FGFR) (3.2 %) and in the N-methyl-N'-nitroso-guanidine human osteosarcoma transforming gene (MET) (1.6 %)¹⁷. Increased protein expression of ERB-B2 receptor tyrosine kinase (ERBB2; HER2/neu), a protein from the EGFR family, was found in 42 % of GBM tissue samples¹⁷. Further mutations are found in the phosphoinositide 3 (PI3)-kinase (25.1 %), in the p110alpha and/or p85alpha subunits (18.3 %) and in other genes of the PI3K family (6.8 %)¹⁷. Moreover, 85.3 % of all GBMs exhibit a dysregulated p53 pathway¹⁷. Additionally, high nuclear protein expression of signal transducer and activator of transcription 3 (STAT3), which is associated with invasion, metastasis, motility of tumor cells and chemoresistance¹⁹⁻²¹ is found in 76.5 % of all GBMs²².

Based on expression of various molecular markers, clustering of GBM into 4 different subtypes, proneural, neural, classical and mesenchymal, was suggested²³. The proneural subtype is found primarily in younger patients, exhibits longer survival but doesn't respond well to chemo- and radiotherapy. The neural subtype was originally associated with good responsiveness to radio- and chemotherapy but lower survival than the proneural subtype. Different studies suggest though that the neural subtype is not a distinct GBM subtype but was identified because of contamination with non-neoplastic brain cells like neurons and oligodendrocytes^{24,25}. The classical and especially the mesenchymal subtype show a significant reduction of mortality after extensive treatment but also exhibit the worst prognosis^{23,26}. In addition, an association of the cancer stem cell marker cluster of differentiation (CD) 133 with the proneural subtype and of CD44 with the mesenchymal subtype has been studied²³.

1.1.5 Standard treatment

Presently, GBM is diagnosed by magnetic resonance imaging (MRI) but is often combined with functional MRI, diffusion-weighted imaging or positron emission tomography (PET)^{27,28}. Patients first undergo a 5-aminolevulinic acid supported microsurgery. When the clinical condition of a patient or location of the tumor prevents standard surgery, stereotactic surgery is performed⁶. Tissue removed during surgery is used for classification and grading according to the WHO criteria and often analyzed for several molecular markers. Following surgery, patients are treated with radiation therapy of up to 60 Gy in combination with TMZ chemotherapy⁶.

Despite this heavy treatment patients show a median OS of just 15.6 months²⁹. Lately, a novel treatment option emerged based on alternating electric fields applied to GBM patients via transducer arrays to interrupt cell cycle during metaphase and thereby induce apoptosis and cell death²⁹. Those tumor treating fields (TTF) can increase the median OS of GBM patients from 15.6 up to 20.5 months²⁹. Currently no curative treatment option is available. Therefore, there is a high unmet need to develop novel therapeutic options.

1.2 Immunotherapies against GBM

1.2.1 Modern immunotherapy approaches and clinical studies against GBM

During the last decade, several different types of immunotherapies were tested clinically for treatment of GBM, which are summarized in the following paragraphs. Peptide vaccines function by priming the adaptive immune system of patients against epitopes of tumor antigens to induce elimination of cancer cells³⁰. The peptide vaccines that were tested in clinical studies so far consisted of 8-30 amino acid long peptides of one or multiple tumor antigens, which aimed to induce an immune response against the corresponding antigens³⁰. Multiple peptide vaccines were shown to be safe and some showed promising efficiency in phase I or II clinical studies, but benefit did not translate into larger phase III clinical studies so far. An EGFRVIII targeting vaccine, rindopepimut, for example showed promising results in phase I studies but no survival benefit was observed in a subsequent phase III study³¹. A different type of vaccine targeting glioblastoma is based on stimulating dendritic cells (DC) of patients with specific tumor antigens or messenger RNA (mRNA)-expressing major histocompatibility complex (MHC) molecules. The main function of DCs is to incorporate antigens and present those to T- and B-cells to induce a potent immune reaction against a presented epitope³². Because of this function, DCs are well-suited to be used for antitumor vaccination³³. For that purpose, DCs are usually harvested from the patient, stimulated *ex vivo* and re-administered to the patient to initiate antigen presentation and stimulate CD4⁺- and CD8⁺-T cells³⁴. In one phase III trial, patients treated with a vaccine based on autologous tumor lysate-pulsed DCs called DCVax®-L, showed a median OS of 23.1 months after surgery, which represents a minor survival benefit³⁵. Several other DC vaccines exhibited promising results in phase I clinical trials, but have yet to be evaluated in phase III studies³⁰.

Another immunotherapeutic approach is to apply lytic viruses to tumor tissue or a resection cavity to eliminate tumor cells and initiate curative inflammation in the region³⁶. Two different oncolytic viruses targeting immunosuppressive myeloid cells, (Toca 511 and Toca FC) or tumor cells directly (FB-111) showed promising results in phase I and phase II studies of recurrent GBM (rGBM) but failed to show benefit for the patients in phase III studies. A different oncolytic virus, DNX-2401, targets integrins on tumor cells via an arginine/glycine/aspartic acid (RGD) motif. In phase I and II studies on rGBM, a survival benefit and immune response was observed for this virus and no dose limiting toxicities were observed and only adverse events lower than grade 3 were seen in 15 % of the patients, though therapeutic benefit has yet to be confirmed in phase III studies³⁷.

A different strategy that might also be combined with other immunotherapies, is blockage of immune checkpoints exploited by tumor cells to inactivate anti-tumor immune response in patients. By blocking receptors like programmed cell death protein (PD) -1 or cytotoxic T-lymphocyte-associated (CTLA) -4, ligands emitted by the tumor cannot bind and thereby inactivate immune cells. Multiple clinical studies showed only a minimal improvement of survival within selected GBM patient subgroups at best³⁸. Also, significant adverse events of grade 3 and 4 were observed in some patients when an anti-PD-1- and an anti-CTLA-4 antibody were combined³⁸.

Taken together, many different kinds of immunotherapies were developed during the last decades and some showed an encouraging benefit for patients in early studies but so far most of them failed to reproduce the effect when analyzed in larger phase III trials. Because of this, novel therapies for the treatment of this devastating disease are still urgently needed.

1.2.2 History and structure of chimeric antigen receptors

A novel and effective form of immunotherapy is based on chimeric antigen receptors (CARs) that are introduced into immune cells to retarget their function towards tumor cells³⁹. The original idea behind this approach was to combine the function of a T cell receptor (TCR) with the specificity of antibodies.

By fusing single chain variable fragments (scFv), which are functional fusion proteins of the variable regions of the heavy and light chain of immunoglobulins, connected by a short peptide linker⁴⁰, with a signal transducing subunit of immunoglobulin- or T cell receptors, chimeric TCRs, also called T-Bodies, were generated³⁹. By adding a flexible spacer between antigen binding domain and signaling domain, the function of those chimeric receptors was enhanced⁴¹. This structure is nowadays referred to as first-generation of CAR (Figure 1).

In contrast to TCRs, CARs can function unrestricted from MHC, but can only recognize surface proteins and not peptide epitopes presented by cells via the MHC pathway³⁹. Downregulation of MHC-1 molecules is a common mechanism of tumor cells to escape T cell recognition that is found in 40-90 % of tumors^{42,43}. By arming T cells with CARs, this escape mechanism can be counteracted. A second-generation of CARs, which enables enhanced cell proliferation and cytokine production was generated by adding a CD28⁴⁴ or CD137 (4-1BB)⁴⁵ domain to the intracellular domain of CARs. CARs equipped with CD28 usually exhibit a more robust proliferation, whereas CARs equipped with CD137 show greater persistence and central memory differentiation⁴⁶. To further increase persistence of CAR cells, CD28 and CD137⁴⁷ or CD134 (OX-40)⁴⁸ were both integrated to the intracellular part of the CARs, which are then referred to as third-generation CAR. A fourth-generation of CARs was developed, which enable cells to release cytokines like interleukin (IL)-12 when activated⁴⁹. These constructs were also called "T cells redirected for universal cytokine-mediated killing" (TRUCK) and boost the function of CAR cells and also unmodified immune cells of the patient⁴⁹. Lately, a fifth-generation CAR was suggested that exhibits a truncated IL-2R β and STAT3-binding domain additional to the CD28 and CD3 ζ signaling domains. Using this design, CARs are able to activate the Janus kinase (JAK)-STAT3/5 pathway that further increases proliferation and prevents terminal differentiation *in vitro*⁵⁰. So far, an advantage of this approach was only shown to second-generation CARs. In addition to the different generations of CARs that only differ in their stimulatory domains, several other structural factors have been described, which influence the function of a CAR. It was shown that the affinity of the antigen binding domain strongly influences the CAR-cell function. In multiple studies, a high affinity CAR induced higher cytotoxicity in comparison with CARs with lower affinity against the same molecular target *in vitro*. But in a proliferation assay and *in vivo*, a CAR with a high but not the highest affinity showed the highest proliferation or *in vivo* efficiency.⁵¹⁻⁵³

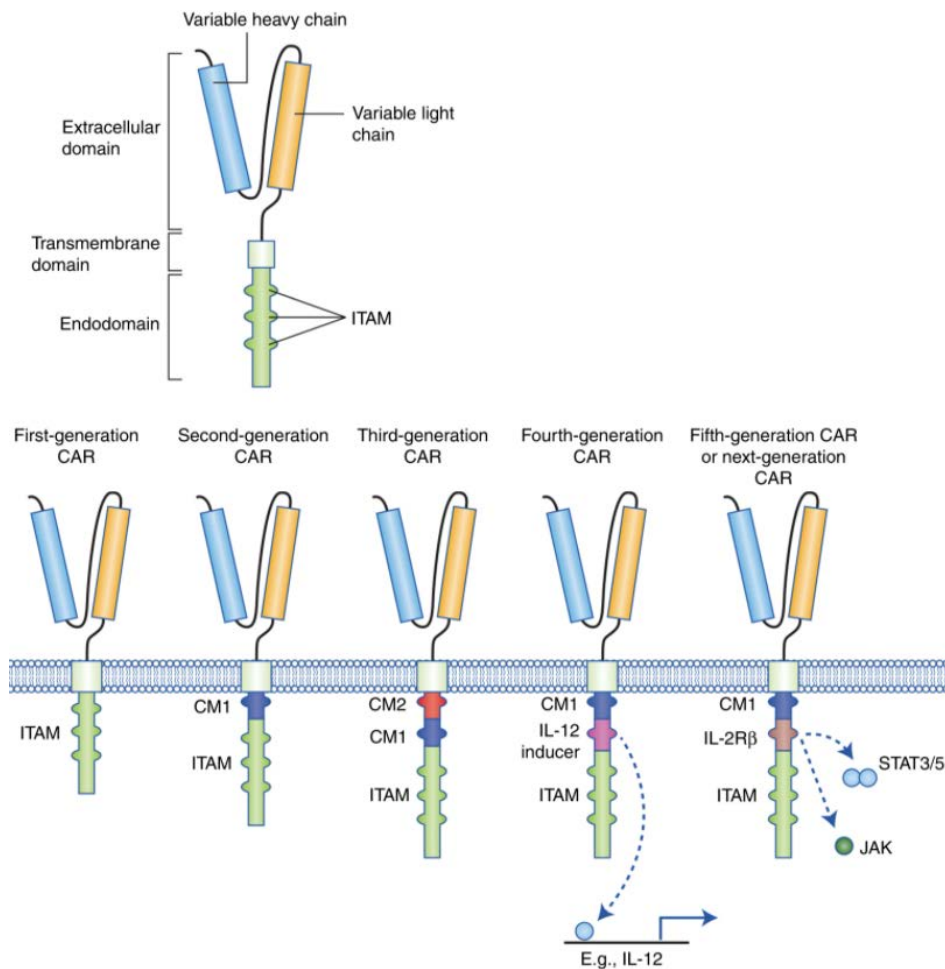


Figure 1: Structure of different CAR generations. Upper scheme: Elements of a first-generation CAR, consisting of an extracellular domain that binds to a target antigen, an intracellular domain that mediates activation of the immune cell after antigen binding and a transmembrane domain that links the extra and the intracellular domain. Lower scheme: Differences in structure of the five different CAR generations. Additional co-stimulatory domains were added to the first-generation CAR to increase proliferation and persistence of CAR cells and to protect them against the immunosuppressive tumor microenvironment to some extent. CAR, chimeric antigen receptor; CM, co-stimulatory molecule; IL-12, Interleukin-12; IL-2R β , Interleukin-2 receptor β ; ITAM, immunoreceptor tyrosine-based activation motif; JAK, Janus kinase; STAT, Signal transducer and activator of transcription¹.

1.2.3 Clinical studies of CAR therapies

During the last years, several CAR-therapies were approved for treatment of patients in the USA and Europe. So far, all approved CAR-T cell therapeutics are second-generation CARs. KymriahTM and YescartaTM were the first approved CAR-T cell therapeutics and target CD19 positive cells to treat patients with relapsed or refractory diffuse large B-cell lymphoma (DLBCL) and other forms of hematologic cancers.

An anti-CD19 CAR-T cell therapy that also uses CD137 for co-stimulation, namely Breyanzi™, was approved recently and can also be applied for patients that only received one treatment prior to the CAR-Therapy, in contrast to other CAR-therapies. In addition, two CAR-T cell therapeutics, namely TECARTUS™ and ABECMA™ were approved, which both use CD28 for co-stimulation and target CD19 or the B-cell maturation antigen (BCMA). Both therapeutics, TECARTUS™ and ABECMA™, were approved for treatment of patients with relapsed or refractory mantle cell lymphoma or relapsed or refractory multiple myeloma, respectively.

In contrast to therapies for treatment of hematologic cancers that reached more than 85 % of complete response in many studies⁵⁴, only small benefits were observed in studies of CAR-T cells against glioblastoma so far. In two phase I clinical trials Interleukin-13 receptor subunit alpha-2 (IL-13R α 2), which is highly expressed in about 38 % of GBMs⁵⁵, was targeted by first-⁵⁶ or second-generation⁵⁷ CAR-T cells in three⁵⁶ or one⁵⁷ patients with recurrent GBM, respectively. Although signs of tumor response were observed, only a median survival of 11 months after relapse was observed in the three patients treated with the first-generation CAR-T cells. Different grade 3 adverse effects were noticed after administration of 10^8 of the first-generation CAR-T cells but not for lower amounts of cells or the second-generation CAR-T cells^{56,57}. In a phase I study targeting ERBB2 (HER2) with second-generation CAR-T cells in 17 patients, a median OS of 24.5 months after diagnosis and 11.1 months after the first CAR-T cell injection was achieved. The study also included 7 young patients, ranging between 10 and 17 years (median age 14), which might have influenced the OS outcome of this single-arm study compared to historical OS result according to the authors of the study⁵⁸. No adverse effects of grade 3 or higher were observed. Furthermore, a phase I trial using a second-generation CAR targeting EGFRvIII which is expressed in about 38 % of GBMs⁵⁹ was conducted with 10 patients. A single dose of 5×10^8 cells was injected peripheral but only a median survival of 8 months after CAR treatment was reached. Adverse events of grade 3 were observed in several patients and in two patients grade 4 events were seen⁶⁰. Recently, CAR-T cells against Ephrin type-A receptor 2 (EphA2) were applied intravenously into three patients. Overall survival of these patients ranged only between 86 and 181 days. Two of the patients suffered from grade 2 cytokine release syndrome and pulmonary edema that might have been related to on-target-off-tumor effects according to the authors⁶¹.

Despite targeting a variety of GBM-antigens by CAR-therapies, no success comparable to the treatment of hematologic cancers was achieved, indicating that additional limitations need to be overcome.

1.2.4 Hurdles for treatment of Glioblastoma by immunotherapies

So far, success of CAR therapies was observed treating hematologic cancers. However, barely any therapeutic benefit was achieved by treating solid tumors such as GBM⁶². Main hurdles impeding efficient CAR-cell function are thought to be inter- and intratumoral antigen heterogeneity, an immunosuppressive tumor-microenvironment and inadequate migration as well as invasion of CAR-cells into the tumor⁶³. Especially GBM shows an enormous phenotypic and genetic heterogeneity and is one of the clinically most challenging solid cancers^{62,64}. To counteract antigen heterogeneity, targeting of multiple marker proteins in parallel seems to be a promising approach. It was shown that targeting of HER2, IL-13R α 2 and EphA2 in parallel eliminated nearly 100 % of GBM cells in an orthotopic patient derived xenograft (PDX) GBM animal model. Although it has to be noted that in this study tissue from patients with favorable expression profiles was selected for exhibiting at least one of the targeted antigens significantly on each cell⁶⁵. For a similar treatment of a wide range of patients with differing antigenic profiles the identification and combination of more antigens is most likely needed⁶⁶.

1.2.5 Novel targets for CAR therapies against Glioblastoma

In view of this drastic need for novel antigens and the poor outcome of clinical approaches for a CAR-T therapy of GBM so far, one of the central issues is to find appropriate targets for the development of new therapeutic strategies. Therefore, different antigens have been investigated showing promising results in pre-clinical studies. Nearly all of the targets investigated also displayed a negative correlation with survival and were found in multiple tumor entities:

B7 homolog 3 protein (B7-H3) was shown to be overexpressed in multiple tumor types, including GBM and is expressed in 58 %⁶⁷ to 76 %⁶⁸ of clinical glioma samples. The receptor and function of this target remain mostly unknown so far⁶⁷. In addition, carbonic anhydrase IX (CAIX), which is expressed in 60 % of resected GBM samples⁶⁹, and which is highly expressed under hypoxic conditions, was targeted in a study and possibly holds great potential as a GBM specific antigen.

EphA2 was found to be expressed with a moderate to strong extend in more than 90 % of GBM tissue samples and several GBM cell lines^{70,71}, but suitability as a target might hinge on on-target-off-tumor adverse events as stated above. Chondroitin sulfate proteoglycan 4 (CSPG4) is another target that was highly expressed in 31 of 46 GBM tissue samples and seems to be induced by tumor necrosis factor- α (TNF α) released by microglia. In one study, targeting of this antigen did not lead to antigen loss, although recurrence was still detected⁷². An antigen that is associated with GBM initiation and is regarded as GBM stem cell marker, CD133 (Prominin 1, PROM1), is found in 78.7 % of tumors on the mRNA level⁷³. However, targeting of this protein marker *in vitro* seemed to induce upregulation of CD57 on CAR-T cells, which is a marker for terminal differentiation of T cells and senescence⁷⁴. Furthermore, a CAR against the integrin α V β 3 was developed⁷⁵, as it was shown that this target is overexpressed in 7 out of 7 GBM patients in comparison to normal brain tissue of the same patients⁷⁶. This CAR efficiently treated metastatic melanoma in a murine xenograft model but was not evaluated in a glioblastoma model so far⁷⁵. A novel CAR, applying the chlorotoxin peptide as binding domain, showed promising efficiency in an orthotopic PDX model of GBM and did not seem to induce antigen loss⁷⁷. The receptor of chlorotoxin is not conclusively confirmed, but strong evidence suggests either matrix metalloproteinase-2 (MMP-2)⁷⁷ or neuropilin 1 (NRP1)⁷⁸. Nonetheless, using fluorescence-labeled chlorotoxin, over 90 % of patient samples stained positive with more than 80 % positive cells per tumor. To further broaden the spectrum of targetable GBM antigens, two new targets, namely PTPRZ1 and TMEM158, were investigated in the present dissertation to evaluate their potential use for anti-GBM CAR-T cell therapy.

1.3 PTPRZ1

Receptor-type tyrosine-protein phosphatase zeta (PTPRZ1) belongs to the R5 subfamily of the receptor tyrosine phosphatase family⁷⁹. Initially, three different splice variants of PTPRZ1 were described, two transmembrane variants (PTPRZ-A and PTPRZ-B) and one secreted extracellular variant (PTPRZ-S, long and short) also known as phosphacan^{80–82}(Figure 2). A short isoform of PTPRZ-S was also identified in mice that might be a proteolytic breakdown product of the PTPRZ-A or the long PTPRZ-S isoform⁸³.

Also transmembrane variants of PTPRZ were identified that exhibit a deletion in exon 16, called PTPRZ-B- or PTPRZ-A Δ ex16 and show a higher catalytic activity⁸². All isoforms of PTPRZ were reported to be post-translationally modified with chondroitin sulfate (CS) and PTPRZ-A and -S (long) are additionally modified with keratan sulfate, while only the short form of PTPRZ-S seems to be not modified with any of those modifications^{83,84}. The structure of the different PTPRZ isoforms is shown in Figure 2. PTPRZ-A and -B are expressed in neurons and radial glia during development of the brain, while phosphacan and PTPRZ-B were found predominantly in the murine adult brain^{84–86}.

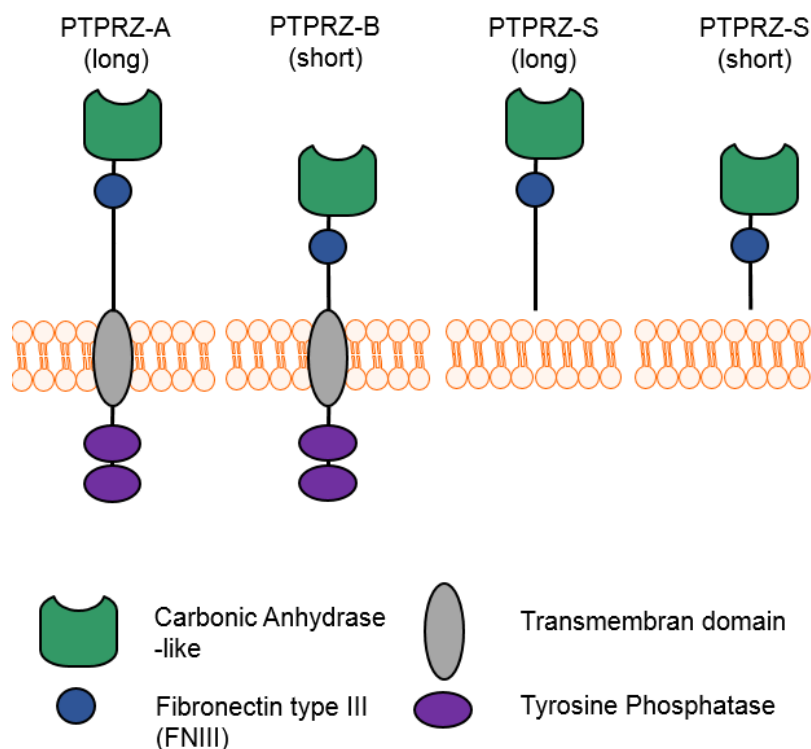


Figure 2: Isoforms of PTPRZ1 and Phosphacan. Shown is the structure of the two main transmembrane variants of PTPRZ1 as well as the two different soluble isoforms, called PTPRZ-S or phosphacan.

Overexpression of *PTPRZ1* in GBM tissues was shown by complementary DNA (cDNA) arrays and liquid chromatography – mass spectrometry (LC-MS) analysis^{87,88}. In addition, immunohistochemical analysis revealed that 16 out of 24 glioblastoma tumors (66 %) stained positive for PTPRZ-A and -B, whereas none of 4 investigated normal brain tissues were positive. In the same study, it was found that nearly all samples expressed both isoforms⁸⁹.

PTPRZ1 expression also negatively correlated with survival of GBM patients^{90,91}. Furthermore, overexpression of *PTPRZ1* was identified in a multitude of other cancer entities, namely breast cancer^{92,93}, lymphoma⁹⁴, ovarian cancer⁹⁵, small-cell lung carcinoma⁹⁶, melanoma⁹⁷, oral squamous cell carcinoma⁹⁸, pancreatic cancer⁹⁹, meningioma¹⁰⁰, gastric cancer¹⁰¹, colon adenocarcinoma¹⁰² and neuroblastoma⁹⁷. Protein expression of PTPRZ1 was also shown in tissue micro arrays of most of the above-mentioned tumor entities and others, although for some tumor entities protein expression levels were only found in few patients. Only in few subsets of normal tissue a corresponding signal was detected¹⁰³. In case of triple-negative breast cancer (TNBC), upregulation of PTPRZ1 and pleiotrophin was found in patients that received chemotherapy and in TNBC cell lines that were treated with doxorubicin⁹².

Several ligands of PTPRZ1 have been described so far, including cell adhesion molecules such as neuronal cell adhesion molecule (NRCAM), L1 cell adhesion molecule (L1CAM), F3/contactin, neural cell adhesion molecule (NCAM) and TAG1/axonin-1. In addition, growth factors such as pleiotrophin (PTN), midkine, heparin-binding growth-associated molecule (HB-GAM) and fibroblast growth factor (FGF)-2, as well as extracellular matrix molecules like tenascin-C and tenascin-R appear to be ligands^{80,86,104–106}.

Multiple studies analyzed the function of PTPRZ1 performing knockdown in tumor cells. In one study it was found that expression of several stem cell transcription factors was altered by knockdown and sphere-forming abilities were decreased. Because of this, a function of PTPRZ1 in maintaining stem-like properties of GBM cells was hypothesized¹⁰⁷.

It was also demonstrated that PTPRZ1 knockdown significantly decreased tumor growth and reduced migration *in vitro* and *in vivo*^{87,108}. A later study confirmed that an isoform of pleiotrophin 15 promotes glioblastoma proliferation in dependency of anaplastic lymphoma kinase (ALK), whereas immobilization of PTN18 by interaction with PTPRZ1 facilitates haptotactic migration of GBM cells¹⁰⁹. Furthermore, it was found that pleiotrophin is secreted by tumor associated macrophages (TAM), which might lead to malignant growth of GBM via the PTN-PTPRZ1 axis⁹⁰. Interestingly, it was also shown that PTPRZ1 is inactivated by binding to PTN15, which is positively charged, allowing interaction with the negatively charged CS-chains of PTPRZ1, resulting in dimerization and clustering¹¹⁰.

Tenascin-c, another likely ligand of PTPRZ1, binds to the protein via its fibronectin III (FNIII) domain repeats A1-A4 and was shown to mediate cell adhesion and spreading of an astrocytoma cell line¹¹¹. The FNIII domain contains the common arginine-glycine-aspartate (RGD) motif that is found in matrix proteins and promotes binding to cell surface proteins like integrins¹¹²⁻¹¹⁴. One study reports that a conservative amino acid shift from RGD to RGE completely disrupts the binding of integrins to this motif¹¹³.

Based on the previous findings, various therapeutic approaches, including small molecules¹¹⁵, antibodies¹⁰³ and peptide-based vaccines^{88,116,117}, targeting PTPRZ1 have been developed and for the most part showed encouraging results in pre-clinical studies. However, none of these therapeutics have been tested in clinical studies against GBM, yet.

1.4 TMEM158

Transmembrane protein (TMEM) 158 is a dual-pass membrane protein with unclear function (Figure 3). It was first identified by cross-linking to a newly identified neurotrophic peptide called brain injury-derived neurotrophic peptide (BINP). This peptide was identified by isolation from a sponge gelfoam that was implanted into injured rat brains¹¹⁸. In cell cultures, it promotes survival of septal cholinergic and mesencephalic dopaminergic neurons and rescued hippocampal neurons from glutamate induced excitotoxicity¹¹⁸. By exchanging each amino acid of this peptide individually with glycine, it was suggested that this peptide has an α -helical conformation and that amino acids on the hydrophobic side of the peptide are involved in its neurotrophic activity¹¹⁹. Further studies also showed binding to hippocampal and septal rat synaptosomes and identified TMEM158, without giving it a name at this point, as binding partner of BINP by cross-linking TMEM158 to a radiolabeled version of BINP and analyzing band size after gelelectrophoresis¹²⁰. A monoclonal antibody against TMEM158 was developed, used for blocking of the protective effect of BINP and also used for immunoprecipitation of TMEM158¹²¹. In this study, it was also shown that the cell line NG108-15, which is a neuroblastoma x glioblastoma fusion cell line, expressed TMEM158. Furthermore, the recombinant TMEM158 could be expressed in COS7 cells and was called 40 kDa BINP-binding protein (p40BBP). In immunohistochemical studies, protein expression of TMEM158 was increased in hippocampal rat neurons after treatment with kainic acid or the neurotoxic substance lasalocid¹²².

Independent of the research on p40BBP, TMEM158 was identified during a microarray-based search for up-regulated genes in Ras-senescent fibroblasts and was therefore called Ras-induced senescence 1 (RIS1)¹²³. A function as tumor-suppressor gene was assumed since filters of this array were chosen for identification of such genes, and because it was demonstrated that TMEM158 might be regulated by Ets2, a mediator of Ras-induced senescence¹²³. TMEM158 is also overexpressed in atrophic muscle fibers of old mice and was thus linked to senescence¹²⁴.

However, further studies did not support this sole role of TMEM158^{125,126}. Instead, a role as oncogene was suggested, which is supported by several studies. It was demonstrated that knockdown of TMEM158 significantly decreases invasion, proliferation, tumorigenicity and transforming growth factor (TGF)- β signaling in ovarian-, pancreatic- and triple-negative breast cancer models¹²⁷⁻¹²⁹. Comparable results were found in colorectal carcinoma (CRC), supporting gain-of-function experiments that seem to confirm a role of TMEM158 as an oncogene¹³⁰. Additionally, it was shown that knockdown of TMEM158 significantly decreased chemoresistance against cisplatin in non-small cell lung cancer and CRC^{130,131}. TMEM158 was also shown to be up-regulated in certain triple-negative breast cancer cell lines with high IL-32 expression¹³² as well as in anaplastic thyroid cancer^{133,134}. Very recently, overexpression of TMEM158 in GBM was confirmed *in silico* and experimentally¹³⁵. Expression was highest in high grade gliomas and in a subgroup with wild-type IDH1 specimens. In patients with high TMEM158 expression, lower survival rates were observed. The same authors also demonstrated that knockdown or overexpression of TMEM158 in glioma cell lines reduced or increased proliferation, colony formation, migration and invasion, respectively. It was demonstrated that TMEM158 influences those parameters by induction of STAT3 and epithelial-mesenchymal transition (EMT). Up- or downregulation of TMEM158 in the U-251 MG GBM cell line also influenced tumor growth, invasiveness and survival in a xenograft mouse model¹³⁵.

2 Aim of the work

Glioblastoma is one of the most prevalent, deadly and poorly treatable brain tumors, and new treatment options are urgently needed. Unfortunately, the success of treating hematologic cancers by immunotherapeutic strategies has not been translated successfully to the treatment of GBM thus far. In the case of GBM, a main obstacle is high molecular heterogeneity even within one individual tumor of a patient. Therefore, it has been suggested that targeting multiple antigens at once might be an approach towards the development of new treatment strategies. Towards this purpose, novel targets need to be identified that can be employed for immunotherapy.

Potential GBM targets were identified by our group previously through linking literature search with a datamining strategy of public expression databases. The aim of this project was to evaluate feasibility of one of those candidates for targeting by CAR-T cells, to design and produce CAR-Ts against this target and to demonstrate their cytotoxicity *in vitro*.

The specific aims of this work are:

- To analyze gene-expression of two potential candidate GBM targets, TMEM158 and PTPRZ1, regarding GBM-specific expression, based on *in silico* data.
- Confirm their expression by real-time quantitative polymerase chain reaction (RT-qPCR)-analysis of samples from a local GBM patient cohort and multiple GBM cell lines.
- Analyze protein expression of TMEM158 by Western blot in the same cell lines analyzed by RT-qPCR.
- Demonstrate binding of a natural TMEM158-ligand, called BINP, to GBM cells using flow cytometry, to confirm suitability as a potential target for a CAR-based anti-TMEM158-therapy and usability of BINP for design of an anti-TMEM158-CAR.
- Produce recombinant TMEM158 in 293T cells and used it to further quantify binding of BINP to TMEM158 by a plate-based binding assay.
- Design different versions of an anti-TMEM158-CAR based on BINP, produce CAR-T cells with those constructs, and measure their transduction rates.
- Determine cytotoxicity of those CAR-T cells against GBM cell lines with differing TMEM158 expression to determine function of the individual variants and quantify differences regarding their cytotoxicity.

3 Materials & Methods

3.1 Materials

3.1.1 Chemicals

Name	Supplier, City, Country
1 kb DNA Ladder	New England BioLabs, Frankfurt, Germany
2-propanol	Thermo Fisher Scientific, Waltham, USA
2-mercaptoethanol (55 mM)	Carl Roth, Karlsruhe, Germany
4x Laemmli sample buffer	Bio-Rad Laboratories, Feldkirchen, Germany
4-(2-hydroxyethyl)-1-piperazineethanesulfonic acid (HEPES)	Carl Roth, Karlsruhe, Germany
10x Tris/Glycine/SDS buffer	Bio-Rad Laboratories, Feldkirchen, Germany
10x Tris/Glycine buffer	Bio-Rad Laboratories, Feldkirchen, Germany
50x TAE Electrophoresis buffer	Thermo Fisher Scientific, Waltham, USA
Agarose	Promega, Walldorf, Germany
Agar-Agar	Carl Roth, Karlsruhe, Germany
Albumin fraction V (Bovine serum albumin, BSA)	Carl Roth, Karlsruhe, Germany
Ammonium persulfate (APS)	Carl Roth, Karlsruhe, Germany
Ampicillin sodium salt	Carl Roth, Karlsruhe, Germany
CutSmart® Buffer	New England BioLabs, Frankfurt, Germany
Disodium hydrogen phosphate	Carl Roth, Karlsruhe, Germany
Dry Ice	Sigma-Aldrich, Taufkirchen, Germany
Dulbecco's Modified Eagle Medium (DMEM) (high glucose + pyruvate)	Thermo Fisher Scientific, Waltham, USA
Dulbecco's phosphate-buffered saline (DPBS)	Thermo Fisher Scientific, Waltham, USA

EcoTransfect Transfection Reagent	OZ Bioscience, Marseille, France
Ethylenediaminetetraacetic acid (EDTA) solution pH 8.0	Applichem, Darmstadt, Germany
Ethanol (absolute)	Applichem, Darmstadt, Germany
Fetal bovine serum (FBS)	Thermo Fisher Scientific, Waltham, USA
Fixable Viability Stain 450 (BD)	BD Bioscience, Heidelberg, Germany
Gel Loading Dye, Purple (6X)	New England BioLabs, Frankfurt, Germany
Glycin	Carl Roth, Karlsruhe, Germany
HCl	Carl Roth, Karlsruhe, Germany
Interleukin- 2	Peptotech, Hamburg, Germany
Interleukin- 7	Peptotech, Hamburg, Germany
L-Glutamine (200 mM)	Thermo Fisher Scientific, Waltham, USA
LB-Bouillon (Lennox)	Sigma-Aldrich, Taufkirchen, Germany
Methanol (Western Blot grade)	Carl Roth, Karlsruhe, Germany
Midori Green Advance DNA Stain	NIPPON Genetics, Düren, Germany
MEM Non-essential amino acids (NEAA)	Sigma-Aldrich, Taufkirchen, Germany
Nonfat Dry Milk	Carl Roth, Karlsruhe, Germany
Opti-MEM™ ¹ Reduced Serum Medium	Thermo Fisher Scientific, Waltham, USA
Paraformaldehyde (PFA) 4 %	Morphisto, Offenbach am Main, Germany
Penicillin/Streptomycin (P/S)	Thermo Fisher Scientific, Waltham, USA
Polyethylenimin (PEI)	Sigma-Aldrich, Taufkirchen, Germany
Potassium chloride	Merck, Darmstadt, Germany
Potassium dihydrogen phosphate	Merck, Darmstadt, Germany
Protease Inhibitor Cocktail Set III	Merck, Darmstadt, Germany
Rotiphorese® NF-Acrylamide/Bis-solution 30 % (29:1)	Carl Roth, Karlsruhe, Germany
Radioimmunoprecipitation assay (RIPA) buffer	Thermo Fisher Scientific, Waltham, USA

ROTI®Mark BI-PINK	Carl Roth, Karlsruhe, Germany
Roswell Park Memorial Institute (RPMI) 1640	Thermo Fisher Scientific, Waltham, USA
SOC (super optimal broth with catabolite repression) outgrowth medium	New England BioLabs, Frankfurt, Germany
Sodium bicarbonate	Sigma-Aldrich, Taufkirchen, Germany
Sodium butyrate	Sigma-Aldrich, Taufkirchen, Germany
Sodium carbonate	Merck, Darmstadt, Germany
Sodium chloride	Carl Roth, Karlsruhe, Germany
Sodium dodecyl sulfate (SDS)	Applichem, Darmstadt, Germany
Sodium pyruvate (100 mM)	Sigma-Aldrich, Taufkirchen, Germany
Tetramethylethylenediamine (TEMED)	Carl Roth, Karlsruhe, Germany
tris(hydroxymethyl)aminomethane (TRIS)	Carl Roth, Karlsruhe, Germany
Triton™ X-100	Sigma-Aldrich, Taufkirchen, Germany
Trypane blue	Sigma-Aldrich, Taufkirchen, Germany
Tween® 20	Sigma-Aldrich, Taufkirchen, Germany
Water (demineralized)	inhouse
Water (nuclease-free)	New England BioLabs, Frankfurt, Germany
XenoLight D-luciferin	Perkin Elmer, Rodgau, Germany

3.1.2 Self-made buffers and media

Name	Ingredients
1 M HCl	1 M HCl in water
1 M NaOH	1 M NaOH in water
1 M TRIS-HCl (pH 8.8)	1 M TRIS in water, HCl (pH 8.8)
1 M TRIS-HCl (pH 6.8)	1 M TRIS in water, HCl (pH 6.8)
Ammonium persulfate in water (10 %)	0.1 g/ml ammonium persulfate in water
BSA blocking buffer	0.01 g/ml BSA in PBS (1 %)
Coating buffer (bicarbonate)	100 mM NaHCO ₃ /Na ₂ CO ₃ , pH 9.6
EDTA detaching buffer	5 mM EDTA in DPBS
FC buffer	2.5 mM EDTA and 5 % BSA in DPBS
Fixation buffer	50 % DPBS + 50 % PFA (4 %)

Freezing medium	10 % DMSO in FBS
GBM- / 293T-medium	10 % FBS in DMEM
Lysis buffer	1 % Triton X-100 in PBS with Protease Inhibitor Cocktail Set III (1:200)
Lysogeny broth (LB) medium	0.02 g/ml LB-Bouillon (Lennox) in water
Neutralization buffer	1 M TRIS in water, HCl (pH 8.5)
PBS	137 mM NaCl, 2.7 mM KCl, 10 mM Na ₂ HPO ₄ , 1.8 mM KH ₂ PO ₄
PBST buffer	PBS containing 0.1 % Tween® 20
PEI transfection buffer	0.5 mg/ml polyethylenimine at pH 7 in water
Protein elution buffer	100 mM Glycine in water, HCl (pH 2.5)
Sodium dodecyl sulfate in water (10 %)	0.1 g/ml Sodium dodecyl sulfate in water
T cell complete medium	RPMI 1640, 10 % FBS, 1 % NEAA, 10 mM HEPES, 2 mM L-Glutamine, 1 % P/S, 1 mM Sodium-Pyruvate and 55 mM β-Mercaptoethanol
TAE (Tris-acetate-EDTA) buffer	40 ml 50x TAE Electrophoresis buffer, 1960 ml water
TG buffer	700 ml water, 200 ml methanol, 100 ml 10x Tris/glycine buffer
TGS buffer	900 ml water, 100 ml 10x Tris/Glycine/SDS buffer
TGS with methanol	700 ml water, 200 ml methanol, 100 ml 10x Tris/Glycine/SDS buffer
Western blot blocking buffer	2.5 % Nonfat Dry Milk in PBST

3.1.3 Kits

Name	Supplier, City, Country
5x HOT FIREPol® EvaGreen® qPCR Mix Plus (ROX)	Solis Bio Dyne, Tartu, Estonia
Deoxyribonuclease I (DNase I)	New England BioLabs, Frankfurt, Germany

Monarch® DNA Gel Extraction Kit	New England BioLabs, Frankfurt, Germany
Monarch® Plasmid Miniprep Kit	New England BioLabs, Frankfurt, Germany
Monarch® RNA Cleanup Kit	New England BioLabs, Frankfurt, Germany
Pierce™ BCA Protein assay kit	Thermo Fisher Scientific, Waltham, USA
PrimeScript RT Master Mix	Takara Bio Europe, Saint-Germain-en-Laye, France
Qiagen Plasmid Maxi	Qiagen, Hilden, Germany
QuikChange Lightning Site-Directed Mutagenesis Kit	Agilent, Heilbronn, Germany
T4 DNA Ligase	New England BioLabs, Frankfurt, Germany
TriFECTa DsiRNA Kit (Design ID: hs.Ri.TMEM158.13.1)	Integrated DNA Technologies, Leuven, Belgium

3.1.4 Antibodies and labeled peptides

Name	Supplier, City, Country
anti-integrin α V β 3-antibody (MAB1976)	Merck, Darmstadt, Germany
anti-TMEM158 antibody (ab98335)	Abcam, Cambridge, UK
APC/Cy7 anti-mouse IgG1 Antibody (406619)	Biolegend, Koblenz, Germany
CD271 (LNGFR)-Viobright FITC antibody (130-113-423)	Miltenyi, Bergisch-Gladbach, Germany
GAPDH Loading Control Monoclonal Antibody (GA1R)	ThermoFisher Scientific, Waltham, USA
IRDye® 800CW Goat anti-Rabbit IgG (H+L)	LI-COR Bioscience, Bad Homburg vor der Höhe, Germany
IRDye® 680RD Goat anti-Mouse IgG	LI-COR Bioscience, Bad Homburg vor der Höhe, Germany
pooled IgG from human serum	Merck, Darmstadt, Germany

Rhodamine B-labeled BINP (Sequence: EALELARGAIFQA)	Thermo Fisher Scientific, Waltham, USA
Rhodamine B-labeled scrambled BINP (Sequence: AIALREGFAELAQ)	Thermo Fisher Scientific, Waltham, USA

3.1.5 Important devices

Name	Supplier, City, Country
1 mm glass gel plates	Bio-Rad Laboratories, Feldkirchen, Germany
1 mm comb	Bio-Rad Laboratories, Feldkirchen, Germany
1.5 mm combs	PEQLAB, Erlangen, Germany
BD FACS Canto™II flow cytometer	BD Bioscience, Heidelberg, Germany
Centro XS3 LB 960 plate-reading luminometer	Berthold Technologies, Bad Wildbad, Germany
Drigalski spatula	Carl Roth, Karlsruhe, Germany
Electrophoretic transfer cell	Bio-Rad Laboratories, Feldkirchen, Germany
Electrophoresis chambers	Bio-Rad Laboratories, Feldkirchen, Germany
Foam pad	Bio-Rad Laboratories, Feldkirchen, Germany
Gel chambers (agarose gel)	Bio-Rad Laboratories, Feldkirchen, Germany
Gel documentation system iX20	Intas, Göttingen, Germany
Gel holder cassettes	Bio-Rad Laboratories, Feldkirchen, Germany
Infinite® 200	Tecan, Männedorf, Switzerland
Lightcycler® 480	Roche Diagnostics, Mannheim, Germany
Mr. Frosty™ Freezing container	Thermo Fisher Scientific, Waltham, USA
NanoDrop™ 2000 spectrophotometer	Thermo Fisher Scientific, Waltham, USA

Neubauer improved chamber	Paul Marienfeld, Lauda-Königshofen, Germany
Odyssey Imaging System	LI-COR Bioscience, Bad Homburg vor der Höhe, Germany
QIARack	Qiagen, Hilden, Germany
Universal magnet plate	Promocell, Heidelberg, Germany
UW2070 supersonic system	Bandelin, Berlin, Germany
Vacufuge vacuum concentrator 5301	Eppendorf, Hamburg, Germany

3.1.6 Cells and bacteria

Name	Supplier, City, Country
293T	DSMZ, Braunschweig, Germany
Buffy coat	Institute of Transfusion Medicine Leipzig, Germany
GL-261	DSMZ, Braunschweig, Germany
LN-229	ATCC, Manassas, USA
MZ-18	Provided by Donat Kögel, Frankfurt University Hospital, Germany
NEB® 5-alpha Competent E. coli (High Efficiency)	New England BioLabs, Frankfurt, Germany
SH-SY5Y	DSMZ, Braunschweig, Germany
T98G	ATCC, Manassas, USA
U-87 MG	ATCC, Manassas, USA

3.1.7 Enzymes

Name	Supplier, City, Country
<i>Ascl</i>	New England BioLabs, Frankfurt, Germany
<i>Bam</i>HI	New England BioLabs, Frankfurt, Germany
<i>Nhe</i>I	New England BioLabs, Frankfurt, Germany
Trypsin (0.25 %)	Thermo Fisher Scientific, Waltham, USA

3.1.8 Vectors

Name	Supplier, City, Country
pCCL	Provided by Prof. Jonathan Bramson, McMaster University, Hamilton, Canada
pMDLg/pRRE	Provided by Prof. Jonathan Bramson, McMaster University, Hamilton, Canada
pMD2.G	Provided by Prof. Jonathan Bramson, McMaster University, Hamilton, Canada
pRSV-Rev	Provided by Prof. Jonathan Bramson, McMaster University, Hamilton, Canada

3.1.9 Primer (Supplier: Eurofins Genomics, Ebersberg, Germany)

Name	Sequence
Mut_A9D_f	5'-GGAGTTGGCGAGGGGGGACATATTTTCAGGCGGAAAGC-3'
Mut_A9D_r	5'-GCTTTCCGCCTGAAATATGTCCCCCTCGCCAACCTCC-3'
Mut_G5A_f	5'-CTCGGAGGCGTTGGAGGGTGCAGGGGGGGCGATATTTCC-3'
Mut_G5A_r	5'-GAAATATCGCCCCCTCGCACCTCCAACGCCTCCGAG-3'
Mut_G7A_f	5'-GCGTTGGAGTTGGCGGGAGGGGCGATATTTTCAG-3'
Mut_G7A_r	5'-CTGAAATATCGCCCCCTCCCGCCAACCTCCAACGC-3'
Mut_G11_f	5'-GCGAGGGGGGCGATAGGTCAGGCGGAAAGCAAATATG-3'
Mut_G11A_r	5'-CATATTTGCTTTCCGCCTGACCTATCGCCCCCTCGC-3'
PTPRZ1_f	5'-CATGTAATAGCCCAAACAATCTCC-3'
PTPRZ1_r	5'-TTCTGAAACTCCTCCGCTGAC-3'
RPL32_f	5'-CATCTCCTTCTCGGCATCA-3'
RPL32_r	5'-AACCTGTTGTCAATGCCTC-3'
TMEM158_f	5'-GCTTCCAGTTCCGAAAAGCAG-3'
TMEM158_r	5'-ATGCAATAGAGGGGAAAGGGC-3'

3.1.10 Consumables

Name	Supplier, City, Country
0.45 µm Immun-Blot® Low Fluorescence PVDF-membrane	Bio-Rad Laboratories, Feldkirchen, Germany

384-well plate	Thermo Fisher Scientific, Waltham, USA
96-well plate, flat bottom, white, high-binding (PS)	Greiner Bio-One, Frickenhausen, Germany
Amicon Ultra-15 100 kDa centrifugal filters	Merck, Darmstadt, Germany
Dynabeads™ Human T-Activator CD3/CD28	Thermo Fisher Scientific, Waltham, USA
Filter paper	Bio-Rad Laboratories, Feldkirchen, Germany
Low-retention pipette tips	Biozym, Hessisch Oldendorf, Germany
Magne® Protein A Beads	Promega, Walldorf, Germany

3.2 *In silico* analysis of public gene expression data

In silico analysis of *TMEM158* RNA expression in 518 low-grade gliomas (LGG), 163 GBM tumor tissues and 207 non-malignant brain tissues, obtained from The Cancer Genome Atlas^{136–138} (TCGA) and the Genotype-Tissue Expression^{139,140} (GTEx) projects, was performed using the Gene Expression Profiling Interactive Analysis^{141,142} (GEPIA) tool. GEPIA also allowed analysis and plotting of overall survival or disease-free survival in correlation to low (< median) or high (> median) *TMEM158* expression with CI95 %. Log rank p-values, hazard ratios (HR), and number of patients per cohort are also given. Furthermore, Pearson correlation of *TMEM158* and *CD133* (*PROM1*) or *CD44* expression was calculated and plotted via GEPIA as well.

3.3 Cultivation of adherent cell lines

For analysis of protein- and gene-expression, performance of *in vitro* assays or production of viral vectors and recombinant protein, several cell lines were cultivated. The human GBM cell lines T98G, LN-229 and U-87 MG as well as the murine GBM cell line GL-261, the neuroblastoma cell line SH-SY5Y and the human kidney cell line 293T were obtained from the American Type Culture Collection (ATCC) or from the German Collection of Microorganisms and Cell cultures (DSMZ). The GBM cell line MZ-18 was kindly provided by Donat Kögel.

Adherent cell lines were cultured in high glucose Dulbecco's Modified Eagle's Medium (DMEM) containing 10 % fetal bovine serum (FBS) and pyruvate at 37 °C in a 5 % CO₂-humidified incubator. Adherent cells were cultured either in tissue (T)75-flasks with 12 ml medium or in T175-flasks with 35 ml medium. Cells were split upon confluence at a 1:2 to 1:5 ratio, depending on the growth rate of a cell line. For splitting of cells, medium was aspirated, and cells were washed with 8- or 12 ml Dulbecco's phosphate-buffered saline (DPBS) when cultivated in T75- or T175-flasks, respectively. DPBS was aspirated, 5 or 8 ml of Trypsin was added to a T75- or T175-flask and incubated for 5 minutes at 37 °C and 5 % CO₂. Trypsinization was stopped by adding 5 or 8 ml of medium to a T75- or T175-flask, pipetting up and down and rinsing the bottom wall of the flask. Cell suspension was transferred to a 50 ml-tube (cone shaped) and centrifuged at 300 x g for 5 minutes. Supernatant was discarded and cell pellet was suspended in 10 ml of warm medium.

To determine cell number and vitality, 10 µl of cell suspension was added to a 96-well plate and mixed with 10 µl of Trypan blue. Ten µl of the mixture was added to a Neubauer improved chamber. The number of cells per ml was calculated by multiplying the averaged counted number per large square with the dilution factor and the factor 10,000. For high cell numbers per large square only the four diagonal small squares of each large square were counted and averaged. Vitality was calculated by dividing the number of unstained cells by the total number of counted cells.

An appropriate volume of cell suspension was added to a fresh flask and warm medium was added to a final volume of 12 ml (T75 flask) or 35 ml medium (T175 flask).

3.4 Freezing and thawing of cells

For long-term storage, cells were cryo-conserved in liquid nitrogen. Cells were counted as described above and adjusted to 2 to 40 x 10⁶ cells per ml in culture medium. Into labelled 2-ml-cryo-tubes, 500 µl of cell suspension was added and mixed with 500 µl pre-cooled freezing medium. Cryo-tubes were quickly put into a Mr. Frosty, containing 2-propanol, and put into a -80 °C-freezer. Cryo-tubes with frozen cells were kept in the -80 °C-freezer for 1 to 2 days and were then transferred to cryo-tanks, filled with liquid nitrogen (~-180 °C). To thaw cells, cryo-tubes were transferred from cryo-tanks to dry ice and transported to a water bath. Cryo-tubes were warmed in a 37 °C-warm water bath until all but a small piece of ice was unfrozen.

Meanwhile, a 15-ml-tube was prepared with 10 ml of pre-warmed medium. The tubes were quickly transferred to a sterile bench, while the last piece of ice melted. The unfrozen cell suspension was added slowly to the culture medium and centrifuged for 5 minutes at 300 x g. Then, the supernatant was discarded, the pellet was suspended in 5-10 ml culture medium and added to a T-flask. Culture medium was added to a corresponding volume of the T-flask.

3.5 Purification of RNA and cDNA synthesis

mRNA derived from freshly isolated GBM tumor tissue or cell lines was obtained from the Clinic of Neurosurgery of the University Hospital Leipzig in accordance with the Helsinki Declaration and confirmed by the local committee (#144/08-ek). Tissue was histologically characterized and the statuses of molecular markers (MGMT (in %), IDH (IDH1^{WT} or IDH1^{mut}) and Ki-67 (in %)) were determined at the Department of Neuropathology of the University Hospital Leipzig. The RNA samples were digested with DNase I by adding 5 µg RNA, water (to fill up the volume to 44 µl), 5 µl reaction buffer and 1 µl DNase I into the well of a 96-well plate, and incubation was carried out at 37 °C for 10 minutes. The reaction was stopped by adding 1 µl of 0.5 M Ethylenediaminetetraacetic acid (EDTA) to each well. The mixtures were heat-inactivated at 75 °C for 10 minutes. For RNA purification, the Monarch RNA Cleanup Kit was used. First, 100 µl binding buffer was added to 50 µl of each sample, and then 150 µl ethanol was added. Each sample was added to a column, centrifuged for 1 minute at 16,000 x g, and the flow-through was discarded. The columns were washed by adding 500 µl RNA Cleanup Wash Buffer followed by centrifugation for 1 minute at 16.000 x g. The flow-through was discarded, and samples were washed once more. Then, the columns were transferred to a fresh 1.5 ml tube, and RNA was eluted by adding 10 µl of RNase-free water followed by centrifugation for 1 minute at 16,000 x g. RNA concentrations were measured using a NanoDrop™ 2000 spectrophotometer.

For reverse transcription of RNA into complementary DNA (cDNA), 500 µg RNA and RNase-free water were mixed in a 96-well plate to a final volume of 8 µl, and 2 µl of PrimeScript RT Master Mix were added. The plate was heated up to 37 °C for 15 minutes, followed by 1 minute incubation at 85 °C and was cooled down afterwards to 4 °C for 10 minutes. If not immediately processed further, samples were stored at -20 °C.

3.6 Real-time quantitative PCR

To quantify the expression of *TMEM158* and *PTPRZ1*, a real-time quantitative polymerase chain reaction (RT-qPCR) was performed using a 5x HOT FIREPol® EvaGreen® qPCR Mix Plus (ROX). Two µl of template cDNA was mixed with 30.34 µl water and 0.63 µl of each primer of a primer pair (10 µM) as well as with 8.4 µl of the polymerase master mix. *TMEM158* primers are located within exon 1 (T_m : 60°C) whereas primers for detection of *PTPRZ1* are spanning exon 3 to 4 (T_m 59°C). As reference gene, 60S ribosomal protein L32 (*RPL32*) was used (T_m 58°C). Ten µl of each sample was distributed to one well of a 384-well plate as technical replicate. The plate was heated and measured according to Table 1 by a Lightcycler® 480. The cycle of threshold (Ct) values of technical replicates were normalized to the mean of the reference gene *RPL32* to calculate ΔCt values. To compare subgroups, $\Delta\Delta Ct$ values were calculated by subtracting ΔCt values within each group. Data is depicted as fold change ($2^{\Delta Ct}$). Mann-Whitney U test was used to calculate significance between ΔCt values of groups.

Table 1: Cycling parameters for RT-qPCR

Cycles	Step	Temperature	Time
1	Activation	95 °C	15 seconds
45	Denaturing	95 °C	15 seconds
	Annealing	60 °C	20 seconds
	Extension/Detection	72 °C	1 minute
1	Melting curve, Detection from 60 to 95 °C	95 °C	15 seconds
1		40 °C	1 minute
1		95 °C	15 seconds
1		40 °C	15 seconds

3.7 Protein extraction and BCA assay

Cells growing in a T-flask were washed twice with DPBS, detached from culture plates by scraping and centrifuged at 500 x g for 5 minutes. Cell pellets were then re-suspended in radioimmunoprecipitation assay (RIPA) buffer containing Protease Inhibitor Cocktail Set III at a 1:200 dilution and lysed by sonication.

Therefore, protein samples were sonicated 3-times with 20 pulses each at 80 % intensity using a UW2070 supersonic system. Samples were kept on ice between sonication rounds and were incubated for 20 minutes on ice afterwards. Remaining cell debris was pelleted by centrifugation for 10 minutes at 8000 x g and 4 °C. Protein concentrations were determined using the Pierce™ BCA Protein assay kit. Bovine serum albumin (BSA) standards were prepared by diluting 1 ml of the Kit's BSA in 1 ml RIPA buffer to generate a 1000 µg/ml concentration. Four additional dilutions were produced by sequential two-fold serial dilution. All standard dilutions were stored at -20 °C in aliquots. Reagent A and Reagent B were mixed by pipetting at a 50:1 ratio to prepare a working reagent. On a transparent 96-well flat bottom plate, 25 µl of protein sample or standard-dilution was mixed with 200 µl in duplicates. The plate was incubated at 37 °C for 40 minutes and absorbance at 562 nm was measured with an Infinite® 200 plate reader. A standard curve was generated by plotting the averaged values of the standard-dilutions against their corresponding concentration. Protein concentrations were calculated by subtracting the intercept of the linear part of the standard curve and dividing it by the slope.

3.8 SDS-PAGE and Western Blot

Sodium dodecyl sulfate (SDS) separation gels (12 %) were prepared by mixing 4.1 ml demineralized water, 8 ml Rotiphorese® NF-Acrylamide/Bis-solution 30 % (29:1), 7.5 ml 1M Tris-HCl pH 8.8, 200 µl of 10 % SDS in water, 200 µl 10 % Ammonium persulfate (APS) in water and 20 µl Tetramethylethylenediamine (TEMED) in the given order. Between 1 mm glass gel plates 4 ml of the mixed solution was added without bubbles and 500 µl of 2-propanol was added on top to straighten the surface of the gel and to protect it from oxygen. The gel was left at room temperature for about 30 minutes for polymerization. The stacking gel was produced by mixing 5.2 ml demineralized water, 1.6 ml acrylamide solution, 1.0 ml 1M Tris-HCl pH 6.8, 80 µl 10 % SDS, 80 µl 10 % APS and 8 µl TEMED. Isopropanol was discarded and the solution was added on top of the solid separation gel. A 1 mm comb was added and the gel was left for another 30 minutes at room temperature. The gels, including the glass chambers and the comb, were wrapped with wet paper towels and stored at 4 °C. For SDS-polyacrylamide gel electrophoresis (PAGE), electrophoresis chambers were assembled and filled with pre-cooled TRIS/Glycine/SDS (TGS) buffer.

Protein samples were thawed, the volume containing 10 µg of protein was transferred to a fresh 1.5 ml tube, filled to 21 µl with PBS, and 7 µl of 4x Laemmli sample buffer containing 10 % 2-mercaptoethanol was added. The mixture was incubated at 95 °C for 10 minutes. Samples were cooled on ice for 2 minutes, spun down and transferred to the gel. Five µl of ROTI®Mark BI-PINK was also added onto the gel as size marker. SDS-PAGE was performed at 150 V ($E \sim 15$ V/cm) for 1 hour at room temperature.

A 0.45 µm Immun-Blot® Low Fluorescence polyvinylidene difluoride (PVDF)-membrane was activated by incubating it in a dish with methanol for a few seconds. Gels from the SDS-PAGE were separated from the glass plates. Using gel holder cassettes, a stack consisting of a foam pad, a filter paper, the activated membrane, the SDS-gel, another filter paper, and another foam pad was built in a dish with TRIS/Glycine (TG) buffer. After removal of air bubbles, the cassette was closed and transferred to the electrophoretic transfer cell chamber, filled with pre-cooled TG buffer. Fifty ml of TGS buffer with methanol was additionally added to the loaded electrophoretic transfer cell chamber and electrophoresis was performed at 170 mA for 60 minutes at 4 °C. After electrophoresis, the membranes were washed 5-times for 5 minutes in PBST buffer and blocked for 1 hour with Western blot blocking buffer (dry milk in PBST) at room temperature with agitation at 20 RPM. Then, membranes were incubated overnight at 4 °C with agitation at 20 RPM in blocking buffer containing diluted antibodies (polyclonal anti-TMEM158 antibody (1:1500 or 1:3000) and Glyceraldehyde 3-phosphate dehydrogenase (GAPDH) Loading Control Monoclonal Antibody (1:3000)). Finally, membranes were washed 5-times for 5 minutes with PBST and stained for 1 hour at room temperature with diluted secondary antibodies (IRDye® 800CW Goat anti-Rabbit IgG (H+L) and IRDye® 680RD Goat anti-Mouse IgG (H+L); each diluted 1:10,000). Membranes were scanned using an Odyssey Imaging System.

3.9 Knockdown of TMEM158

To validate staining of TMEM158 on cells by anti-TMEM158 antibodies or BINP, knockdown using the TriFECTa DsiRNA Kit (Design ID: hs.Ri.TMEM158.13.1) was performed. In a 6-well plate, 0.5×10^6 T98G cells were seeded 7 hours before transfection.

A transfection mix consisting of 10 μ l of 0.5 mg/ml polyethylenimine (PEI) at pH 7, 400 μ l Opti-MEM™ I Reduced Serum Medium and 1 μ l double stranded small interfering RNA (DsiRNA) (20 μ M) per well was produced and incubated for 30 minutes at room temperature. Then, medium was aspirated from the 6-well plate, and the transfection mix was carefully added to the wells after inverting it several times. After 16 hours, the transfection mix was replaced by culture medium. Cells were harvested 48 hours after transfection. Cells were either scraped from the plate for the isolation of protein as described in 3.07 or detached using an EDTA-solution and used for flow cytometry as described in 3.10.

3.10 Flow cytometric analysis of cell surface proteins

To analyze cell surface expression of TMEM158 or integrin α V β 3, flow cytometry was applied. For adherent cells, culture medium was aspirated and 10 ml of DPBS was added to wash the cells. DPBS was aspirated and 10 ml of pre-warmed 5 mM EDTA in DPBS was added. The cells were incubated for 5 to 10 minutes in an incubator at culture conditions until most of them detached from the flask. The suspension of detached adherent or cells from suspension culture was transferred to a 50 ml or 15 ml tube, respectively, and centrifuged for 5 minutes at 300 x g. Cells were re-suspended in DPBS depending on the size of the pellet, counted and 0.5 x 10⁶ cells were added per flow cytometry (FC) tube. Three ml of FC buffer were added to each tube and cells were centrifuged as before. Supernatant was discarded and cells for staining with BINP peptides were incubated in 100 μ l 0.25 μ g/ml Fixable Viability Stain 450 to stain dead cells. Cells were washed as before and cells were re-suspended in 100 μ l fixation buffer (or DPBS as control) at room temperature for 5 minutes. For staining of integrin α V β 3 and truncated p75 nerve growth factor receptor (Δ NGFR), no fixation was performed at this point. After fixation, 3 ml of FC buffer was added to each tube for washing. Then, cells were centrifuged as before, and supernatant was discarded. For staining, 100 μ l of Rhodamine B-labeled BINP or -scrambled BINP at 1:25 to 1:200 dilution, anti-integrin α V β 3-antibody at 1:50 to 1:400 dilution or CD271 (LNGFR)-Viobright FITC antibody at 1:50 dilution was added to the cells and vortexed shortly. Cells were incubated for 1 hour at 37 °C (BINP) or room temperature (antibodies) and washed as before. For staining of integrin α V β 3, cells were additionally incubated with 100 μ l allophycocyanin (APC)/Cy7 anti-mouse IgG1 Antibody (Biolegend, Cat. #406619) at 1:250 dilution for 1 hour at room temperature and washed afterwards.

After staining, cells were washed a second time as before to reduce fluorescence background. Fluorescence was measured by a BD FACS Canto™II flow cytometer. Rhodamine B was detected at phycoerythrin (PE) channel. The percentage of singlet cells, positive for the stained protein, as well as median fluorescence intensity (MFI) +/- robust standard deviation (rSD) of positive singlet cells was determined. Samples were measured directly after staining and in indicated experiments after about 30 and/or 60 minutes to find out stability of the BINP binding.

3.11 Restriction digestion, agarose gel electrophoresis and gel-extraction of plasmid DNA

For modification and sub-cloning of existing plasmids, 3 µg of plasmid DNA was first digested in a total volume of 30 µl. Therefore, the corresponding volume of plasmid DNA was added to a 1.5 µl tube and filled with nuclease-free water to a volume of 24 µl. Three µl of CutSmart® Buffer was added and 1.5 µl per enzyme, or 3 µl if only one enzyme was used, was added. The mixture was incubated for 1.5 hours in a heating block at the temperature required for the enzyme used. Meanwhile, a 1 % agarose gel was produced by mixing 150 µl of TAE buffer and 1.5 g of agarose in a beaker and heating at 560 W for 3 minutes in a microwave oven. The solution was left for about 2 minutes to cool and 15 µl of Midori Green Advance DNA Stain was added. The solution was mixed by shaking several times and poured into gel chambers with 1.5 mm combs. The gel was left at room temperature for about 30 minutes to cool down and to solidify. Gels were either used right away or stored in plastic bags with a few ml of TAE buffer in the dark at 4 °C.

One µg of uncut plasmid and 2 µg of a 1 kb DNA Ladder were added to separate 1.5 ml tubes, filled up to a volume of 20 µl with nuclease-free water, and 4 µl of Gel Loading Dye, Purple (6X) was added. Plasmid samples (30 µl) were cooled on ice for 2 minutes after digestion, spun down, and 6 µl of Gel Loading Dye, Purple (6X) was added. All samples, uncut vector and ladder were transferred to a fresh or previously prepared 1 % agarose-gel and electrophoresis was performed for 70 minutes at 120 V (E=7.5 V/cm). Afterwards the DNA bands were visualized using a gel documentation system iX20 and cut from the gels using a scalpel. DNA was extracted from the gel pieces using the Monarch® DNA Gel Extraction Kit. Four volumes of Gel Dissolving Buffer were added to the gel pieces and heated to 50 °C in a heating block and vortexed every two minutes until the gel was completely dissolved.

The solution was transferred to the collection tubes with inserted columns and spun at 16,000 x g in a tabletop centrifuge. Flow-through was discarded, 200 µl of DNA Wash Buffer was added, and the tube was spun as before. The washing step was repeated once more, and columns were transferred to a fresh 1.5 ml tube. Six µl of nuclease-free water, heated to 50 °C was added to the centre of the column membrane and incubated for 1 minute. The tube was centrifuged again as before, and the elution step was repeated once more. DNA concentration was measured with a NanoDrop™ 2000 spectrophotometer at 260 nm.

3.12 Ligation and transformation of chemo-competent bacteria

Plasmid backbone and DNA insert were ligated using the T4 DNA Ligase kit. Therefore, 0.02 pmol of plasmid backbone and 0.06 pmol of DNA insert were added to a 1.5 ml tube and filled up to a volume of 17 µl with nuclease-free water. Two µl of T4 DNA Ligase Buffer (10X) and 1 µl of T4 DNA Ligase were added. The mix was incubated for 1 hour at 22 °C in a heating block. Meanwhile, LB-agar plates containing ampicillin were warmed to room temperature, super optimal broth with catabolite repression (SOC) Outgrowth Medium was pre-warmed to 37 °C, and NEB® 5-alpha Competent *E. coli* (High Efficiency) were thawed on ice. Five µl of the ligation mix was added to a tube of bacteria, mixed slowly by stirring with a pipette tip and incubated for 30 minutes on ice. Bacteria were heat-shocked for 30 seconds at 42 °C and cooled on ice for 2 minutes. Afterwards 100 µl of pre-warmed SOC (without antibiotics) was added, and the bacteria were cultivated for 1 hour at 37 °C at 200 RPM in an incubator. To prepare Lysogeny broth (LB) agar-plates, 500 ml of LB-medium was mixed with 7.5 g agar-agar and heated at 560 W in a microwave oven until it was completely dissolved. The solution was cooled down at room temperature until it was lukewarm but still fluid, and 0.5 ml of 100 mg/ml sterile-filtered ampicillin in water was added. LB-agar was distributed into fresh 90 mm petri dishes. The bacteria suspension was mixed by slow pipetting and 50 µl distributed on an LB-agar plate using a Drigalski spatula. The plates were cultivated overnight at 37 °C. Then, multiple culture tubes with two-point vent stopper with 2.5 ml of LB-media containing ampicillin were inoculated from a single colony, using fresh 10 µl pipette tips for each colony. The cultures were incubated for about 7 hours, and isolation of plasmids was performed using the Monarch® Plasmid Miniprep Kit to purify the DNA. Two ml of the bacterial culture was transferred to a 2 ml tube and centrifuged at 16.000 x g.

Supernatant was discarded, and the pellet was re-suspended in Plasmid Resuspension Buffer (B1) by pipetting. Then, 200 µl of Plasmid Lysis Buffer (B2) was added and each tube was inverted 5-6 times. Afterwards, 400 µl of Plasmid Neutralization Buffer (B3) was added, each tube was mixed by inverting several times and incubated for 2 minutes at room temperature. The suspension was centrifuged for 3 minutes at 16,000 x g. Supernatant was transferred to a column inside a collection tube and centrifuged again for 1 minute as before. Flow-through was discarded, and 200 µl of Plasmid Wash Buffer 1 was added onto the column. The tubes were centrifuged again, flow through was discarded, and the washing step was repeated with 400 µl of Plasmid Wash Buffer 2. Columns were transferred to a fresh 1.5 ml tube, and 30 µl of nuclease-free water was added to the membrane of the column. The tubes were incubated for 1 minute at room temperature and subsequently centrifuged for 1 minute at 16,000 x g. DNA concentrations were measured with a NanoDrop™ 2000 spectrophotometer.

3.13 Identification of clones with correct plasmids

To identify clones with the correct sequence or to validate a plasmids sequence in general, an analytical digest was performed. One µg of each plasmid DNA sample and the parental plasmid was filled up to a volume of 16 µl with nuclease-free water. Two µl of CutSmart® Buffer and 1 µl per enzyme was added to the mix. The mixture was incubated for 1 hour at the appropriate temperature for the enzyme combination and was cooled down on ice afterwards. A new agarose-gel was produced during the incubation time or taken from storage. Digested samples were mixed with 4 µl of Gel Loading Dye, Purple (6X) by pipetting. DNA ladder was prepared as described earlier and all samples, including the DNA ladder, were transferred to the gel. Afterwards, the DNA bands were visualized using an iX20 gel documentation system. Three samples per genetic construct, which showed the expected combination of bands on the analytical gel, were sent to be sequenced by Eurofins Genomics. Therefore, 750 ng of each plasmid was transferred to a fresh 1.5 ml tube and filled up to a volume of 15 µl. Two µl of 10 µM sequencing primer were added to each tube. Sequencing results were analysed by alignment with the corresponding plasmid map using SnapGene.

3.14 Site-directed mutagenesis

To generate mutated versions of the BINP-CAR sequence, inducing an amino acid exchange to alanine at positions L5, R7 or F11 or an exchange at position A9 to aspartic acid, site-directed mutagenesis was performed using the QuikChange Lightning Site-Directed Mutagenesis Kit. Versions of the BINP sequence where positions L5, R7 or F11 were changed to glycine were synthesized by Eurofins Genomics and delivered sub-cloned in pUC57 plasmids. Those constructs were not used within this work but used for the final exchange of those amino acid positions to alanine. For this exchange via the QuikChange Lightning Site-Directed Mutagenesis Kit, 5 μ l of 10x reaction buffer, 1 μ l deoxynucleoside triphosphate (dNTP) mix, 1.5 μ l quick solution, 125 ng of each mutagenesis primer of one primer pair (see 3.1.9) and 25 ng of plasmid template were combined and filled up to 50 μ l with nuclease-free water. Afterwards, 1 μ l of QuikChange Lightning Enzyme was added and the sample was heated in a thermocycler as shown in Table 2. Two μ l of *DpnI* (included in the QuikChange Lightning Site-Directed Mutagenesis Kit) was added to the mix and incubated at 37 °C for 5 minutes to cut methylated DNA. Meanwhile, XL10-Gold Ultracompetent cells were thawed on ice and transferred to a pre-chilled 15 ml tube. Two μ l of the XL10-Gold β -mercaptoethanol mix was added to the cells and swirled gently. Cells were incubated on ice for another 2 minutes and 2 μ l of the *DpnI* treated DNA was added to the cells. The mix was incubated for 30 minutes on ice, heat-pulsed at 42 °C for 30 seconds and incubated on ice for another 2 minutes. To each sample 0.5 ml of preheated SOC medium was added, and the suspension was incubated for 1 hour at 37 °C with shaking at 230 RPM. On two separate agarose plates, 100 μ l and 250 μ l of the bacterial suspension was plated as described in 3.12, respectively. Correct clones were identified by sequencing.

Table 2: Cycling parameters for site-directed mutagenesis

Cycles	Temperature	Time
1	95 °C	2 minutes
18	95 °C	20 seconds
	60 °C	10 seconds
	68 °C	30 seconds/kb: 2 minutes for pUC57 (3.5 kb) 5 minutes for pCCL (10.8 kb)
1	68 °C	5 minutes

3.15 Isolation of plasmid DNA in 300 ml scale (Maxiprep)

To produce larger amounts of plasmid DNA, 300 ml of LB-medium containing ampicillin was inoculated with 150 µl of liquid bacteria cultures harbouring the plasmid of interest. The cultures were shaken overnight at 200 RPM and 37 °C in an incubator. Plasmids were purified using the Qiagen Plasmid Maxi (Qiagen) kit. Bacteria were first pelleted by centrifugation at 6000 x g for 15 minutes at 4 °C, then medium was discarded, and bacteria were re-suspended in 10 ml of Buffer P1 and transferred to a 50 ml tube. Ten ml of Buffer P2 was added, and samples were mixed vigorously by inverting. Ten ml of pre-cooled Buffer P3 was added, samples were mixed again by inverting the tube and incubated on ice for 20 minutes. Samples were centrifuged at 25,000 x g for 45 minutes at 4 °C. Meanwhile, QIAGEN-tip columns were placed in a QIArack, and 10 ml Buffer QBT was added per column for equilibration. Supernatant of the samples was transferred to the columns and allowed to move through it by gravity flow. Fifteen ml of Buffer QC was added to the column two times for washing. DNA was eluted from the columns by placing a 50 ml tube under each column and adding 15 ml of Buffer QF to each column. To the eluted DNA 10.5 ml of isopropanol was added, samples were mixed by inverting the tube and centrifuged at 20,000 x g for 30 minutes at 4 °C. Supernatant was discarded, and precipitated DNA was detached from the wall of the tube with 70 % ethanol by pipetting and transferred to a 2 ml tube.

The tubes were centrifuged for 16,000 x g for 10 minutes, supernatant was discarded and the pellet was dried for 10 minutes in a Vacufuge Vacuum Concentrator 5301 at 6 mbar at room temperature. The DNA was solved in 500 µl nuclease-free water, and concentration was measured with a NanoDrop™ 2000 spectrophotometer. Correct plasmid identity was verified by restriction digestion or sequencing as described in 3.13.

3.16 Recombinant TMEM158-hFc production and peptide binding assays

A genetic construct consisting of the extracellular part of TMEM158 and a human fraction crystallizable (hFc)-tag was designed and synthesized by Eurofins Genomics. It was delivered sub-cloned into a pEX-plasmid containing an ampicillin resistance. The sequence of the TMEM158-hFc was cloned into the pCCL-plasmid as described above (Chapter 3.11 – 3.13), using *Ascl* and *NheI* as enzymes at 37 °C for digestion. A scheme of the pCCL-TMEM158-hFc expression cassette is shown in Figure 4A. The size of the cut pCCL backbone was predicted to be about 9.3 kb, while the size of the CAR-sequence that was cut out should be about 1.6 kb large. The size of each band observed on the gels matched the corresponding predicted size (Figure 4B). The pCCL-TMEM158-hFc plasmid was produced in 300 ml scale (Chapter 3.15) and used for transfection of 293T cells. These cells were chosen as expression system, since TMEM158 was predicted to be a glycoprotein, and the human glycosylation patterns should be preserved on the recombinant protein. 293T cells were thawed and expanded until 10 T175 flasks were at about 80 % confluence. A transfection mix consisting of 240 µl of 0.5 mg/ml polyethylenimine at pH 7, 8 ml Opti-MEM™TM Reduced Serum Media and 60 µg of plasmid DNA was produced and incubated for 30 minutes at room temperature. Meanwhile media of the 293T cells was replaced with 8 ml Opti-MEM™TM Reduced Serum Media. The transfection mix was inverted multiple times after incubation, added to the cells and incubated overnight. Medium was changed to 35 ml culture medium containing 1 mM sodium butyrate and incubated for 3 days. Afterwards, medium was removed, and cells were washed once with 10 ml DPBS. The cells were detached by scraping, transferred to two 50 ml tubes and centrifuged at 500 x g for 5 minutes. Supernatant was discarded, and the pellets were frozen at -80 °C. Five ml lysis buffer containing Protease Inhibitor Cocktail Set III at 1:200 dilution was added to each tube with frozen cell pellet and vortexed every few minutes until it was thawed. Cells were lysed by sonication as described earlier.

To purify the recombinant protein, Magne® Protein A Beads that bind the Fc-tag were used. In 5 ml PBS, 500 µl re-suspended protein beads were washed and centrifuged for 1 minute at 300 x g. Supernatant was discarded and the lysed protein suspension was added. The suspension was incubated at room temperature for 1.5 hours with 20 rpm agitation. The beads were collected at the wall of the tube using a universal magnet plate and protein suspension was discarded. The beads were washed with 5 ml of PBS and pelleted again with a universal magnet plate. The washing step was repeated once more, and afterwards the beads were incubated in protein elution buffer for 5 minutes with agitation. Meanwhile, 80 µl of neutralization buffer was added to a fresh 1.5 ml tube and cooled on ice. The beads were collected again at the wall of the tube using a universal magnet plate, and the protein elution buffer was transferred to the tube containing the neutralization buffer and mixed by pipetting several times. The elution was repeated once more. Protein concentrations were measured with a NanoDrop™ 2000 spectrophotometer. The purity and size of the TMEM158-hFc protein was determined by Western blot analysis as described above with 2.5 µg of recombinant protein.

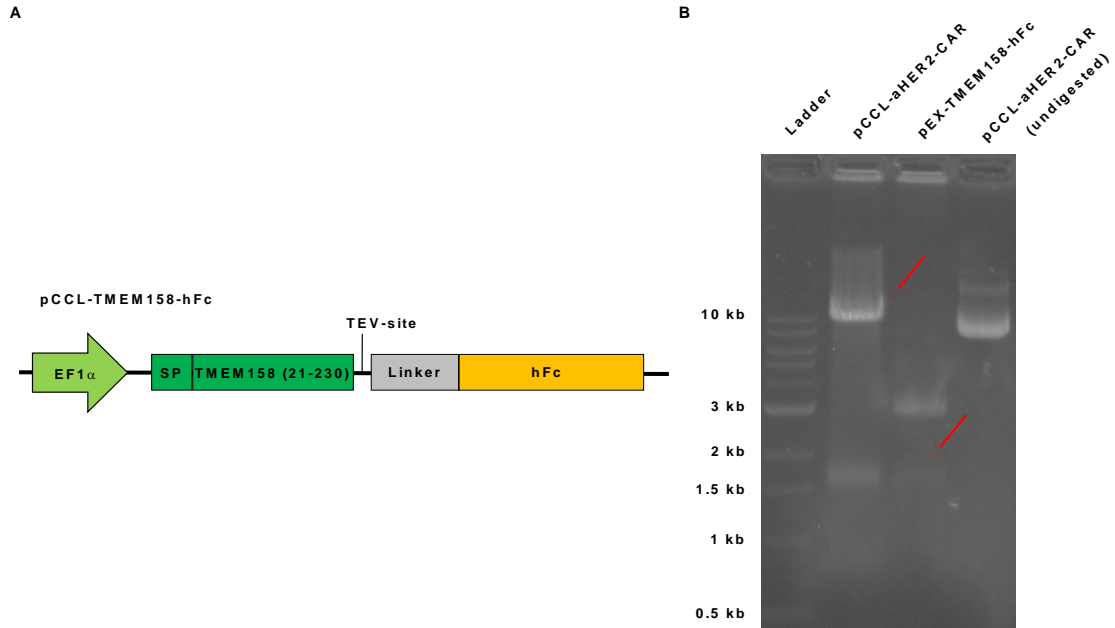


Figure 4: Scheme and cloning of recombinant TMEM158. **A)** Expression cassettes of recombinant TMEM158-hFc. Shown is a scheme of the expression cassette of the extracellular part of TMEM158, fused to a human Fc-Tag. **B)** Agarose gel loaded with restriction digested plasmids for cloning of TMEM158-hFc into pCCL backbone. Indicated plasmids were cut with *Ascl* and *NheI*. Bands indicated by the red arrow were cut out of the gel using a scalpel for purification of the digested plasmids and ligation. Undigested plasmids were also loaded on the gel to determine separation of the lower border of the bands from cut and uncut plasmids as orientation for cutting out the bands. Abbreviations: EF1 α , elongation factor-1 alpha (promoter); SP, signaling peptide (TMEM158); TEV, Tobacco etch virus (protease cleavage site); hFc, human fraction crystallizable (antibody fragment)

3.17 Peptide binding assay

To demonstrate binding of the peptide to the recombinant TMEM158-hFc protein, a plate-based binding assay was performed. Either 1.5 μ g TMEM158-hFc protein or pooled IgG from human serum was immobilized on a high-binding polystyrene 96-well flat bottom plate in 100 μ l (bicarbonate) coating buffer in triplicates overnight. Wells were washed once with 300 μ l PBS and blocked with 200 μ l of 1 % BSA in PBS per well for 1 hour at room temperature. Different concentrations of Rhodamine B-labeled BINP were added to the plate in 90 μ l blocking buffer per well and incubated for 1 hour at room temperature in the dark. The plate was washed 3 times with flow cytometry (FC) buffer, and 100 μ l of PBS was added to the plate before measuring fluorescence at 550/600 nm using an Infinite® 200 plate reader. Wells without immobilized protein were treated in the same way as described and measured as negative control.

To compare binding of BINP and scrambled BINP (scBINP), the signal of both peptide versions was normalized by subtracting the negative control. Therefore, scBINP signal of the lowest compared concentration was multiplied with a factor to equalize the signal to the corresponding BINP signal. The same factor was used to convert the signal of higher scBINP concentrations. A logarithmic function was calculated for each curve by fitting, and parameters of the negative control curve function were subtracted from the corresponding BINP or scBINP curve function. The data points of each normalized curve are shown.

3.18 Design and cloning of CAR

The sequence encoding a CAR containing BINP, fused to an Immunoglobulin G (IgG)4-linker, was cloned into a published second-generation CD28-CAR-sequence within a pCCL plasmid^{143,144} (provided by Dr. Jana Burkhardt). This CAR plasmid, designated as pCCL-BINP-WT-CAR in the following chapters, was used to generate mutated BINP-CAR versions by site directed mutagenesis as described in 3.14. In those CAR-variants either leucine on position 5 of the BINP (L5A), arginine on position 7 (R7A) or phenylalanine on position 11 (F11A) was exchanged with alanine. Those exchanges were performed to generate non- or less-functional CAR-variants. Those CAR-plasmids, exhibiting an amino acid exchange, are named pCCL-BINP-L5A-CAR, -R7A-CAR or -F11A-CAR, according to the positions of the exchange. In order to investigate, whether the generation of an RGD motif in BINP influences the function of the CAR, also a corresponding construct was produced, in which alanine on position 9 of BINP was exchanged with aspartic acid. This plasmid is designated as pCCL-BINP-RGD-CAR, since it contains an RGD-motif. A scheme of those plasmids described above is shown in Figure 5A (pCCL-BINP-CAR) and a scheme of a CAR-T cell binding a target cell that expresses TMEM158 via the BINP-CAR molecule is illustrated in Figure 5B.

The BINP-WT-CAR encoding genetic sequence was sub-cloned back to the plasmid backbone of the pCCL-BINP-F11A-CAR since a mutation in the pCCL-BINP-WT-CAR backbone occurred randomly during a re-transformation after introduction of the amino acid exchanges. Therefore, the sequence of the extracellular part of the BINP-WT-CAR was cut out of the plasmid by restriction digestion with *Ascl* and *Bam*HI (as described in Chapter 3.11 to 3.13), and bands matching the predicted band sizes of about 10 and 0.8 kb were observed in an agarose gel for both plasmids (Fig. 5C).

In addition to the BINP-CAR-plasmids, a pCCL-plasmid without CAR sequence (received from Prof. Bramson, McMaster University, Canada) was used to produce transduced T cells (Chapter 3.19 - 3.21) without expression of any CAR as negative control (Fig. 5A, pCCL-control). Also, a version of the pCCL-plasmid which contains all genetic elements including the CAR but without any binding domain was generated as an additional control (Fig. 5A pCCL-IgG-control-CAR). A pCCL-vector containing an anti-HER2-CAR¹⁴⁵, which was used to generate anti-HER2-CAR-T cells, was applied as a control showing high functionality against HER2⁺ GBM cells¹⁴³ (Figure 5A, pCCL-aHER2-CAR).

All pCCL-based plasmids contain a truncated p75 nerve growth factor receptor (Δ NGFR; missing large parts of the cytoplasmatic tail) sequence as detection marker, which can be visualized via flow cytometry as described in 3.10.

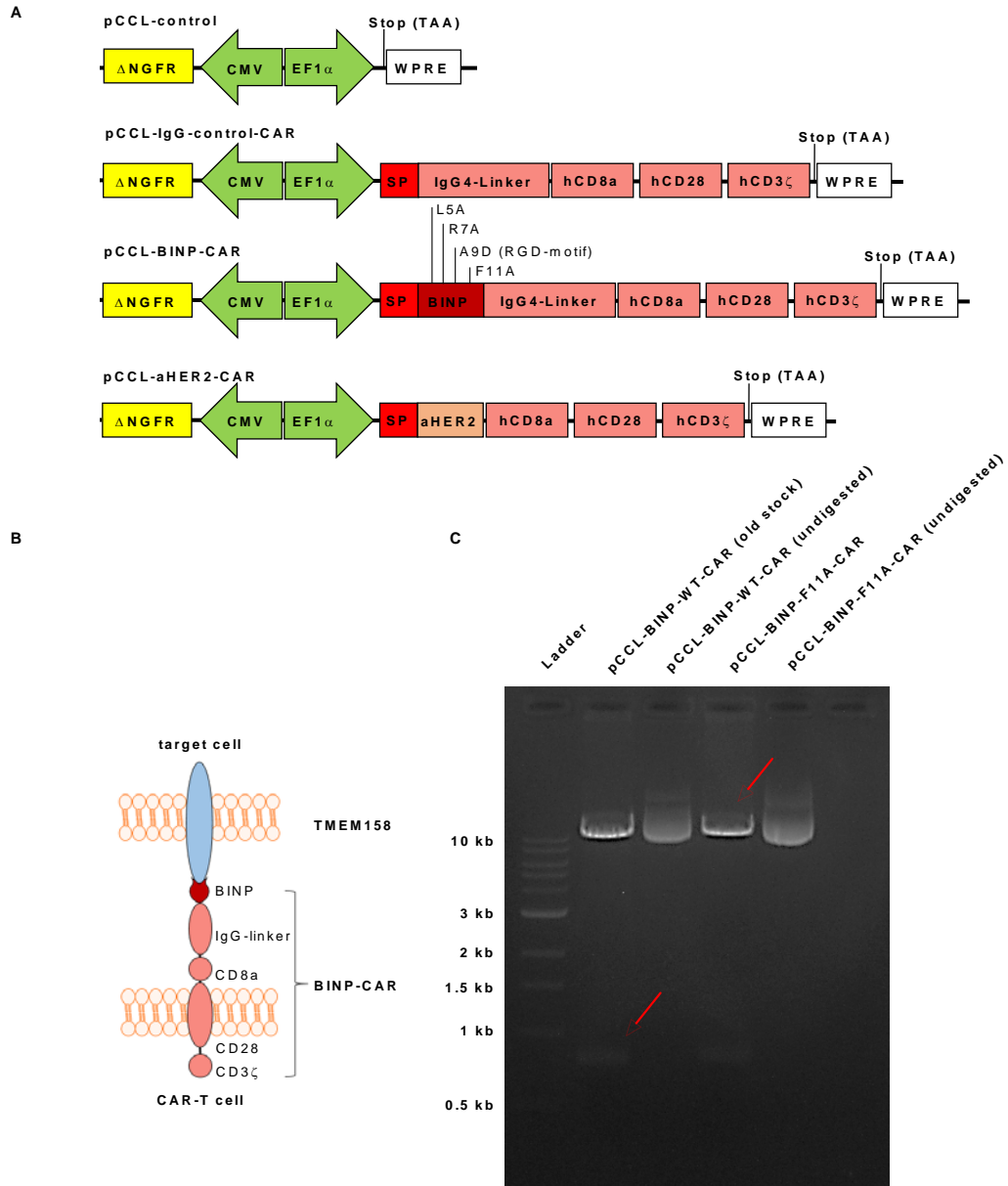


Figure 5: Cloning of BINP-CAR-T constructs **A)** Expression cassettes of BINP-CARs. Shown are the control vectors and the second-generation CAR constructs consisting of a CD8a transmembrane domain, intracellular signaling domains of CD28 and CD3 ζ (light red) as well as the BINP-IgG4 domain (dark red) for antigen binding. The CAR-cassette was cloned into a lentiviral pCCL vector. **B)** Scheme of the BINP-CAR protein on a T cell, binding to TMEM158 on the surface of a target cell. The BINP-CAR is illustrated in red and TMEM158 is shown in blue. **C)** Agarose gel loaded with restriction digested plasmids for re-cloning of BINP-WT-CAR. Both plasmids were cut with *Ascl* and *Bam*HI. Bands indicated by the red arrow were cut out of the gel using a scalpel for purification of the digested plasmids and ligation. Undigested plasmids were also loaded on the gel to determine separation of the lower border of the bands from cut and uncut plasmids as orientation for cutting out the bands.

Figure 5 (continued): Cloning of BINP-CAR-T constructs Abbreviations: aHER2, anti-human epidermal growth factor receptor 2; BINP, brain injury-derived neurotrophic peptide; CAR, chimeric antigen receptor; CMV, cytomegalo virus (promoter); EF1 α , elongation factor 1 α (promoter); hCD8a/28/3 ζ , human cluster of differentiation 8a/28/3 ζ ; IgG4, Immunoglobulin G4; Δ NGFR, truncated p75 nerve growth factor receptor (missing large parts of the cytoplasmic tail); SP, signal peptide (IgG heavy chain variable region); TMEM158, transmembrane protein 158; WPRE, woodchuck hepatitis virus (WHV) posttranscriptional response element.

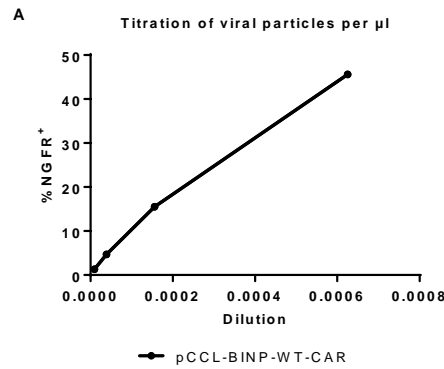
3.19 Production of viral particles

Helper plasmids of a third-generation lentiviral transduction system, pMDLg/pRRE, pRSV-Rev and pMD2.G (see Figure 17, 8.1 Appendix), were received from Prof. Jonathan Bramson (McMaster University, Hamilton, Canada). To produce lentiviral particles, helper plasmids and a pCCL-plasmid, originally generated by Dr. Megan Levings¹⁴⁴ (University of British Columbia, Vancouver, Canada), containing the sequence encoding one version of the BINP-CAR, were transfected into 293T cells by lipofection. 293T cells were thawed and expanded until three 15 cm² petri dishes per virus type were at about 80 % confluence. A transfection mix consisting of 120 μ l of EcoTransfect Transfection Reagent and 4 ml Opti-MEMTMI Reduced Serum Medium per virus type was produced, mixed by inverting the tube 5 times and incubated at room temperature for 5 minutes. Meanwhile, in a different tube per virus type, 4 ml of Opti-MEMTMI Reduced Serum Medium, 32 μ g of pCCL-BINP-CAR DNA, 12.5 μ g of pMDLg/RRE DNA, 6.25 μ g of pRSV-Rev DNA and 9 μ g of pMD2.G DNA, respectively, were combined and mixed by inverting the tube 5 times. The DNA and transfection reagent containing solutions were combined, mixed again by inverting the tube and incubated for 20 minutes at room temperature. During that time, medium of the 293T cells was replaced with 8 ml Opti-MEMTMI Reduced Serum Medium. The transfection mix was again mixed by inverting the tube multiple times after incubation, added to the cells drop wise in a concentric way and incubated overnight at 37 °C in a 5 % CO₂-humidified incubator. Medium was changed to 15 ml culture medium per dish containing 1 mM sodium butyrate and incubated for 2 days. To concentrate the viral particles by ultrafiltration, the supernatant was first transferred to a 50 ml tube and centrifuged at 2000 x g for 5 minutes at 4 °C to pellet cell debris. Afterwards, supernatant was filtrated through a 0.45 (polyethersulfone) PES bottle-filter. Amicon Ultra-15 100 kDa centrifugal filters were pre-wetted by adding 5 ml of DPBS and centrifugation at 2000 x g for 5 minutes at 4 °C.

DPBS was discarded, 15 ml of filtrated virus supernatant was added to the Amicon filter, and the tube was centrifuged for 30 minutes at 2000 x g at 4 °C. Flow-through was discarded and fresh 15 ml of viral supernatant were added and centrifuged. The procedure was repeated until all 45 ml of supernatant from 3 dishes was concentrated to about 300 μ l. Aliquots of 25 μ l and an aliquot of 5 μ l for the titration were generated using low-retention pipette tips and immediately frozen at -80 °C.

3.20 Virus titration

To determine viral titers, 30,000 293T cells were seeded in 500 μ l 293T-medium per well into 6 wells of a 24-well plate for each virus type. One additional well was seeded serving as untransduced control. Cells were transduced with viral particles 12 hours after seeding. On the day of infection, a serial dilution was generated on a separate 24-well plate. Therefore, 995 μ l were added to the first well of a row and 750 μ l were added to the other wells of the same row. Five μ l of concentrated virus was added to the first well (200-fold dilution), the medium was mixed by pipetting up and down 10-times and 250 μ l were transferred to the second well. The medium of the second well was mixed as before, and 250 μ l were transferred to the next well. The procedure was repeated for each well of the row (4-fold serial dilution). From each well, 500 μ l were transferred to the matching well containing 293T cells. The cells were cultivated for 2 days, stained for Δ NGFR-expression as described in 3.10 and the percentage of Δ NGFR⁺ cells was determined for each dilution using flow cytometry. A titration curve was generated by plotting the percentage of Δ NGFR⁺ cells against the dilution (μ l virus / μ l total volume) (Fig. 6A). Slope and intercept of the linear part of the curve as well as mean percentage of Δ NGFR⁺ cells of the samples were calculated. The number of viral particles per ml, referred to as titer, was calculated using the following formula shown in figure 6B.



B

$$Titer = \text{Number of cells} \times \left(\frac{\% \text{positive cells}}{100} \right) \times \text{dilution factor}$$

Figure 6: Titration of the viral particles per μ l of concentrated supernatant on 293T cells. A log₄ dilution series of the concentrated supernatant from virus production was generated and added to individual wells of a 24-well plate, each containing 30,000 293T cells. Cells were harvested and stained using an antibody (CD271 (LNGFR) -Viobright FITC antibody) against the Δ NGFR marker protein 48 hours after infection. **A)** Flow cytometric quantification of transduced 293T cells. Percentage of Δ NGFR⁺ cells was determined using flow cytometry. Slope and intercept of the linear part of the curve (lowest three data points in this example) were calculated by linear regression and used for calculating the number of viral particles per μ l and per ml. **B)** Formula for calculation of the number of viral particles per ml. Abbreviations: BINP, brain injury-derived neurotrophic peptide; CAR, chimeric antigen receptor; Δ NGFR, truncated p75 nerve growth factor receptor (missing large parts of the cytoplasmic tail).

3.21 Stimulation, transduction and cultivation of PBMC and primary T cells

Frozen peripheral blood mononuclear cells (PBMCs), isolated from buffy coat by Ficoll density gradient centrifugation as published¹⁴⁶, were received from Daniela Rudolf or Jasmin Adam (both were working at Fraunhofer IZI, Leipzig, Germany, at the time). Buffy coats were obtained from anonymous HIV⁻ donors that gave written consent via the Institute of Transfusion Medicine, University Leipzig. Purchase and handling were approved by the local ethics committee (272-12-13082012). PBMCs were thawed, counted, and re-suspended at a density of 1×10^6 cells per ml in T cell complete medium containing 100 U/ml IL-2 and 10 ng/ml IL-7. For stimulation, PBMCs were co-cultivated for four days with Dynabeads™ Human T-Activator CD3/CD28 at a bead-to-cell ratio of 0.8:1. The corresponding volume of Dynabeads™ was added to 1 ml DPBS, containing 0.1 % BSA and 2 mM EDTA and vortexed for 5 seconds.

Dynabeads™ were pelleted using a universal magnet plate for about 1 minute, supernatant was discarded and the Dynabead™-pellet was re-suspended in the same tube by adding the corresponding volume of PBMC cell suspension from before and mixing by pipetting. One hundred µl of the cell-Dynabead™ suspension was seeded per well of a 96-well round bottom plate. On the next day, cells were transduced at a multiplicity of infection (MOI) of 4 by adding the appropriate amount of thawed, concentrated viral supernatant to a well and slow resuspension by pipetting. One day after transduction, 100 µl of T cell complete medium with cytokines was added without resuspension. On day 4 after seeding, all wells transduced by the same viral supernatant were pooled in a 1.5-ml-tube and Dynabeads™ were pelleted using a universal magnet plate. Cell suspension without Dynabeads™ (200 µl per well) was seeded again in a 96-well round bottom plate. Afterwards PBMCs were cultivated for 2 to 3 weeks, split every 2 or 3 days and adjusted to 1×10^6 cells per ml each time. During stimulation and cultivation, cells were kept in T cell complete medium containing IL-2 and IL-15 and incubated at 37 °C in a 5 % CO₂-humidified incubator. Because of the T cell specific stimulation and cultivation, nearly all other cells besides T cells die during the cultivation or are drastically overgrown by T cells. Therefore, the cells are referred to as T cells, even though no cell purification was performed.

3.22 Luciferase-based cytotoxicity assay

Luciferase-transgenic cell lines were generated by our group previous to this work by lentiviral transduction of a firefly-luciferase transgene and puromycin based selection (2 µg/mL) for at least 7 days. Per well, 12,500 luciferase-expressing target cells were seeded onto white, flat-bottom 96-well plates and cultured for at least 5 to 16 hours. CAR-T cells were added at defined effector-to-target (E:T) ratios in T cell complete medium without IL-2 and IL-7. After 24, 28, and 44 hours of co-culture, 1 µg/well XenoLight D-luciferin (Perkin Elmer) in water was added and bioluminescence was measured using a Centro XS3 LB 960 plate-reading luminometer (Berthold Technologies). To calculate cytotoxicity, luminescence (relative light units) of wells containing only medium were averaged, subtracted from values of all other wells and the difference between the mean of each group and the mean of wells containing only tumor cells were calculated. T cells were used for functional assays after 14 to 21 days of cultivation if not stated otherwise.

Luminescence values of edge wells were excluded from the calculation when they were different from the other two replicates by a multiple on all plates of all cell lines (pCCL-control-T cells, Donor 1, Figure 16B).

3.23 Statistics and software

Data was analyzed and visualized using Excel Professional Plus 16 (version 16.0.5083.1000, Microsoft, Redmond, USA) or GraphPad Prism software 6 (version 6.07, June 12, 2015; GraphPad Software, San Diego, USA) and is depicted as mean \pm SD unless stated otherwise. For measurement and analysis of flow cytometry data, DIVA 8 (version 8.0.1; Becton Dickinson, Franklin Lakes, USA) and FlowJo™ v10 (version 10.8.1; Becton Dickinson, Franklin Lakes, USA) were used. For visualization of plasmids and primer design SnapGene v4 (version 5.2.4; Dotmatics, Bishop's Stortford, UK) was used. For visualization of Western blots and densitometrical quantification of band intensity, Image Studio™ Lite (version 5.2.5, LICOR Bioscience, Bad Homburg vor der Höhe, Germany) was used. The thesis was written using Word Professional Plus 16 (version 16.0.5083.1000, Microsoft, Redmond, USA) and Citavi 5 (version 5.2.0.8, Free, Swiss Academic Software, Waedenswil, Switzerland).

4 Results

4.1 Gene-expression, patient survival and stem cell marker correlation in public expression datasets of *TMEM158*

Previous to this work, potential targets of GBM were identified by datamining of public datasets by Dr. Jana Burkhardt. Selection criteria included high gene expression in GBM but low or no expression in normal (brain) tissue. One of thus identified candidate genes was *TMEM158*. A literature analysis was performed in 2017 to determine what was known about this potential target. At the time, as described in greater detail in chapter 1.4, publications showed experimental data that associated overexpression of *TMEM158* with colorectal cancer, thyroid carcinoma, lung cancer, ovarian carcinoma and triple-negative breast cancer^{127,130–132,134,147}. In most of those studies, gene expression of *TMEM158* was analyzed by PCR based methods, microarrays or epigenetic profiling. Only in a few studies, knockdown of *TMEM158*^{127,131} and analysis of its protein expression by Western Blot¹²⁷ was performed. One publication described the cloning and recombinant production of *TMEM158*, the development of an antibody against it, blocking of one physiological function by the antibody and binding to a peptide ligand identified as BINP^{121,122}.

Overexpression of *TMEM158* in GBM and its influence on patient survival was not described at the beginning of our investigations. Therefore, RNA datasets from the TCGA database (accessed on 12/04/2018), the GTEx (accessed on 09/09/2019) and the GEPIA tool (accessed on 09/29/2022) were analyzed to compare expression between tumor and normal tissue. First, mRNA expression between normal brain tissue, low-grade glioma and GBM (possibly containing low numbers of grade IV astrocytomas¹³⁸) was compared and a significantly higher expression in GBM in comparison to normal brain tissue ($p < 0.01$) was found. No significant difference was found between low-grade glioma and normal brain tissue (Fig.7A). To identify a possible prognostic value of *TMEM158*, also overall (Fig. 7B) and disease-free survival (DFS) (Fig. 7C) of glioma patients (GBM and LGG) with low and high gene expression was analyzed. Patients with low expression of *TMEM158* survived significantly longer than patients with high expression (overall survival: $p = 0$, HR (high)=3.8, disease-free survival: $p = 1.5 \times 10^{-8}$; HR (high)=2). Furthermore, correlation between expression of *TMEM158* and cancer stem cell markers *CD44* and *PROM1* (CD133) was analyzed in the GBM dataset, since these two markers are closely associated with the mesenchymal- or proneural GBM subtype.

Thereby, correlation of *TMEM158* and one of these markers might indicate association of *TMEM158* with one of the GBM subtypes. A moderate correlation between *TMEM158* and *CD44* ($R=0.44$, $p=5.1 \times 10^{-9}$), but none between *TMEM158* and *PROM1* ($R=0.11$, $p=0.15$) was observed (Fig. 7D).

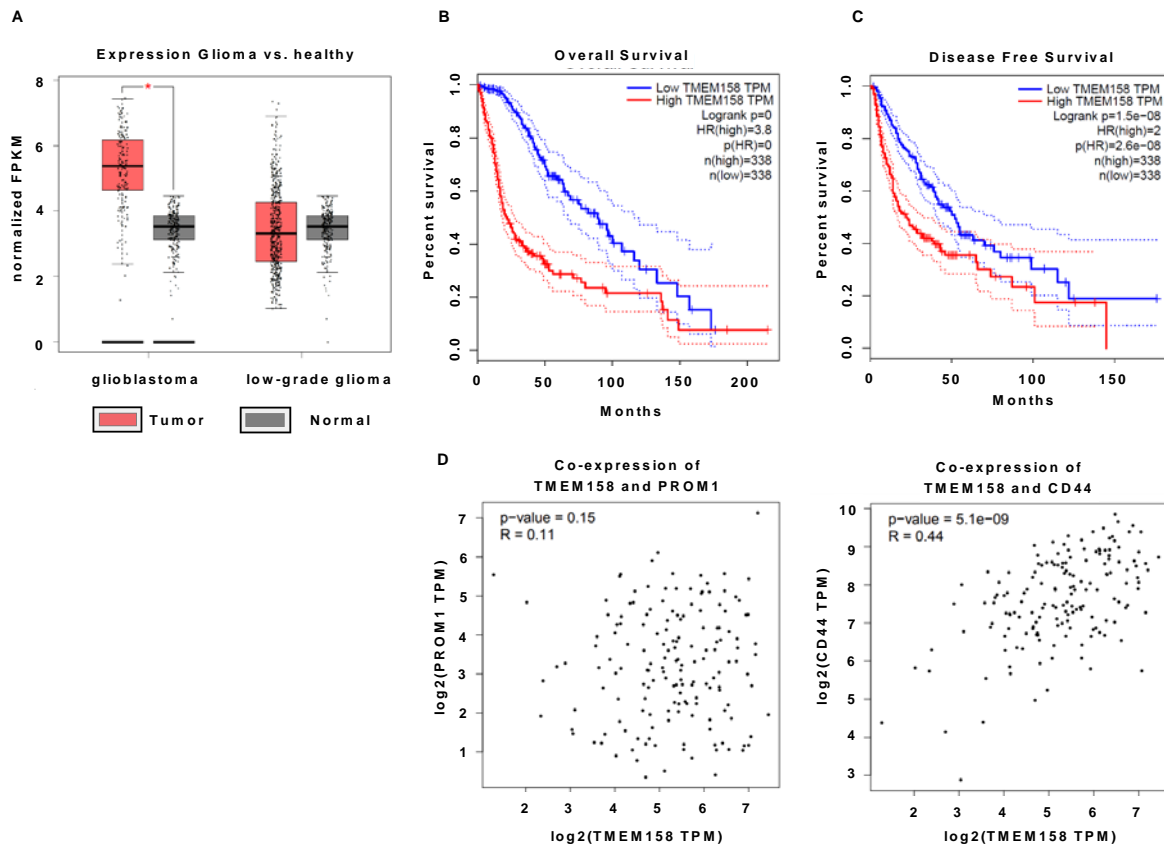
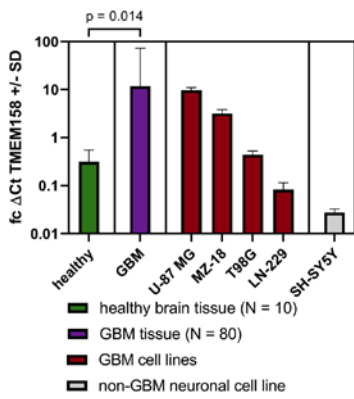


Figure 7: Gene-expression of *TMEM158*, influence on survival and correlation with cancer stem cell marker. **A)** Comparison of *TMEM158* gene-expression between low-grade glioma (LGG) ($n=518$), GBM ($n=163$) and normal brain tissue ($n=207$). Significance was determined by analysis of variance (ANOVA) with a p -value cut-off of 0.01 and a fold-change threshold of 2. **B)** Overall survival and **C)** Disease-free survival of GBM- and low-grade glioma patients, expressing low ($<$ median) or high ($>$ median) *TMEM158*. Hazard ratio and corresponding p -values are indicated as well. **D)** Co-expression of *TMEM158* and two cancer stem cell markers. Pearson correlation between *TMEM158* gene expression and either PROM1 (left) or CD44 (right) expression was calculated using data from the TCGA GBM dataset. Abbreviations: FPKM, Fragments per kilo base of transcript per million mapped fragments; HR, Hazard ratio; TPM, transcripts per million.

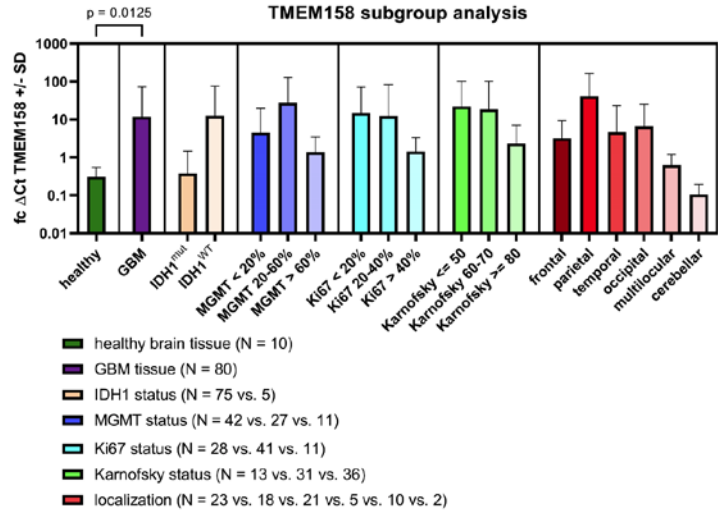
4.2 Gene-expression analysis of *TMEM158* in a clinically relevant patient subgroup

To validate the significance of *TMEM158* expression patterns in GBM, as observed in data from public data bases, also gene expression of *TMEM158* was analyzed in tissue obtained by surgery of a local cohort of patients for which clinical and molecular data was available. Also, expression was compared regarding IDH- and MGMT-status, Ki67 index and Karnofsky score, and with regard to tumor location. Characteristics of the cohort are shown in Figure 8D. In this analysis, also RNA from tumor surrounding tissue (peritumoral tissue, zone III; designated healthy brain tissue) that had to be surgically removed to obtain access to the tumor was included. In this analysis also significantly higher *TMEM158* gene-expression in GBM samples in comparison to normal brain tissue ($p=0.004$) was found (Fig. 8A). Additionally, significantly higher *TMEM158* gene-expression in IDH1^{WT} tumors in comparison to tumors with IDH1^{mut} ($p=0.125$) was observed. Other than that, no significant correlation with MGMT-, Ki67-, Karnofsky-status or tumor location was seen (Fig. 8B). Also, overall survival of *TMEM158* low (< median expression) and high (> median expression) was analyzed in the local cohort of GBM patients. No significant difference in survival was found between both patient groups (Figure 8C).

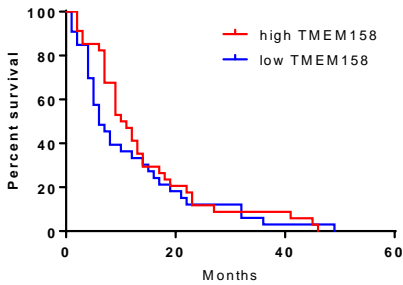
A **TMEM158 expression cell lines**



B **TMEM158 subgroup analysis**



C **Overall survival (Leipzig cohort)**



D

Sample type	Gender		Location of Tumor	Age		Karnofsky	Ki-67 [%]	IDH		MGMT [%]	OS [mths.]	PFS [mths.]	
	M	F		≥ 60	<60			WT	mut.				
Glioblastoma	46	34	Frontal	23	59	21	72.0 \pm 17.5	22.8 \pm 12.5	75	5	26.5 \pm 23.1	11.3 \pm 9.6	11.2 \pm 9.8
			Parietal	18									
			Occipital	5									
			Temporal	21									
			Cerebellar	2									
			Multilocular	10									
Healthy Brain Tissue	5	3	-		6	2	-	-	-	-	-	-	-

Figure 8: Gene-expression of *TMEM158* in a local cohort and differences between subgroups.

TMEM158 gene-expression, measured by RT-qPCR. **A)** Comparison between GBM and normal brain tissue as well as GBM cell lines. GBM samples (n=80, including 5 grade 4 astrocytomas, formerly designated as secondary GBM) and normal brain tissue (n=10) from local patients are compared with different GBM and a neuroblastoma cell line. **B)** Comparison between indicated subgroups of the same dataset. All samples were measured in technical quadruplicates and their mean expression levels were normalized to *RPL32* expression. Fold change was calculated for all ΔCt values and are depicted as $\log_{10}(2^{\Delta\text{Ct}}) \pm \text{SD}$. **C)** Overall survival of GBM patients from the University Hospital Leipzig with high (> median expression) or low (< median expression) *TMEM158* expression is illustrated as Kaplan-Maier plot. Statistical significance was calculated by log-rank test. **D)** Clinical characteristics of the patient cohort analyzed by RT-qPCR. Samples were obtained from patients during surgery and expression of Ki-67, IDH mutation- and MGMT methylation status were measured by RT-qPCR. Clinical metadata is shown as total number (Gender, Age, Location and IDH status) or as mean \pm SD (Karnofsky index, Ki-67, MGMT, OS and PFS). Gender and age of two donors of normal tissue is not included, since data was not accessible. Abbreviations: M, male; F, female; IDH, isocitrate dehydrogenase; WT, wild type; OS, overall survival; PFS, progression-free survival.

4.3 Gene-expression, patient survival and stem cell marker correlation in public expression datasets of *PTPRZ1*

Analogous to *TMEM158*, expression of *PTPRZ1* was analyzed in RNA datasets from the TCGA database (accessed on 12/04/2018), GTEx (accessed on 09/09/2019) and the GEPIA tool (accessed on 09/29/2022) regarding expression in different tissue groups. First, expression between low-grade gliomas or GBM (might contain low numbers of grade IV astrocytomas) and normal brain tissue was compared. A significantly higher expression in both types of cancer in comparison to normal brain tissue ($p < 0.01$) was observed (Fig. 9A). To analyze the influence of *PTPRZ1* expression on the survival of patients, overall- (Fig. 9B) and disease-free survival (Fig. 9C) of glioma patients (GBM and LGG) with low and high gene-expression was analyzed. Patients with low expression of *PTPRZ1* survived significantly longer than patients with high expression (Overall survival: $p = 0.0072$; HR (high)=1.4, Disease-free survival: $p = 0.00046$; HR (high)=1.6). Also, correlation between gene-expression of *PTPRZ1* and *CD44* and *PROM1* (CD133) in the GBM dataset was calculated. No correlation between *PTPRZ1* and *PROM1* or *CD44* was observed (Fig. 9D).

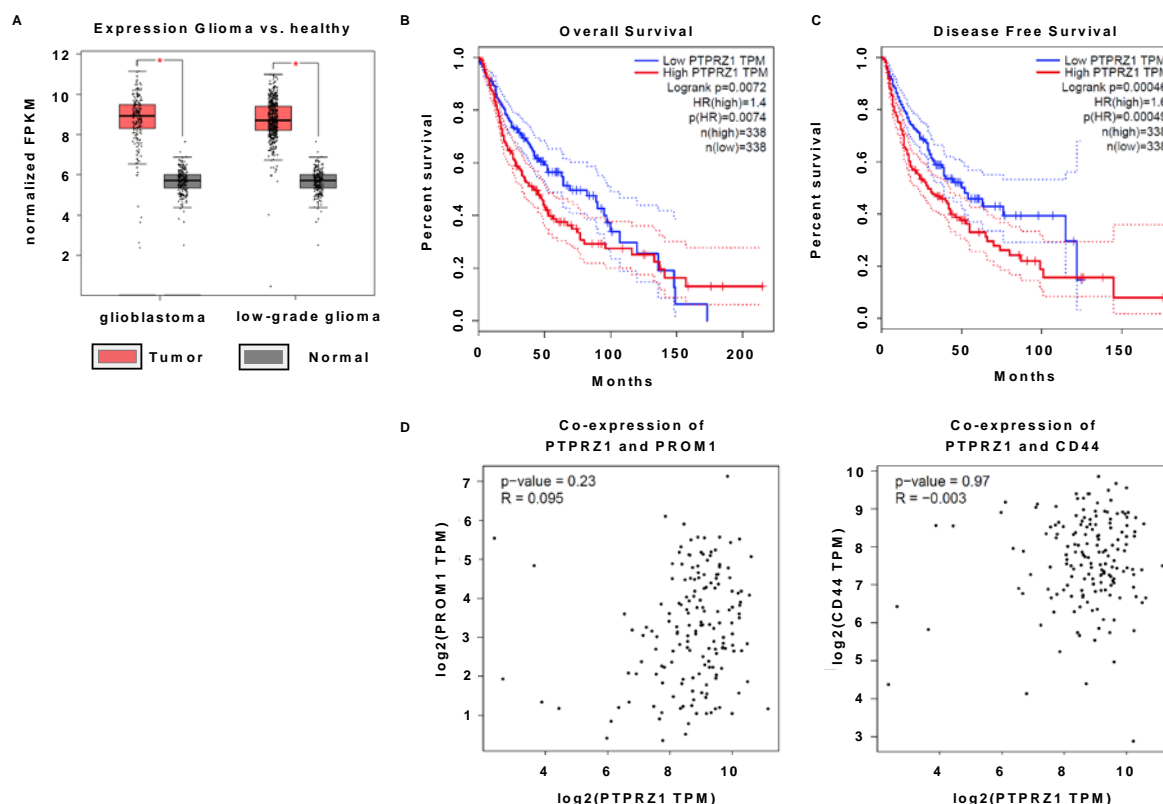


Figure 9: Gene-expression of *PTPRZ1*, influence on survival and correlation with cancer stem cell marker. **A)** Comparison of *PTPRZ1* gene-expression between low-grade gliomas (LGG) (n=518), GBM (n=163) and normal brain tissue (n=207). Significance was determined by analysis of variance (ANOVA) with a p-value cut-off of 0.01 and a fold-change threshold of 2. **B)** Overall survival and **C)** Disease-free survival of GBM- and low-grade glioma patients, expressing low (< median) or high (> median) *PTPRZ1*. Hazard ratio (HR) and corresponding p-values are indicated as well. **D)** Co-expression of *PTPRZ1* and two cancer stem cell markers. Pearson correlation between *PTPRZ1* gene-expression and either *PROM1* (left) or *CD44* (right) expression was calculated using data from the TCGA GBM dataset. Abbreviations: *FPKM*, Fragments per kilo base of transcript per million mapped fragments; *HR*, Hazard ratio; *TPM*, transcripts per million.

4.4 Gene-expression analysis of *PTPRZ1* in a clinically relevant patient subgroup

To confirm the overexpression of *PTPRZ1* in GBM, as observed in data from previous publications and public data bases, gene-expression in a local cohort of patients was analyzed by RT-qPCR.

Also, differences in expression between patients regarding IDH- and MGMT-status, Ki67 index and Karnofsky score, and tumor location were analyzed. Characteristics of the cohort are shown in Figure 8D. RNA from tumor surrounding tissue (peritumoral tissue, zone III; designated healthy brain tissue) was also isolated and measured for comparison. In this analysis also significantly higher *PTPRZ1* gene-expression was found in GBM samples in comparison to normal brain tissue ($p=0.0001$) (Fig. 10A/B). Other than that, no correlation with MGMT-, Ki67-, Karnofsky-status or tumor location was seen. Furthermore, overall survival of *PTPRZ1* low (< median expression) and high (> median expression) was analyzed in the local cohort of GBM patients. No significant difference in survival was found between both patient groups (Figure 10C).

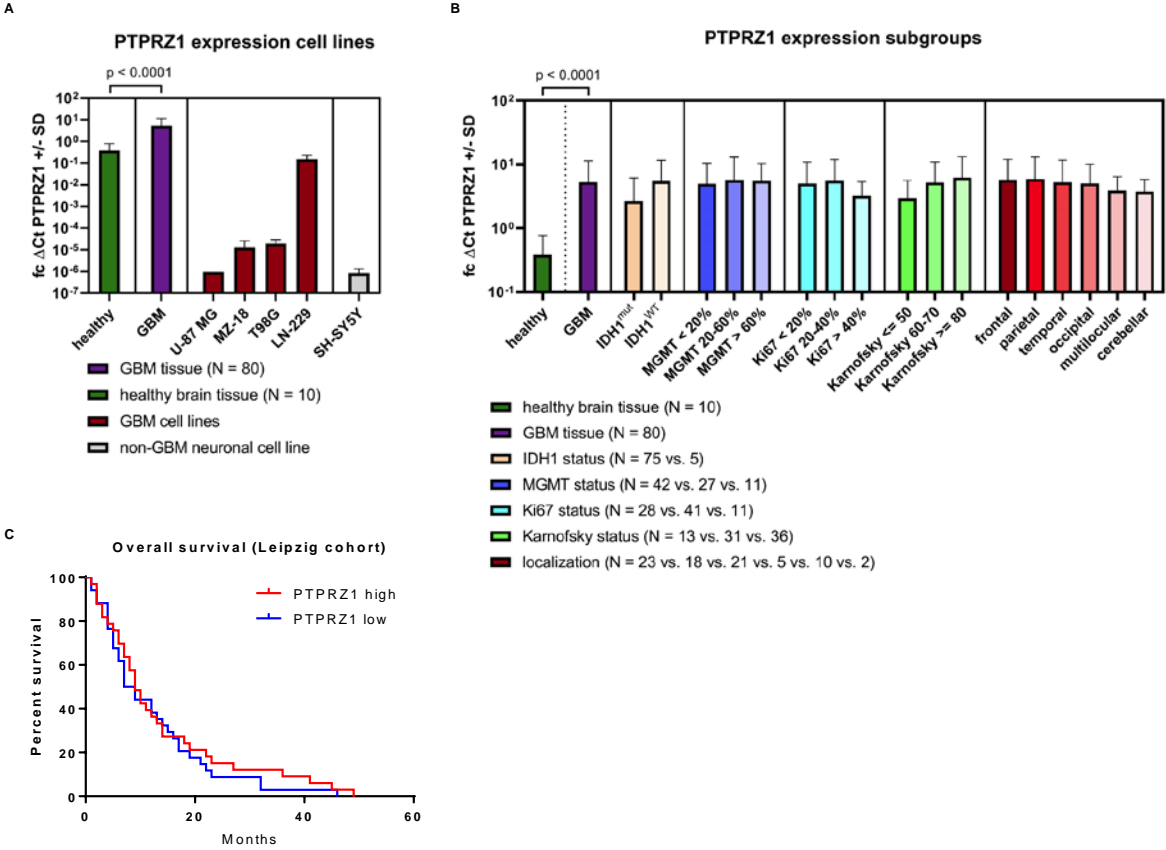


Figure 10: Gene-expression of *PTPRZ1* in a local cohort and differences between subgroups. *PTPRZ1* gene-expression was measured by RT-qPCR. **A)** mRNA expression in GBM samples (n=80, including 5 grade 4 astrocytomas, formerly designated as secondary GBM) and normal brain tissue (n=10) from local patients are compared with different GBM and a neuroblastoma cell line. **B)** Comparison between indicated subgroups of the same dataset. All samples were measured in technical quadruplicates and their mean expression levels were normalized to *RPL32* expression. Fold change was calculated for all ΔCt values and are depicted as $\log_{10}(2^{\Delta\text{Ct}}) \pm \text{SD}$. **C)** Overall survival of local GBM patients from the University Hospital Leipzig with high (> median expression) or low (< median expression) *TMEM158* expression is illustrated as Kaplan-Maier plot. Statistical significance was calculated by log-rank test.

4.5 Protein expression and knockdown of *TMEM158* expression in GBM cell lines

Since mRNA- and protein expression of molecular markers can differ extensively, next expression of *TMEM158* protein was analyzed in different GBM and non-GBM cell lines. First, two different antibody dilutions within the range recommended by the antibody manufacturer were compared, since no data was published at the time. Signals of 5 and 10 μg of total protein from T98G, MZ-18, 293T and SH-SY5Y cells at 1:1500 or 1:3000 anti-*TMEM158* antibody dilution were compared. The 1:1500 dilution was chosen for the following experiments because of better signal to background ratio, as observed by eye (Figure 19, 8.3 Appendix). Next, protein expression in 4 human (T98G, U-87 MG, MZ-18, LN-229) and one mouse (GL-261) GBM cell line as well as in one human neuroblastoma cell line (SH-SY5Y) was analyzed by Western blot. The murine GL-261 cell line was included in this analysis because it was used for murine, syngeneic GBM models before^{148,149}, which might be an option for investigating cross-reactive treatments against *TMEM158*. A protein band was observed at about 50 kDa in all cell lines with differing intensity (Fig. 11A). To verify that this band is *TMEM158*, a knockdown in T98G cells was performed with DsiRNA, and the protein amount was quantified densitometrically. After this treatment, the relative signal intensity of the band was reduced by about 30 %, suggesting that the staining for *TMEM158* is specific (Fig. 11B).

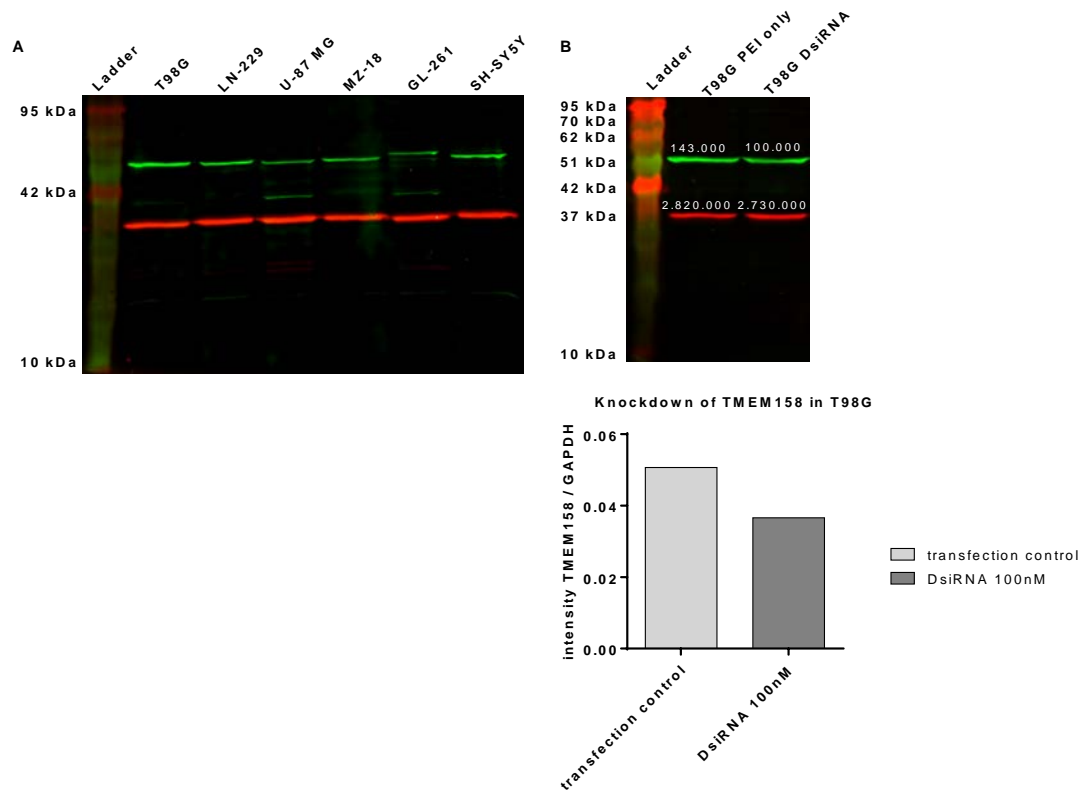


Figure 11: Protein expression and knockdown of TMEM158 in different cell lines. A) Western blot analysis of TMEM158 in GBM cell lines and the neuroblastoma cell line SH-SY5Y. Blots were stained at a 1:1500 antibody dilution against TMEM158 (ab98335) and 1:3000 against GAPDH (GA1R). Bands shown in green represent TMEM158, while red bands indicate GAPDH, which was used as loading control. **B)** DsiRNA knockdown of TMEM158. T98G cells were either transfected with only PEI as control or PEI and 100 nM of DsiRNA directed against TMEM158. Signal intensities were determined densitometrically and are written above the corresponding band in relative intensities (top). The ratio of both fluorescence intensities was calculated and is shown in the lower graph (N=1). Abbreviations: DsiRNA, double stranded small interfering RNA; GAPDH, Glyceraldehyde 3-phosphate dehydrogenase; GBM, glioblastoma; PEI, polyethylenimine; TMEM158, transmembrane protein 158.

4.6 Binding of BINP to GBM cell lines

For therapeutic targeting of TMEM158 on GBM cells, it is important to show that the protein is also present on the cell surface of target cells in adequate amounts. A suitable antibody, which recognizes an epitope of TMEM158 with intact folding, as required for flow cytometry, was not commercially available at the time. But it was previously found that brain injury-derived neurotrophic peptide (BINP) binds to TMEM158^{118,121,122}.

To analyze binding of BINP to GBM cells, they were incubated with fluorescence-labeled synthetic BINP or a scrambled version for staining, followed by measuring fluorescence by flow cytometry. First, fluorescence signals in T98G cells were quantified after incubation with different peptide concentrations, ranging from 28.8 to 115.2 μ M. As shown in Figure 21A/B (8.5 Appendix), lower signals with lower concentrations of BINP were observed, while only about one third to one half of cells showed binding of the scrambled peptide at a corresponding peptide concentration. Since peptides might detach from target cells over time, it was of interest to find out, how stable the BINP staining is. Interestingly, it was observable that the BINP signal didn't change over time within 1 hour but the signal of the scrambled BINP, which was at a comparable level as the BINP signal when measured within minutes after staining, decreased fast within one hour (Figure 21C, 8.5 Appendix). Since only the signal measured after 1 hour seems to be a specific signal, for the following experiments a time point of 1 hour was used for measuring.

Next, binding of labeled BINP to cells from a neuroblastoma cell line (SH-SY5Y), which exhibited only low expression of *TMEM158* (Fig. 8A), and to cells from two GBM cell lines was analyzed. T98G showed a signal with 40.1 ± 23 % positive cells, while 37.2 ± 11.5 % of U-87 MG and 7.0 ± 1.4 % of SH-SY5Y cells were positive. After staining with the scrambled BINP, only 22.7 ± 8.8 % of T98G and 3.4 ± 3.5 % of SH-SY5Y cells were positive, but surprisingly 81.4 ± 5.1 % of U-87 MG cells. MFI mostly resembled these proportions, although the MFI of U-87 MG was much higher for both peptide versions in comparison to both other cell lines, possibly indicating unspecific staining against this cell line (Fig. 12A/B). Also, for T98G and SH-SY5Y two distinct cell populations were recognizable, but a gradient like distribution of positive cells, peaking at a very high fluorescence intensity was observed for U-87 MG, which might confirm unspecific staining in this cell line (Figure 12C). A representative example of the gating used to measure samples of the flow cytometry experiments is shown in Figure 12D.

Furthermore, staining of T98G cells with and without knockdown was analyzed to validate specificity of BINP binding to TMEM158. About 95 % of T98G cells showed a positive signal after staining with BINP without knockdown, while only 55 % of cells were positive after knockdown, resulting in a difference of 40 %, between these groups (Fig. 22A/B, 8.6 Appendix). This percentage is comparable to the difference in signal intensity of about 30% observed in Western blot analysis (Fig. 11B), when protein of T98G cells with and without DsiRNA treatment were stained by antibody. It has to be taken into account, though that in this flow cytometry experiment no live/dead discrimination was performed and that this analysis was only done once.

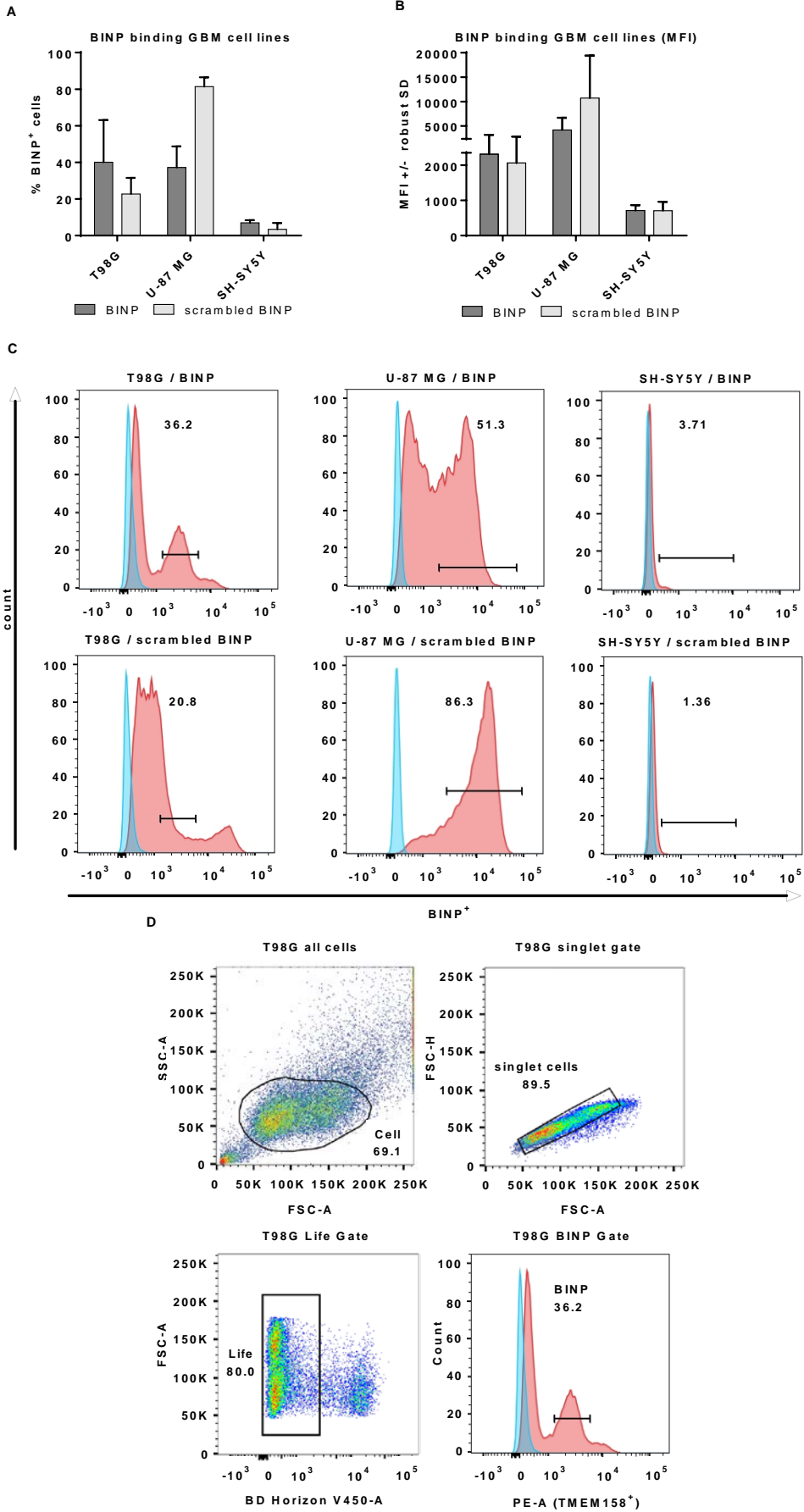


Figure 12: Flow cytometry analysis of BINP binding to TMEM158. A) - C) BINP binding to different GBM and non-GBM cell lines. Cells were stained with BINP at a concentration of 57.6 μ M. Cells stained with a scrambled version of BINP served as control. Shown is the percentage of positive stained T98G cells (A), MFI (B) of Rhodamine B-positive cells (PE channel) or histograms (C) of live singlet cells. Data is illustrated as mean \pm SD and was measured in biological triplicates, except for the staining of U-87 MG and SH-SY5Y with scrambled BINP, which was measured in biological duplicates (A/B). Histograms show one representative example of the performed experiments (C). **D)** Gating of T98G cells stained with BINP. Cells were stained with BD Horizon™ Fixable Viability Stain 450 for exclusion of dead cells and Rhodamine-B labeled BINP at a concentration of 115.2 μ M. Cell debris and larger cell conglomerates were excluded by the gate shown in the upper left picture. Doublet cells (upper right) and dead cells (lower left) were excluded as well. Living singlet cells were analyzed as shown in the histogram (lower right). Shown is one representative example of samples analyzed in A) – C). Abbreviations: FSC, forward scatter; MFI, median fluorescence intensity; PE, Phycoerythrin; SSC, side scatter.

4.7 Protein expression of integrin α V β 3 on GBM cell lines

It is known that integrin α V β 3 is a promising GBM target and can bind to the RGD motif found in several proteins. Within the BINP sequence the first two amino acids of this motif, arginine, and glycine, are present. As it was tempting to speculate that the introduction of an RGD motif at this site may increase binding to GBM cells, protein expression of integrin α V β 3 was quantified in several cell lines using flow cytometry (Fig. 13). Here, it was detectable that over 95 % of LN-229, U-87 MG and T98G cells were positive for integrin α V β 3, while only 59.6 \pm 1.6 % and 0.2 \pm 0.1 % of MZ-18 and SH-SY5Y cells were positive, respectively (Fig. 13, left). The MFI of the stained cell lines is shown in Figure 13 (right graph). Based on the different expression levels, U-87 MG, T98G and SH-SY5Y were chosen to test the influence of an RGD motif within BINP in CAR-based experiments, presented later on in Chapter 4.10B/C.

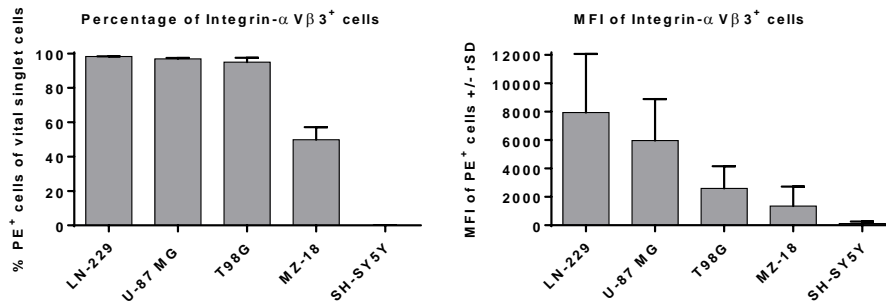
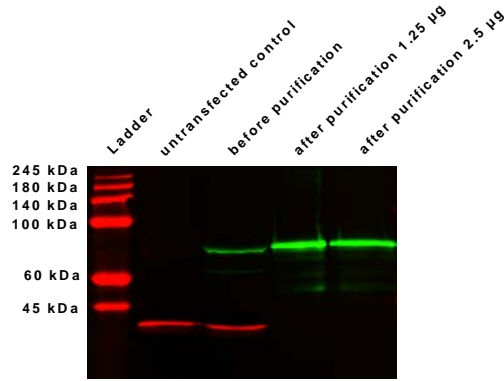


Figure 13: Flow cytometry analysis of integrin $\alpha V\beta 3$ in GBM cells and in cells from a neuroblastoma cell line. Shown is the percentage of positive stained cells (left) and the median fluorescence intensity (MFI, right) of singlet cells. Data was measured two times with technical duplicates each and is illustrated as mean \pm SD.

4.8 Production of recombinant TMEM158-hFc protein and binding by BINP

To enable precise determination of binding between BINP, modified versions and other potential ligands, a fusion protein was produced, consisting of the extracellular part of TMEM158 and a human Fc-tag. A scheme of the expression cassette is shown in Figure 4A. The genetic sequence encoding the fusion protein was cut out of the pEX-plasmid using *Ascl* and *NheI* (Fig. 4B) and cloned into the pCCL plasmid. To preserve human post-translational modifications, 293T cells were used as expression system. The size of the protein, purified using magnetic protein A beads that bind the Fc-part of the recombinant TMEM158, was analyzed by Western blot, and a protein band was found at about 75 kDa (Fig. 14A). According to calculations¹⁵⁰, the size of the recombinant protein should be 55.75 kDa without glycosylation. Next, a plate-based binding-assay was performed to show binding and thereby indirectly correct folding of the produced protein. It was observable that Rhodamine B-labeled BINP was binding to wells with recombinant protein stronger than to wells without protein, visible by the upward slope of the normalized curve. In addition, binding of the Rhodamine B-labeled BINP was stronger than that of a scrambled version, recognizable by the difference in steepness of the compared curves. (Fig. 14B). Since higher binding of the scBINP peptide in wells without immobilized TMEM158-hFc protein was observed in comparison to BINP, signal of both peptides was normalized with the signal of wells containing no immobilized protein for better comparison.

A



B

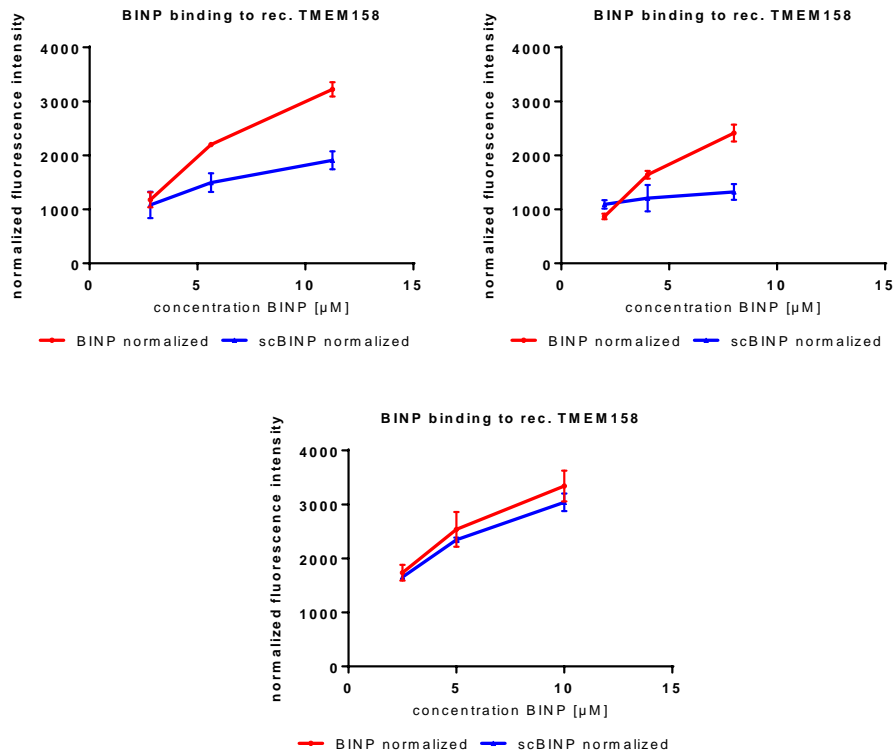


Figure 14: Size and binding of recombinant TMEM158. **A)** Western Blot of recombinant TMEM158 protein. The protein was produced in HEK293T cells and purified using magnetic protein A beads, which bind the hFc part. Bands shown in green represent recombinant TMEM158, while red bands indicate GAPDH, which was used as loading control. **B)** Binding of BINP to recombinant TMEM158-hFc. Proteins were immobilized on high-binding polystyrene plates overnight and stained with Rhodamine B-labeled BINP or -scrambled (sc) BINP on the following day. Fluorescence intensity was measured in technical triplicates and is shown as mean \pm SD at indicated (sc)BINP concentrations. The BINP and scBINP curves were normalized by subtracting the negative control curve (no immobilized TMEM158 protein). Three independent experiments were performed and are shown as individual graphs (upper, middle and lower row). Abbreviations: hFc, human fraction crystallizable (antibody fragment).

4.9 Production of BINP-CAR-T cells and their transduction efficiency

To target TMEM158 positive tumor cells, a second-generation CAR was generated, using BINP as antigen binding domain. BINP was connected to an IgG4-linker, to create enough space for BINP to bind a target protein, as well as a CD8a transmembrane domain and intracellular signaling domains from CD28 and CD3 that activate T cells when the CAR molecule binds a target protein. Based on the pCCL-BINP-WT-CAR plasmid, different versions of the CAR were produced, in which different amino acid positions were exchanged with alanine to generate less- or -non-functional CARs. In addition, a version containing an RGD motif to potentially enhance binding properties was produced through site-specific mutagenesis (Figure 5A). Viral particles were generated by introducing one of the pCCL-plasmids and corresponding packaging plasmids into 293T cells by lipofection and harvesting the supernatant. PBMCs were stimulated and transduced with the different types of viral particles to produce CAR- or control-T cells. The transduction efficiency of all CAR-T variants was determined by staining of the Δ NGFR detection marker, which is co-expressed with the CAR, using a fluorescein isothiocyanate (FITC)-labeled antibody followed by flow cytometry. The percentage of Δ NGFR⁺-cells is referred to as transduction rate in the following chapters of this work. In the different BINP-CAR-T cell versions, the transduction rates ranged between 15 % and 50 %, while up to 77 % of the pCCL-control-T cells were stained positive for Δ NGFR. Transduction ratios of two different donors are shown in Fig. 15A-C. Taken together, production of viral particles and transduction of T cells worked with all constructs at suitable ratios, although differences between the vectors and possibly between blood donors was observable.

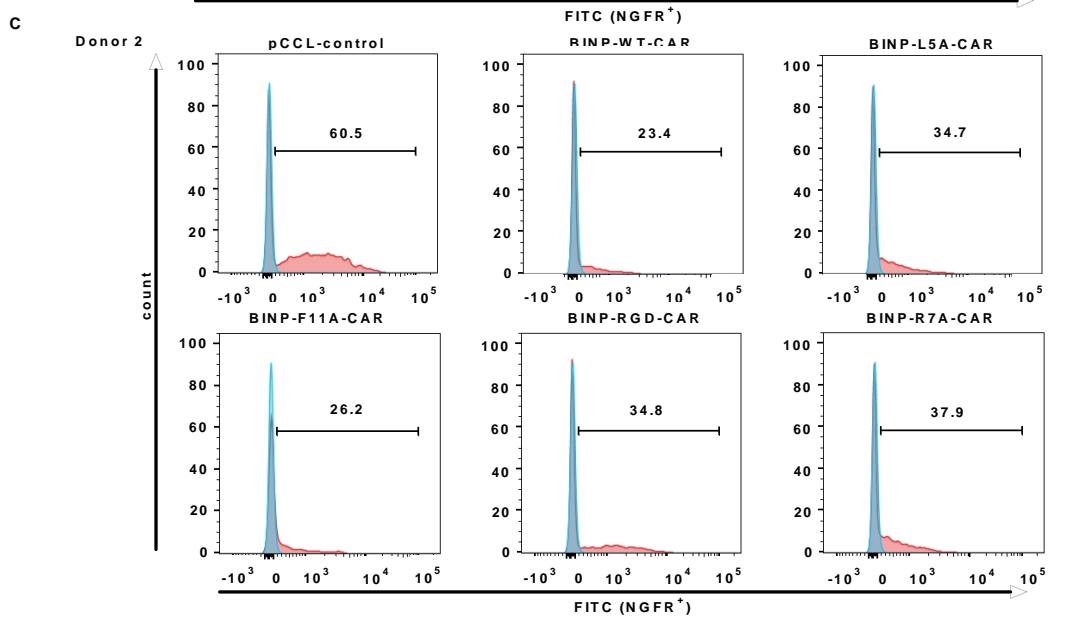
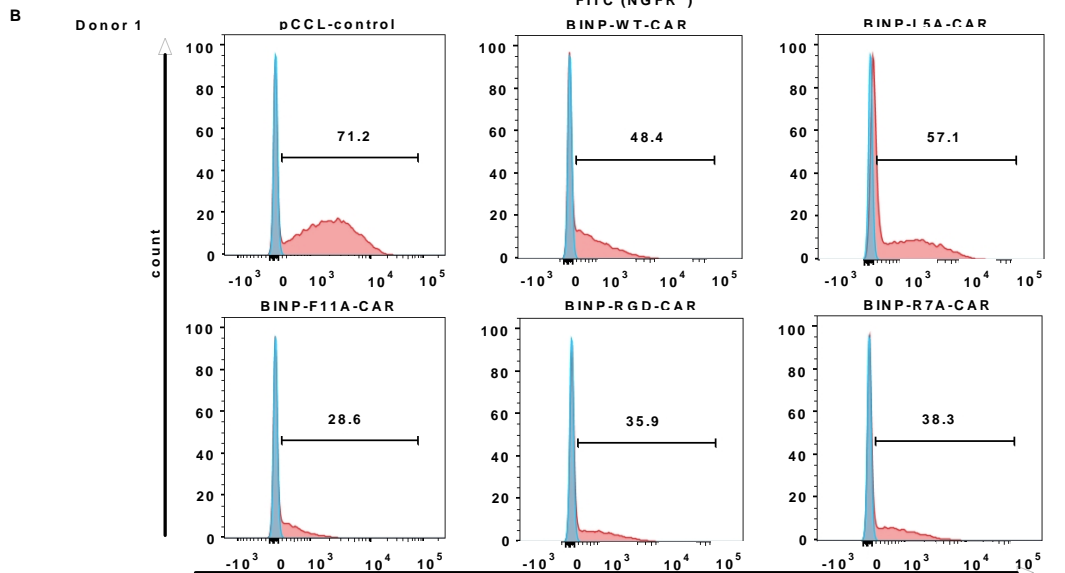
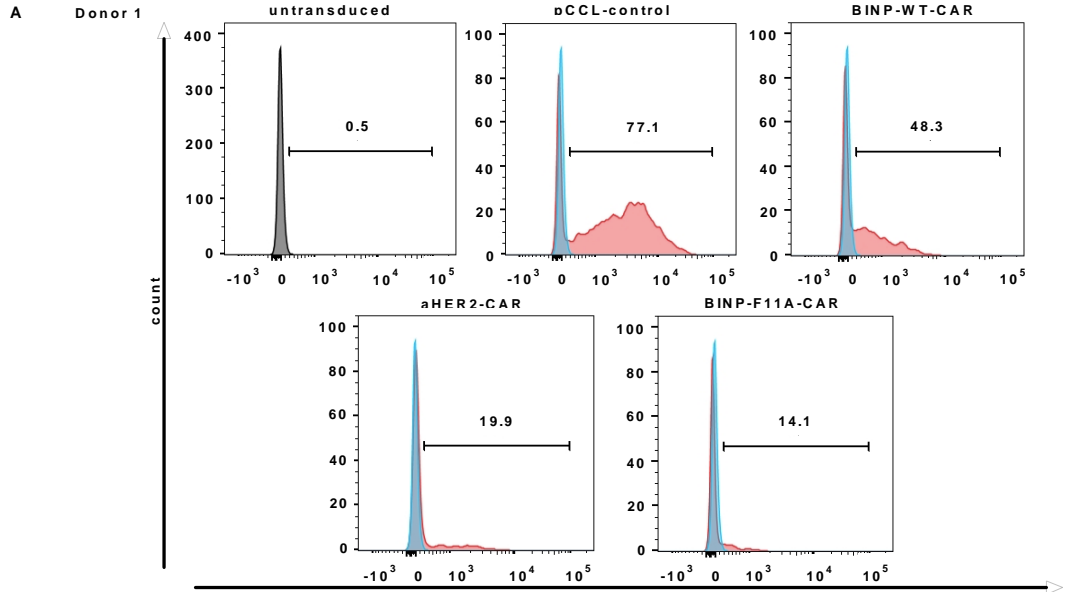


Figure 15: Transduction rates of BINP-CAR-T cells A) – C) Transduction rates of CAR- and control-T cells. T cells were transduced at an MOI of 4, except for the BINP-F11A-CAR-T cells of donor 2, which was transduced at MOI 3.5 because of a low virus titer. Cells of each group were stained with an antibody (CD271 (LNGFR) -Viobright FITC antibody) against the Δ NGFR protein, which is co-expressed with the CARs and served as detection marker. Percentage of cells positive for the Δ NGFR was determined by flow cytometry (numbers depicted in each graph). Cells from donor 1 (A/B) and 2 (C) are shown as histograms. Abbreviations: aHER2, anti-human epidermal growth factor receptor 2; BINP, brain injury-derived neurotrophic peptide; CAR, chimeric antigen receptor; Δ NGFR, truncated p75 nerve growth factor receptor (missing large parts of the cytoplasmic tail).

4.10 Cytotoxicity of BINP-CAR-T cells against cell lines

To analyze the function of the CARs, cytotoxicity against GBM cells co-cultivated with T cells was investigated by measuring luminescence emitted by living tumor cells. In a first experiment, cytotoxicity of pCCL-control-, aHER2-, BINP-WT-, and BINP-F11A-CAR-T cells against T98G, a GBM cell line with high binding of BINP (Fig. 12), was determined after 24, 28 and 44 hours of co-culture. The result of this experiment is presented in Figure 16A.

First, it was important to determine if the pCCL-control-T cells were suited as control in this assay. After 24 hours, cytotoxicity lower than 0 % was observed for the pCCL-control-T cells at effector-to-target (E:T) ratios of 0.5 to 2, while cytotoxicity increased to 32 % at E:T ratio of 8 (Note: Negative cytotoxicity indicates lower luminescence signals in wells with cells not co-cultivated with CAR-T cells compared to target cells cultivated in their presence; for details see discussion). The range of cytotoxicity mediated by the pCCL-control-T cells indicates their general functionality, but at the experimental parameters used for further experiments (E:T ratio up to 4 and 24-hour incubation) cytotoxicity is low enough to be used as control.

Next, it was of interest to analyze the difference between two BINP-CAR-T cell versions in comparison to the pCCL-control-T cells and the published aHER2-CAR-T cells, which served as reference for high cytotoxicity. In comparison to the pCCL-control-T cells, BINP-WT-CAR-T cells mediated significantly higher cytotoxicity at each E:T ratio after 24 hours ($p < 0.0001$). In presence of the aHER2- or BINP-F11A-CAR-T cells, cytotoxicity was significantly higher than observed for the pCCL-control-T cells and also higher than the BINP-WT-CAR-T cells at all E:T ratios ($p < 0.0001$) (Fig. 16A left). Cytotoxicity of the aHER2- and BINP-F11A-CAR-T cells were almost identical at E:T ratios of 4 and 8 and differed less than 10 % at all E:T ratios lower than that.

In summary, increasing cytotoxicity is visible between E:T ratios of 0.5 to 4, while separation of cytotoxicity of the different (CAR-) T cells is best at E:T ratios of 2 and 4. Therefore, it was decided to include only E:T ratios of 0.5 to 4 in following experiments.

In the first series of experiments (Fig. 16A), it was also determined how the cytotoxicity of each type of (CAR-) T cell changes with co-cultivation longer than 24 hours. After 28 hours of co-culture, cytotoxicity of the pCCL-control-T cells was very comparable to cytotoxicity seen after 24 hours at all E:T ratios. After 44 hours of co-culture, cytotoxicity of the pCCL-control-T cells decreased at low E:T ratios of 0.5 and 1, while it was unchanged at E:T ratio of 2 and increased at high E:T ratios of 4 and 8 in comparison to earlier time points. Cytotoxicity of the BINP-WT-CAR-T cells after 28 hours was almost identical with cytotoxicity after 24 hours and increased about 10 % at all E:T ratios higher than 1 after 44 hours compared to cytotoxicity at earlier time points. Cytotoxicity of the aHER2- and BINP-F11A-CAR-T cells at E:T ratios of 0.5 to 2 further increased after 28 and 44 hours. Since after 24 hours cytotoxicity of the aHER2- and BINP-F11A-CAR-T cells already reached about 95 % at E:T ratios of 4 and 8, and cytotoxicity of the pCCL-control-T cells increased to about 40 and 70 % at E:T ratios of 4 and 8, it was decided to compare cytotoxicity only after 24 hours of co-cultivation in the following experiments.

In subsequent experiments, cytotoxicity of all BINP-CAR-T cell versions against cell lines with differing TMEM158 expression was analyzed after 24 hours of co-culture to determine the influence of each individual amino acid exchange. First, cytotoxicity against T98G cells, which showed the highest BINP binding in flow cytometry (Fig. 12) was determined. With cells from donor 1 (Fig. 16B), significant cytotoxicity against T98G was observed for the BINP-WT-CAR-T cells at E:T ratios higher than 1 in comparison to pCCL-control-T cells. As seen before, significant cytotoxicity of the BINP-F11A-CAR-T cells was observed in comparison to the pCCL-control- and also the BINP-WT-CAR-T cells at all E:T ratios ($p < 0.0001$). The BINP-RGD-CAR-T cells mediated significant cytotoxicity at an E:T ratio of 4 and a tendency towards higher cytotoxicity at E:T ratio of 2 in comparison to the pCCL-control-T cells. No significant difference in cytotoxicity was found in comparison to the BINP-WT-CAR-T cells (Fig. 16B, upper left). In a following experiment using T cells from a different donor (Fig. 16C), cytotoxicity of the BINP-RGD-CAR-T cells was significantly higher than the cytotoxicity of the pCCL-control- and BINP-WT-CAR-T cells (Fig. 16C, upper left)

Cytotoxicity of the BINP-L5A-CAR-T cells against T98G was significantly higher in comparison to pCCL-control-T cells at E:T ratios 2 and 4. Also a tendency for higher cytotoxicity at E:T ratios 0.5 and 1 was observed. No significant difference to the cytotoxicity of the BINP-WT-CAR-T cells was noticeable at any E:T ratio for cells of donor 1 (Fig. 16B, lower left). Cytotoxicity of the BINP-L5A-CAR-T cells from donor 2 mediated significantly higher cytotoxicity at E:T ratio of 4 and showed a tendency towards higher cytotoxicity at E:T ratio of 2 in comparison to the BINP-WT-CAR-T cells (Fig. 16C, lower left). Cytotoxicity of the BINP-R7A-CAR-T cells was lower than the cytotoxicity of the pCCL-control-T- or BINP-WT-CAR-T cells at any E:T ratio but showed a dose dependency between E:T ratio and cytotoxicity (Fig. 16B, lower left). Interestingly, the BINP-R7A-CAR-T cells of donor 2 showed a significantly higher cytotoxicity against T98G in comparison to the BINP-WT-CAR-T cells at all E:T ratios except 1 (Fig. 16C, lower left).

In conclusion, all BINP-CAR-T cells, especially the BINP-F11A-CAR-T cells, showed significantly higher cytotoxicity against T98G cells at E:T ratios higher 1 in comparison to the pCCL-control-T cells.

Next, it was of interest to analyze cytotoxicity against U-87 MG, a GBM cell line with high surface expression of integrin $\alpha V\beta 3$ (Fig. 13). The BINP-WT-CAR-T cells didn't show higher cytotoxicity than the pCCL-control-T cells at any E:T ratio. Cytotoxicity of the BINP-F11A-CAR-T cells was significantly higher than cytotoxicity of pCCL-control-, BINP-WT-, BINP-L5A-, or BINP-R7A-CAR-T cells at E:T ratio of 0.5 but not at higher E:T ratios. The BINP-RGD-CAR-T cells in contrast, mediated significantly higher cytotoxicity against U-87 MG cells in comparison to the pCCL-control-T cells at all E:T ratios except 4 and also in comparison to all other BINP-CAR-T cell variants at all E:T ratios (Fig. 16B, upper middle). Cytotoxicity of the BINP-L5A- and BINP-R7A-CAR-T cells was not significantly higher than cytotoxicity of the BINP-WT-CAR-T cells at any E:T ratio (Fig. 16B, lower middle). In summary, of all CAR-T cell versions, only the one containing the RGD motif showed significantly higher cytotoxicity against U-87 MG at several E:T ratios, in comparison to the pCCL-control-T cells.

Finally, cytotoxicity of the (CAR-) T cells was determined against SH-SY5Y, a cell line for which low binding of BINP as well as low surface expression of integrin $\alpha V\beta 3$ (Fig. 13) was detected. The BINP-WT-CAR-T cells didn't show higher cytotoxicity than the pCCL-control-T cells at any E:T ratio.

Cytotoxicity of the BINP-F11A-CAR-T cells was significantly higher as observed for the pCCL-control-T cells at an E:T ratio of 0.5, but only a tendency towards higher cytotoxicity was found at E:T ratios of 1 and 2. In comparison to the BINP-WT-CAR-T cells, cytotoxicity mediated by the BINP-F11A-CAR-T cells was significantly higher at each E:T ratio, although the difference was only about 20 %. The BINP-RGD-CAR-T cells showed a similar cytotoxicity, with a tendency towards higher cytotoxicity in comparison to the pCCL-control-T cells at all E:T ratios except 4. In comparison to the BINP-WT-CAR-T cells, cytotoxicity mediated by the BINP-RGD-CAR-T cells was significantly higher at all E:T ratios except 4 (Fig. 16B, upper right). No significantly higher cytotoxicity was found, though, for BINP-RGD-CAR-T cells from donor 2 in comparison to the pCCL-control- or BINP-WT-CAR-T cells (Fig. 16C, upper right). Cytotoxicity of the BINP-L5A- and BINP-R7A-CAR-T cells against SH-SY5Y was not significantly higher as cytotoxicity of the pCCL-control- or BINP-WT-CAR-T cells at any E:T ratio (Fig. 16B, lower right). In conclusion, no cytotoxicity higher than observed for the pCCL-control-T cells was seen against SH-SY5Y in the BINP-WT-, BINP-L5A- and BINP-R7A-CAR-T cells, while a significantly higher cytotoxicity of the BINP-F11A- and BINP-RGD-CAR-T cells was found. But still, cytotoxicity of those two CAR-T cell versions was below 20 % at all E:T ratios.

All in all, compared to the pCCL-control-T cells, significant cytotoxicity against T98G was observable for all CAR-T cell versions at E:T ratios of 2 to 4 and lower E:T ratios in some of the CAR-T cell versions. Against U-87 MG, only the BINP-RGD-CAR-T cells showed significant cytotoxicity at several E:T ratios in comparison to the pCCL-control-T cells and none of the CAR-T cells showed significant cytotoxicity against the SH-SY5Y cell line at E:T ratios higher than 0.5.

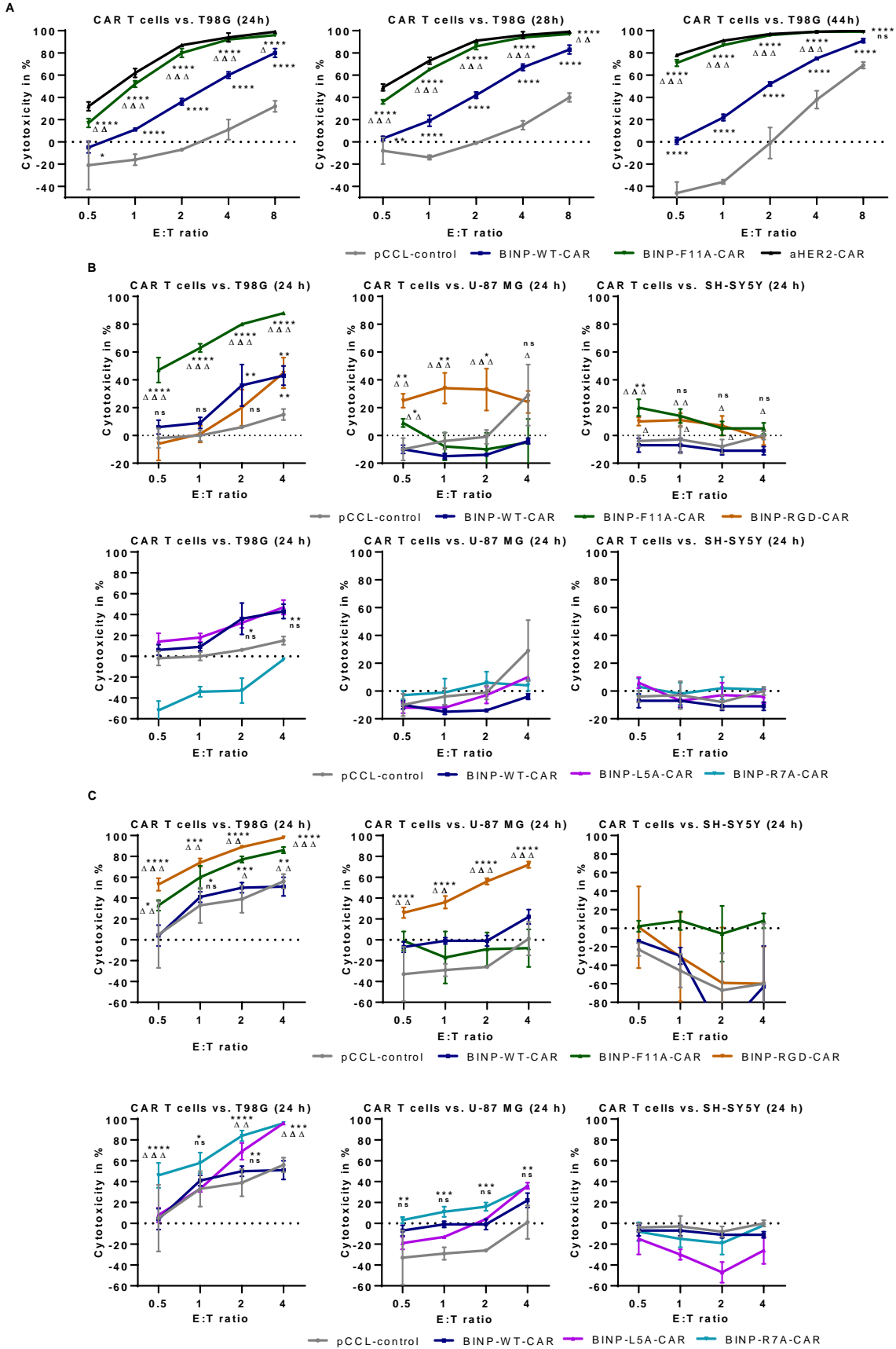


Figure 16: Cytotoxicity of BINP-CAR-T cells **A)** Cytotoxicity of BINP-CAR-T cells from donor 1 (transduction rates see Fig. 15A) against T98G at different time points and different effector-to-target ratios. Bioluminescence of cells was measured at indicated time points, shortly after addition of D-luciferin. Cytotoxicity was calculated from the difference of bioluminescence between wells with tumor cells only and wells containing both tumor- and T cells. The ratio between T- and tumor cells is designated as effector-to-target (E:T) ratio. In this experiment E:T ratios of 0.5 to 8 were analyzed. Shown is an experiment with T cells from one donor in technical triplicates. Data is presented as mean \pm SD cytotoxicity. **B) / C)** Cytotoxicity of BINP-CAR-T cells from donor 1 (B, transduction rates see Fig. 15B) or from donor 2 (C, transduction rates see Fig. 15C) against the GBM cell lines T98G and U-87 MG and towards the neuroblastoma cell line SH-SY5Y. T cells and tumor cells were co-cultivated at E:T ratios of 0.5 to 4. Bioluminescence of cells was measured at indicated time points, shortly after addition of D-luciferin. Shown is one of two experiments performed with cells from different donors in technical triplicates. Data is shown as mean \pm SD cytotoxicity. Statistical significance was calculated by Tukey's multiple comparison test and are illustrated as * for $p < 0.05$, ** for $p < 0.01$, *** for $p < 0.001$, **** for $p < 0.0001$ for comparison of a group with the pCCL-control or as Δ for $p < 0.05$, $\Delta\Delta$ for $p < 0.01$, $\Delta\Delta\Delta$ for $p < 0.001$, $\Delta\Delta\Delta\Delta$ for $p < 0.0001$ for comparison of a group with the BINP-WT-CAR. Due to lack of space, significance is only depicted for selected conditions.

5 Discussion

5.1 Gene- and protein-expression of *TMEM158*

A hallmark of Glioblastoma is its extensively interpatient and intra-tumoral antigen heterogeneity^{151,152}. Discovery of novel tumor antigens is urgently needed to enable efficient treatment of patients. Until recently, *TMEM158* was not known as tumor antigen of GBM. Gene-expression of *TMEM158* in GBM and other brain tumor entities in different public databases was analyzed. A higher expression of *TMEM158* in GBM in comparison to healthy brain tissue or LGG as well as a negative correlation of survival with high expression of *TMEM158* was found (Figure 7). Those findings were recently confirmed by Li et al.¹³⁵. In an additional analysis by Dr. Jana Burkhardt, expression in different low- and high-grade brain tumor entities was compared. Gene-expression of *TMEM158* was significantly higher in GBM in comparison to low-grade glioma ($p < 0.0001$). Expression in neoplasm paragangliomas was found to be about 10-times lower in comparison to GBM ($p < 0.0001$) and more than 10-times lower in neuroblastoma ($p < 0.0001$) (Fig.18A, 8.2 Appendix)

Li et al. also found that *TMEM158* is associated with epithelial–mesenchymal transition (EMT) as well as higher invasiveness and growth of GBM¹³⁵. Those characteristics are also associated with the mesenchymal GBM subtype²⁶. One key marker of this particular GBM subtype is *CD44*¹⁵³. Based on the TCGA dataset, a moderate correlation between gene-expression of *TMEM158* and *CD44* ($R = 0.44$) was observed within this work. This finding raises the question if *CD44* and *TMEM158* interact on a molecular level or are part of an identical pathway.

To further validate the overexpression of *TMEM158* in GBM, a dataset from a well-defined local cohort was analyzed. In this dataset, also overexpression of *TMEM158* in GBM in comparison to healthy brain tissue was found. Furthermore, OS of patients with *TMEM158* expression higher or lower than the median expression was compared (Fig. 8C). No difference in survival was seen between both patient groups. When OS of GBM patients from the TCGA dataset is compared without LGG samples, also no difference is seen (Figure 18C, 8.2 Appendix). However, a significant difference in OS was seen when LGG and GBM samples are combined in the analysis.

Also, a significant difference in *TMEM158* expression was observed between LGG and GBM, suggesting that even in GBM samples with expression below the median, the negative influence on survival is too high to detect a difference to the samples with expression higher than the median.

In addition, a significantly lower expression in tumors with *IDH1*^{mut} was found (Figure 8B). A correlation between *TMEM158* and *IDH1* expression was also identified in the TCGA GBM dataset¹³⁵. Interestingly, it was reported that overexpression of *IDH1* induces resistance to high doses of TMZ *in vivo* and *in vitro*¹⁵⁴. In a different study, it was demonstrated that expression of branched-chain amino acid transaminase 1 (BCAT1), which catabolizes branched-chain amino acids, was dependent on *IDH1*^{WT} expression. Suppression of BCAT1 reduced release of glutamate and invasiveness *in vitro* as well as tumor growth *in vivo*¹⁵⁵. In non-small cell lung cancer¹³¹ and colorectal cancer¹³⁰, *TMEM158* was found to mediate chemoresistance, raising the question whether this is also the case for glioblastoma. If so, targeting of *TMEM158* might be even more feasible, considering that *TMEM158*⁺ cells might become enriched after chemotherapy. Furthermore, eliminating cells positive for this target before or during chemotherapy might also increase the therapeutic effect of TMZ.

TMEM158 protein expression was also analyzed in GBM cell lines by Western blot to confirm overexpression at the protein level (Figure 11). *TMEM158* protein was found in all GBM cell lines and in SH-SY5Y with low signal compared to T98G. Specificity of the antibody was confirmed by DsiRNA based knockdown of *TMEM158*. The observed protein size was larger than expected, indicating a possible post-translational modification of the protein. Glycosylation of *TMEM158* was demonstrated within the Bachelor thesis of a group member, Fabian Flemig, by PNGase F-based deglycosylation and subsequent Western blot analysis¹⁵⁶. Several bands of *TMEM158* were observed below the band mainly seen in samples of non-deglycosylated protein, including one band at the predicted size for not glycosylated protein of about 40 kDa (Figure 20, 8.4 Appendix).

As a suitable antibody for the detection of surface expression of *TMEM158* (with intact folding) on target cells was not commercially available at the time the flow cytometry experiments were performed, a labeled version of the natural ligand BINP was used instead. Differing levels of BINP binding to the different cell lines were found, with T98G showing a high signal while SH-SY5Y showed only a low signal (Figure 12A/B).

Specific staining of T98G by the labeled BINP is also confirmed by reduction of signal in flow cytometry after a (partial) knockdown (Fig. 22A/B, 8.6 Appendix). Staining of the U-87 MG cell line using BINP might be unspecific, since the cells showed a high signal after staining with the scrambled BINP.

At this point, it should be noted that hydrophobicity is the main driver for unspecific binding of fluorescent dyes to cell membranes^{157,158}. In fact, Rhodamine B that was used to label BINP, has previously been used to model the adsorption of hydrophobic small molecules to hydrophobic materials¹⁵⁹, therefore, the possibility that it might also unspecifically bind to cells with a highly hydrophobic cell surface cannot be ruled out.

In summary, mRNA overexpression of *TMEM158* in GBM was confirmed and protein expression was detected in total protein extracts as well as on the surface of the cells. Surface protein expression appears to be high enough to enable targeting by a CAR-immunotherapy. Also, a possible involvement of *TMEM158* in chemoresistance and association with higher mortality enhances the potential therapeutic value.

5.2 Production of recombinant *TMEM158*

The extracellular part of *TMEM158* was produced as a recombinant Fc-fusion protein to show binding of BINP to *TMEM158* and to determine affinity. The size of the protein was larger than the size of 55.75 kDa, calculated by a web-based tool¹⁶⁰ for the not post-translationally modified protein. Since it was already observed that *TMEM158* is glycosylated in different human cell lines, and because 293T cells were used for expression in order to preserve human post-translational modifications, this was expected. The deviation between calculated and observed size was about the same for the isolated and the recombinant protein, indicating that no complete change in post-translational modification was induced by the expression system (Figure 14A).

By transient transfection and extraction of the fusion protein from the cell pellet, only amounts smaller than 0.2 mg per batch were yielded. In the literature, other expression systems using 293T cells yield up to about 16 mg/L when protein is secreted and isolated from culture medium¹⁶¹. Enhancing protein production might help to improve reproducibility of functional tests of the recombinant *TMEM158*-hFc protein and might possibly enable detailed structural analysis. Therefore, changing to optimized expression vector systems and culture conditions should be used for further protein batches.

In a preliminary assay, binding of labeled BINP to the recombinant protein was demonstrated, suggesting correct folding of the recombinant protein (Figure 14B). It was observed that binding of the scBINP was higher in wells without immobilized TMEM158-hFc protein, than seen for BINP. Normalization was performed to equalize this difference in non-specific binding for better comparison of the peptide's signal. A logarithmic fitting of the curves was chosen, since for this data it appeared to come closest to a typical binding curve. Still, it has to be taken into account that three data points don't allow an error-free fitting. Therefore, no precise binding affinity (K_D) was calculated.

In the future, variants of BINP with exchanged possibly functionally relevant amino acids to structurally inert alanine could shed further light on BINP structure and function in general.

5.3 Production and cytotoxicity of BINP-CAR-T cells

Since binding of BINP against T98G was detected by flow cytometry, a CAR against TMEM158 was designed, using BINP as binding domain, which was then introduced into T cells by lentiviral transduction. Transduction levels of the CAR-T cells were comparable to other studies using the pCCL vector system^{143,144} (Figure 16A-C).

First, it was noticed that varying intensity of cytotoxicity was also mediated by the pCCL-control-T cells dependent on the different donors. Those cells don't express a CAR but were stimulated in the same way as the CAR-T cells. Cytotoxicity of stimulated T cells against tumor cell lines is typically observed because of alloreactivity and known to be donor-dependent¹⁶².

A published anti-HER2-CAR¹⁴⁵ was included in the analysis as reference for a well-functioning CAR that should mediate high cytotoxicity against an ERBB2 (HER2) positive cell line. Significant cytotoxicity against T98G was observed for the aHER2-CAR-T cells. This was expected, since expression of HER2 on T98G cells was shown in different studies^{163,164}. No expression of HER2 was found on U-87 MG or SH-SY5Y in other studies¹⁶³⁻¹⁶⁶. Therefore, cytotoxicity of the aHER2-CAR-T cells against those cell lines was not determined.

Significant cytotoxicity of the BINP-WT-CAR-T cells against T98G, which showed binding of BINP in flow cytometry, was detected in comparison to pCCL-control-T cells.

No significant cytotoxicity of the BINP-WT-CAR-T cells was found though against U-87 MG or SH-SY5Y in comparison to the pCCL-control-T cells (Figure 16). Since U-87 MG cells also showed a high signal after staining with the scrambled BINP, the missing cytotoxicity against this cell line further supports the notion that staining of U-87 MG with the labeled BINP peptides was unspecific.

Cytotoxicity mediated by the pCCL-control-T cells and some of the BINP-CAR-T cell versions appeared to be negative, especially against SH-SY5Y. Negative cytotoxicity can arise when luminescence of wells containing only tumor cells is lower than in wells containing tumor and T cells. One very likely reason for that might be differences in target cell growth between wells with and without T cells. Since 12,500 target cells were seeded per well about 16 hours before adding (CAR-) T cells, after additional 24 hours of (co-) cultivation, confluency might be reached in wells without cytotoxicity against a target cell line. In case cells would detach with higher frequency in wells containing T cells in comparison to wells with only target cells, negative cytotoxicity would appear when cells re-grow. Highest negative cytotoxicity was observed for the SH-SY5Y cell line that is known to grow semi-adherent with individual cells detaching spontaneously^{167,168}. Since SH-SY5Y cells are not killed by the CAR-T cells because of the missing binding of BINP and integrin expression, and because of their susceptibility for detachment, negative cytotoxicity seems very plausible for this cell line. In future experiments the occurrence of negative cytotoxicity can probably be omitted by irradiation of the cells as this prevents target cell growth in co-culture^{53,169}. In addition, the use of more advanced image-based cytotoxicity assays, such as assays that can measure cytotoxicity in 3D cultures, might be an alternative, especially as some of these more advanced assays also allow the measurement of cytotoxicity over time^{170,171}.

Furthermore, different versions of the CAR, which contain either alanine in different positions of BINP or one version containing an RGD motif converted from an RGA sequence originally present in BINP were tested. The exchanged amino acid positions were predicted to be relevant for the binding of BINP to TMEM158 by an *in silico* modelling performed by Dr. Galina Denisova at McMaster University, Hamilton, Canada (Fig. 25, 8.9 Appendix). In this analysis also no relevant influence of the exchange to complete the RGD motif (A9D) on TMEM158 binding was seen.

The BINP-L5A-CAR-T cells of one donor exhibited significantly higher cytotoxicity than the BINP-WT-CAR-T cells at E:T ratio 4 against T98G cells, but no significantly different cytotoxicity was seen at other E:T ratios, for cells of the other donor, or against U-87 MG or SH-SY5Y. For the BINP-R7A-CAR-T cells, cytotoxicity against T98G was lower than mediated by the BINP-WT-CAR-T at all E:T ratios but was significantly higher at all E:T ratios except 1 when cells of donor 2 were tested. Cytotoxicity of the BINP-R7A-CAR-T cells was not significantly different from cytotoxicity of the BINP-WT-CAR-T cells against U-87 MG or SH-SY5Y at any E:T ratio. In conclusion, this data suggests that the L5A didn't influence the function of the BINP-CAR. To draw a final conclusion about the function of the BINP-R7A-CAR that induced very contrary cytotoxicity with cells of the two different donors, another repetition with a different donor is required.

Interestingly, it was observed that the BINP-F11A-CAR mediated drastically enhanced cytotoxicity (92 % at E:T ratio of 4) against T98G cells in comparison to the BINP-WT-CAR (60 % at E:T ratio of 4). The cytotoxicity of the BINP-F11A-CAR-T cells was on the same level as the aHER2-CAR-T cells at all E:T ratios above 1 after 24 hours, suggesting a high functionality of the BINP-F11A-CAR-T cells. Cytotoxicity against U-87 MG was not significantly higher than observed for the BINP-WT-CAR or pCCL-control-T cells except at an E:T ratio of 0.5 for one donor. Cytotoxicity of the BINP-F11A-CAR-T cells against SH-SY5Y was significantly higher than the cytotoxicity of BINP-WT-CAR or pCCL-control-T cells at some E:T ratios but in general didn't show cytotoxicity higher than about 20 % at any E:T ratio. In summary, the F11A amino acid exchange increased cytotoxicity of the BINP-CAR against the T98G cell line, which showed highest binding of BINP before. Since no increase in cytotoxicity against the SH-SY5Y cell line, which showed the lowest binding of BINP, was observed, the selectivity of the CAR not to attack cells with presumably low expression of TMEM158 seems to be intact.

To draw further conclusions about the influence of the amino acid exchanges of the different BINP-CAR versions on binding properties and mediated T-cell activation, the exact affinities for TMEM158 have to be determined in future assays.

It was demonstrated that affinity and avidity of CARs towards an antigen strongly influence the function of CAR-T cells⁵². In general, higher affinity of CARs results in higher cytotoxicity against target cells *in vitro*.

However, it was shown that too high affinity can lead to reduced proliferation and thereby a lower therapeutic effect *in vivo*^{51,52}. Therefore, proliferation assays should be performed to predict the *in vivo* efficiency of a CAR. Moreover, it might therefore also be more beneficial to perform cytotoxicity assays using low E:T ratios for one to two days instead of high E:T ratios and co-cultivation times of less than one day, as it was done in different publications^{67,172}.

In parallel to the amino acid exchanges to alanine, an RGD motif was introduced into a separate version of the BINP-CAR, since this motif is known to bind to certain integrins such as $\alpha V\beta 3$ or $\alpha V\beta 6$ that are also targeted as GBM antigens^{75,173,174}. Introduction of an RGD motif might enable attacking of both targets in parallel, comparable to a tandem CAR.

High expression of integrin $\alpha V\beta 3$ was detected in U-87 MG by flow cytometry, as also confirmed recently¹⁷⁵, and a significantly increased cytotoxicity of the BINP-RGD-CAR-T cells against U-87 MG was observed in comparison to the pCCL-control- or BINP-WT-CAR-T cells at E:T ratios of 0.5 to 2. For T cells of one donor, a significant difference to the BINP-WT-CAR-T cells was observed against T98G at all E:T ratios and against SH-SY5Y at an E:T ratio of 0.5. The $\alpha V\beta 3$ integrin was targeted before by a CAR that contains a natural ligand with a single RGD motif as binding domain¹⁷⁶. Based on our data, it seems very likely that a single RGD motif included in the BINP-CAR is also sufficient to enhance cytotoxicity against integrin $\alpha V\beta 3$ positive cell lines. This might open up the opportunity for dual targeting when RGD-BINP is used as antigen binding domain. It has to be considered though that RGD binds to multiple proteins, which might lead to an increased risk of off-tumor effects. In one study an RGD-based CAR was tested on a murine ovarian-, breast, and pancreatic tumor xenograft model, and mild toxicities were only evident at a supra-therapeutic dose¹⁷⁷. It was also found by immunohistology analysis that no integrin $\alpha V\beta 3$, $\alpha V\beta 5$ or $\alpha V\beta 6$ is present in normal brain tissues¹⁷⁸, although it is described that at least 8 different integrins can be bound by RGD¹⁷⁹ and might thereby lead to off-tumor effects when using RGD-based therapeutics. Different studies used labeled versions of RGD containing peptides for imaging of rodents¹⁸⁰ and humans¹⁸¹ and did find only minimal accumulation in the brain, but in those studies, the molecules were injected intravenously into the body, and the blood brain barrier was intact. Since the RGD peptide doesn't pass the blood brain barrier well¹⁸², binding of normal brain tissue cannot be ruled out by those studies.

Clinical data for a cytotoxic RGD-based therapy is not available yet, so in the future, studies to quantify binding of RGD-BINP to healthy human tissue should be performed. In further experiments done by Dr. Burkhardt (part of the pending publication associated with this work), cytotoxicity of BINP-WT-CAR-T cells against the ovarian carcinoma cell line OVCAR3 and the triple-negative breast cancer cell line MDA-MB231 was detected (Figure 23, 8.7 Appendix). In those highly aggressive types of cancer TMEM158 was also shown to be overexpressed^{127,132}.

Furthermore, BINP-WT-CAR-, pCCL-IgG-control-CAR- and untransduced T cells were compared in a murine xenograft glioblastoma model by Dr. Jana Burkhardt in cooperation with the group of Prof. Jonathan Bramson (McMaster University, Hamilton, Canada). T98G cells were injected subcutaneously into the flank of NOD rag gamma (NRG) mice and CAR-cells were injected intratumorally when the tumor size reached an appropriate size of about 100 mm³. Mice treated with pCCL-control-CAR-T cells or untransduced T cells reached unbearable tumor sizes > 500 mm³ within 35 days, while 75 % of all mice treated with BINP-WT-CAR-T cells were still alive at this point. Half of the mice treated with BINP-WT-CAR-T cells survived until the end of the experiment at day 100, displaying long-term survival and significantly reduced tumor volume (Figure 24, 8.8 Appendix). This data demonstrates that the BINP-CAR is functional *in vivo* and is able to treat aggressive glioblastoma.

A subcutaneous GBM model using T98G cells in NRG mice is so far not published but in comparable models with different cell lines and mice strains control mice also died between day 20 and 40 after treatment. An NK92-based CAR against HER2 induced survival of 60 % of treated mice for 120 days in comparison to untreated mice that died within 40 days¹⁸³, while CAR-T cells targeting EGFR and EGFRvIII in parallel induced survival until day 60 in 33 % of treated mice¹⁸⁴. The survival of mice treated with the BINP-CAR is within the range of both studies. An alternative to the existing model would be to use murine GL-261 cells in a syngeneic model of immunocompetent mice, since this cell line is also positive for TMEM158 according to our Western blot analysis. Alignment of the human and murine protein sequence revealed a high homology (Figure 26, 8.10 Appendix), especially in the area predicted to be important for BINP binding, according to the *in silico* modeling (Figure 25, 8.9 Appendix). Therefore, cross reactivity of the BINP-CAR against GL-261 seems to be very likely.

Testing the CAR-T cells in a syngeneic model would be advantages because the host immune system is completely functional and might allow identification of additional insights about the CARs function. To test the CAR-T cells under conditions that resemble the disease in patients better, an orthotopic model based on patient derived tumor cells should be performed.

5.4 Gene- and protein-expression of PTPRZ1

PTPRZ1 is already described as a promising marker that might allow treatment of glioblastoma⁸⁷. Gene-expression of *PTPRZ1* was analyzed based on public databases, and overexpression in GBM and low-grade glioma in comparison to healthy tissue, as published by others⁸⁷, was also found in this work (Figure 9). In a more detailed analysis by Dr. Jana Burkhardt, *PTPRZ1* expression was analyzed in different low- and high-grade brain tumor entities and a significantly higher expression in all gliomas in comparison to paraganglioma ($p < 0.0001$) and neuroblastoma ($p < 0.0001$) was found, while neuroblastoma also showed about 20-times lower average expression than paraganglioma ($p < 0.0001$). No difference in expression was observed between glioma subgroups (Fig. 18B, 8.2 Appendix). Overexpression in low-grade glioma might be an indicator that a CAR-therapy against this marker would allow treatment of a larger subset of patients but also hints at a lower association with aggressiveness of cancers in comparison to *TMEM158*.

Also, *PTPRZ1* expression was measured in a local GBM cohort, and its overexpression was observed in comparison to healthy brain tissue (Figure 10A/B). Further correlation between *PTPRZ1* expression and clinical parameters were not observed. Glioma patients (GBM and LGG) with high *PTPRZ1* expression showed lower survival in contrast to patients with low expression as found in the public databases, although the hazard ratio was not as high as observed for *TMEM158*. No difference in OS was seen between GBM patients from the local cohort when patient groups with *PTPRZ1* expression lower and higher than the median were compared (Fig. 10C). In the TCGA data set, also no significant difference was observed between those groups when OS of GBM patients was analyzed without including LGG (Fig. 18D, 8.2 Appendix). As also observed for *TMEM158*, even in the group with *PTPRZ1* expression below the median, expression might be too high to identify a significant increase of OS.

Although several publications found an association of PTPRZ1 with stem cell properties of tumor cells⁹⁰, no correlation with the GBM stem cell marker CD44 or CD133 was identified *in silico*.

So far, it is not known whether PTPRZ1 expression is homogeneously found in all cells of a GBM, and it has not been analyzed whether there are tumor-specific differences between patients. This information appears to be important to estimate the percentage of GBM patients that might benefit from targeting PTPRZ1 by CAR-immunotherapy.

Based on fibronectin, a known binding domain of PTPRZ1 ligands, a CAR potentially targeting PTPRZ1 was designed by Dr. Jana Burkhardt. CAR-T cells were produced and cytotoxicity against GBM and other cell lines was analyzed as described in this work for the BINP-CAR. Varying levels of cytotoxicity were shown against several GBM cell lines, including significant cytotoxicity against T98G, in comparison to stimulated but untransduced T cells. Interestingly, the anti-PTPRZ1-CAR contained an RGD-motif and showed cytotoxicity against U-87 MG cells. A mutated version of the PTPRZ1-CAR with a modified motif (RGD > RGE) was designed to abolish the binding mediated by RGD, as published¹¹³. Cytotoxicity of the mutated CAR was significantly smaller against U-87 MG. This data is also in line with the data of the BINP-RGD-CAR, which showed an enhanced cytotoxicity against U-87 MG in comparison with the BINP-CARs without the RGD-motif within this work. The anti-PTPRZ1-CAR-T cells were also tested in the T98G-based animal model described earlier for the BINP-CAR. Comparable results regarding survival and reduction of tumor volume were seen for the anti-PTPRZ1-CAR-T cells. About 60 % of mice treated with those CAR-T cells survived until the end of the experiment at day 100 (Figure 27, 8.11 Appendix).

In summary, this preliminary *in vitro* and *in vivo* data show that the anti-PTPRZ1-CAR is functional and might hold great promise for the treatment of GBM. Based on this first data, a more in-depth analysis regarding cytokine release, proliferation, and function in superior animal models, like the orthotopic patient derived xenograft model described previously, is needed to optimize this CAR further and to pave the way for a possible clinical use. Several studies showed that PTPRZ1 is important for different physiological functions of the brain, including learning¹⁸⁵, memory formation^{186,187}, structuring of perineuronal nets^{188,189} and response to drugs like morphine¹⁹⁰, ethanol¹⁹¹ and methamphetamine¹⁹².

Therefore, the question could be raised if a cytotoxic cell therapy against PTPRZ1 might lead to reduction or loss of these functions. In the aforementioned studies, knockout of PTPRZ1 was performed in rodents starting from the embryonic stage. So, it is not known whether the physiological functions would also be impaired if the knockout would be performed only in adult animals. In one study, pharmacological inhibition of PTPRZ1 by a substance called MY10 didn't induce behavioral changes in mice without PTPRZ1 knockout¹⁹³, indicating that the functional impairments observed in the other studies might be mostly because of a developmental function of PTPRZ1. Regarding possible side effects of a PTPRZ1-targeting therapy, it should be considered that survival of GBM patients that have only a life expectancy of months is more important than possible impairments in their learning abilities. All in all, PTPRZ1 is a very promising target for treatment of GBM, and its potential for clinical use should be evaluated by further studies in the future.

5.5 Outlook

PTPRZ1 was already recognized as a promising target for the treatment of glioblastoma and might be a well-suited target for a CAR-based immunotherapy⁸⁷. TMEM158 seems to be a highly feasible target for immunotherapy as well, since specific overexpression in GBM and a significant influence on patient survival was found.

The physiological function of TMEM158 is not known so far, but association with several key tumor functions might be linked based on recent findings. It was reported that association of TMEM158 with EMT, increase of invasiveness and growth of GBM is activated via the STAT3 axis¹³⁵. STAT3 activates a plethora of cellular factors including c-myc, survivin, cyclin D1, hypoxia-inducible factor (HIF)-1 and vascular endothelial growth factor (VEGF)¹⁹⁴. It was also shown that STAT3 knockdown results in downregulation of MGMT, which is one of the main enzymes responsible for resistance to the chemotherapeutic temozolomide. Additionally, TGF- β , which was shown to support invasiveness, EMT and immunosuppression^{195,196}, was reduced after knockdown of TMEM158 in several cancer types¹²⁷⁻¹²⁹ or inhibition of STAT3 in lung cancer cells¹⁹⁷. Moreover, STAT3 upregulates and forms a complex with CD44^{198,199}, which itself is also associated with EMT, invasion, chemoresistance and poor patient survival^{200,201}

Since a moderate correlation between the gene expression of TMEM158 and CD44 was found in this work, an indirect activation of CD44 by TMEM158 via activation of STAT3 also seems possible.

Interestingly, STAT3 also activates glutamate aspartate transporter 1 (GLAST; EAAT1) which under healthy conditions imports glutamate into astrocytes but releases glutamate in GBM tumors when Na⁺/K⁺-ATPase activity is downregulated and the Na⁺ gradient generated by it collapses²⁰². Glutamate release is known to be an important driver of GBM invasion²⁰³. High extracellular amounts of glutamate induce excitotoxicity and cell death in surrounding neurons, which clears space for expansion of the tumor²⁰⁴.

When TMEM158 was first discovered, it was demonstrated that it protects different subtypes of rodent neurons from glutamate induced excitotoxicity when binding the peptide ligand BINP¹²¹. This data raises the question whether TMEM158 is involved in glutamate signaling or neuroprotection in humans since this function seems very likely in rodents. Different studies show that TMEM158 is also a marker for senescence¹²⁴ in which also large amounts of glutamate are released. If this holds true, TMEM158 might also be involved in ischemia, since the toxic effects of this disease are also based on glutamate induced excitotoxicity.

A high correlation of TMEM158 with chemical synapse transmission, ECM organization, skeletal system morphogenesis, neuroactive ligand-receptor interaction, calcium signaling and cytokine-cytokine receptor interactions was also found in a study, further supporting the hypothesized functions of TMEM158¹³⁵.

Taken together, all of those studies suggest that TMEM158 might be linked to different pathways responsible for the aggressive and deadly phenotype of GBM, which is initiated by glutamate release, enhanced invasion and chemoresistance.

To make sure that cytotoxicity of the BINP-CARs is specifically based on the binding of TMEM158, a knockdown should be repeated with other siRNAs to achieve a higher knockdown efficiency. An alternative might be a complete knockout, for example via genome editing. Also, TMEM158 might be overexpressed in a TMEM158⁻ cell line and also used to demonstrate specific binding. To be used as a therapeutic target, the analysis of the percentage of patients positive for the antigen and the percentage of positive cells within a tumor appear to be reasonable.

For this purpose, immunohistochemistry of tumor and healthy tissue, using reliable antibodies, should be performed. In order to move forward with the development of immunotherapies against TMEM158 and PTPRZ1, a detailed analysis of the CARs presented in this work should be performed using additional *in vitro* assays and *in vivo* models. For example, proliferation and cytokine release might be analyzed by *in vitro* co-culture assays, while invasion of tumor tissue and inactivation of CAR-T cells by the tumor milieu could be analyzed using superior animal models. As *in vivo* model preferentially a syngeneic model, encompassing intact immune functions, might be used. If off-tumor effects are observed and found to be based on healthy cells with low antigen expression, optimization of the antigen binding domain of the corresponding CAR might be feasible. For example, affinity or avidity might be reduced to increase the activation threshold. Using the recombinant TMEM158 protein, affinity of different BINP variants or other ligands might be determined by the plate-based binding assay established within this work or more sophisticated methods like surface plasmon resonance spectroscopy.

Also, the recombinant TMEM158 protein might be used to identify novel ligands by biopanning in the future. If reduction of the activation threshold is not possible, co-expression of an inhibitory receptor against a specific protein of cells, attacked during off-tumor effects, might be an option²⁰⁵. Determination of potential combination targets for TMEM158 might be interesting if future studies look promising. A possible combination with therapies against EGFR receptors like HER2/ERBB2 might be practicable, since those targets also mediate activation of STAT3²⁰⁶, which interrupts the possibility of tumors to maintain STAT3 signaling by switching expression of those targets.

In conclusion, by showing overexpression of TMEM158 in GBM and developing a first functional cell therapy against this promising new target, this work contributes to acquiring a repertoire of molecular targets and fitting tailor-made therapies that can effectively treat GBM patients in the future, despite any antigen heterogeneity.

6 Summary

Dissertation zur Erlangung des akademischen Grades:

Dr. rer. med.

Titel: Evaluation of PTPRZ1 and TMEM158 as potential new targets for a CAR-T-Cell-based approach for the treatment of glioblastoma

eingereicht von: Christoph Bach

angefertigt in: Klinik und Poliklinik für Neurochirurgie und dem Fraunhofer-Institut für Zelltherapie und Immunologie IZI

betreut von:

Prof. Dr. Frank Gaunitz

Dr. Jana Burkhardt

Prof. Dr. Jürgen Meixensberger

Einreichung: 11/2022

Glioblastoma (GBM) is the most frequent and lethal malignant brain tumor in adults². It emerges with an incidence of 3.2 per 100.000 in the US and 3.91 in Europe³. Today, standard treatment after diagnosis consists of surgical removal of tumor tissue, followed by radiation therapy and adjuvant chemotherapy using temozolomide⁶. Even after this rigorous therapy, patients show a median overall survival of only 15.6 months or 20.5 months when the tumor is additionally treated with so-called tumor treating fields²⁹. GBM is characterized by molecular heterogeneity within the same patient but also between different patients, which impedes development of novel therapeutics^{62,64}. During the last decades various immunotherapies including (multi-epitope) peptide vaccines, oncolytic viruses or immune checkpoint inhibitors against GBM were tested in small clinical studies, but failed to show a benefit in large studies. A novel kind of immunotherapies that showed great success in hematological tumors so far, is based on chimeric antigen receptors (CAR).

These synthetic receptors can be introduced into immune cells to retarget their function towards tumor cells, independently of the major histocompatibility complex (MHC)³⁹ that is often down regulated by tumors for immune evasion^{42,43}. A large hurdle for treatment of GBM using immunotherapies such as CAR-T cells, is antigen heterogeneity that limits the effect of therapies against single targets and renders the need for discovery of novel targets to enable treatment of a wide variety of patients with high success.

Analyzing publicly available data and performing RT-qPCR experiments with RNA isolated from GBM tissue of a local cohort of patients, overexpression of two candidate GBM antigens, namely *TMEM158* and *PTPRZ1* were observed. Overexpression of both antigens in GBM in comparison to normal brain tissue and low-grade gliomas (only *TMEM158*) was revealed. In addition, a negative correlation between expression and patient survival was detected, as well as a correlation between *TMEM158* and *CD44* expression, the latter being a marker for GBM stem cells and the mesenchymal GBM subtype¹⁵³. Induction of chemoresistance by *TMEM158* seems likely for GBM, since this was already discovered for several other tumor entities^{130,131}. Protein expression of *TMEM158* was confirmed by Western blot analysis of different GBM cell lines.

Since cell surface expression of a target protein is a prerequisite for targeting by a CAR-therapy, the expression of *TMEM158* on cells from GBM cell lines was analyzed by flow cytometry. For this analysis a fluorescence-labeled peptide, based on sequence information of a known naturally occurring *TMEM158* ligand (BINP) was designed. Binding to T98G and U-87 MG was observed, while only very low binding to the neuroblastoma cell line SH-SY5Y was seen in flow cytometry. Partial knockdown of *TMEM158* was achieved using DsiRNAs, followed by Western blot (antibody staining) and flow cytometry (peptide staining), confirming the specificity of binding detectable by both methods.

A recombinant fusion protein, consisting of the extracellular part of *TMEM158* and a human Fc-antibody fragment was produced in 293T cells by transient transfection of an expression vector. The expected size of the protein produced was confirmed by Western blot. Furthermore, binding of the BINP-peptide to the recombinant protein was analyzed and compared to a scrambled BINP-peptide. In these experiments specific binding of the BINP-peptide was observed, also indicating the functionality of the recombinant protein.

Next, CAR-constructs were designed using the original sequence information from BINP as binding domain and additional variants with amino acid exchanges at different positions. Significant cytotoxicity of all BINP-CAR-T cells was observed against T98G, which showed highest binding of BINP when analyzed by flow cytometry. A BINP-CAR version in which phenylalanine 11 was exchanged with alanine (BINP-F11A-CAR) showed significantly higher cytotoxicity against T98G than the BINP-CAR containing the original BINP sequence (BINP-WT-CAR). Against the U-87 MG cell line, only a version of the BINP-CAR containing an RGD- (arginine-glycine-aspartic acid) motif showed significant cytotoxicity. RGD-motifs are known to bind integrins like $\alpha V\beta 3$ ¹⁷³, which was abundantly present on this cell line, as it was confirmed by flow cytometry within this work. Using this BINP-RGD-CAR version, targeting of both antigens at the same time seems possible. No significant cytotoxicity of the different CAR versions was observed against the TMEM158^{low}- $\alpha V\beta 3$ - cell line SH-SY5Y.

In conclusion, overexpression of *TMEM158* and *PTPRZ1* and their negative influence on survival of patients, as found in recent literature, was confirmed for glioblastoma. Significantly higher expression of *TMEM158* in GBM in comparison to low-grade gliomas as well as the correlation with *CD44* hint at an association of *TMEM158* with the aggressive phenotype of GBM. For all of these reasons, targeting of *TMEM158* appears to be very feasible. Cytotoxicity of the produced BINP-CAR-T cells, which are the first CAR-T cells targeting *TMEM158* so far, was demonstrated against GBM cells. Additional to cytotoxicity of the CAR-T cells, other *in vitro* assays and *in vivo* models should be utilized to determine more aspects of CAR-T cell function, in the future. For example, proliferation, cytokine release, invasion of tumor tissue, and inactivation of CAR-T cells by the tumor milieu should be quantified. To estimate how many patients could benefit from a therapy against it, percentage of patients and distribution within the tumors should be determined.

7 References

- (1) Tokarew, N.; Ogonek, J.; Endres, S.; Bergwelt-Baildon, M. von; Kobold, S. Teaching an old dog new tricks: next-generation CAR T cells. *British journal of cancer* **2019**, *120* (1), 26–37. DOI: 10.1038/s41416-018-0325-1. Published Online: Nov. 9, 2018.
- (2) Ostrom, Q. T.; Patil, N.; Cioffi, G.; Waite, K.; Kruchko, C.; Barnholtz-Sloan, J. S. CBTRUS Statistical Report: Primary Brain and Other Central Nervous System Tumors Diagnosed in the United States in 2013-2017. *Neuro-oncology* **2020**, *22* (12 Suppl 2), iv1-iv96. DOI: 10.1093/neuonc/noaa200.
- (3) Sant, M.; Minicozzi, P.; Lagorio, S.; Børge Johannesen, T.; Marcos-Gragera, R.; Francisci, S. Survival of European patients with central nervous system tumors. *International journal of cancer* **2012**, *131* (1), 173–185. DOI: 10.1002/ijc.26335. Published Online: Nov. 10, 2011.
- (4) Davis, M. E. Glioblastoma: Overview of Disease and Treatment. *Clinical journal of oncology nursing* **2016**, *20* (5 Suppl), 8. DOI: 10.1188/16.CJON.S1.2-8.
- (5) Ellor, S. V.; Pagano-Young, T. A.; Avgeropoulos, N. G. Glioblastoma: background, standard treatment paradigms, and supportive care considerations. *The Journal of law, medicine & ethics : a journal of the American Society of Law, Medicine & Ethics* **2014**, *42* (2), 171–182. DOI: 10.1111/jlme.12133.
- (6) Stupp, R.; Brada, M.; van den Bent, M J; Tonn, J.-C.; Pentheroudakis, G. High-grade glioma: ESMO Clinical Practice Guidelines for diagnosis, treatment and follow-up. *Annals of oncology : official journal of the European Society for Medical Oncology* **2014**, *25* Suppl 3, 101. DOI: 10.1093/annonc/mdu050. Published Online: Apr. 29, 2014.
- (7) Alifieris, C.; Trafalis, D. T. Glioblastoma multiforme: Pathogenesis and treatment. *Pharmacology & therapeutics* **2015**, *152*, 63–82. DOI: 10.1016/j.pharmthera.2015.05.005. Published Online: May. 2, 2015.
- (8) Gulden-Sala, W.; Roth, P.; Brown, M.; Andratschke, N.; Weller, M.; Stupp, R. Gliome - was ich wissen muss in zehn Fragen. *Praxis* **2016**, *105* (6), 330–337. DOI: 10.1024/1661-8157/a002303.
- (9) Sizoo, E. M.; Braam, L.; Postma, T. J.; Pasman, H. R. W.; Heimans, J. J.; Klein, M.; Reijneveld, J. C.; Taphoorn, M. J. B. Symptoms and problems in the end-of-life phase of high-grade glioma patients. *Neuro-oncology* **2010**, *12* (11), 1162–1166. DOI: 10.1093/neuonc/nop045. Published Online: Jan. 27, 2010.
- (10) Barbaro, M.; Blinderman, C. D.; Iwamoto, F. M.; Kreisl, T. N.; Welch, M. R.; Odi, Y.; Donovan, L. E.; Joanta-Gomez, A. E.; Evans, K. A.; Lassman, A. B. Causes of Death and End-of-Life Care in Patients With Intracranial High-Grade Gliomas: A Retrospective Observational Study. *Neurology* **2022**, *98* (3), e260-e266. DOI: 10.1212/WNL.0000000000013057. Published Online: Nov. 18, 2021.
- (11) Louis, D. N.; Ohgaki, H.; Wiestler, O. D.; Cavenee, W. K.; Burger, P. C.; Jouvet, A.; Scheithauer, B. W.; Kleihues, P. The 2007 WHO classification of tumours of the central nervous system. *Acta neuropathologica* **2007**, *114* (2), 97–109. DOI: 10.1007/s00401-007-0243-4. Published Online: Jul. 6, 2007.
- (12) Han, S. J.; Yang, I.; Tihan, T.; Prados, M. D.; Parsa, A. T. Primary gliosarcoma: key clinical and pathologic distinctions from glioblastoma with implications as a unique oncologic entity. *Journal of neuro-oncology* **2010**, *96* (3), 313–320. DOI: 10.1007/s11060-009-9973-6. Published Online: Jul. 18, 2009.
- (13) Margetts, J. C.; Kalyan-Raman, U. P. Giant-celled glioblastoma of brain. A clinico-pathological and radiological study of ten cases (including immunohistochemistry and ultrastructure). *Cancer* **1989**, *63* (3), 524–531. DOI: 10.1002/1097-0142(19890201)63:3<524:aid-cnrcr2820630321>3.0.co;2-d.

- (14) Broniscer, A.; Tatevossian, R. G.; Sabin, N. D.; Klimo, P.; Dalton, J.; Lee, R.; Gajjar, A.; Ellison, D. W. Clinical, radiological, histological and molecular characteristics of paediatric epithelioid glioblastoma. *Neuropathology and applied neurobiology* **2014**, *40* (3), 327–336. DOI: 10.1111/nan.12093.
- (15) Ohgaki, H.; Kleihues, P. The definition of primary and secondary glioblastoma. *Clinical cancer research : an official journal of the American Association for Cancer Research* **2013**, *19* (4), 764–772. DOI: 10.1158/1078-0432.CCR-12-3002. Published Online: Dec. 3, 2012.
- (16) Hegi, M. E.; Diserens, A.-C.; Gorlia, T.; Hamou, M.-F.; Tribolet, N. de; Weller, M.; Kros, J. M.; Hainfellner, J. A.; Mason, W.; Mariani, L.; Bromberg, J. E. C.; Hau, P.; Mirimanoff, R. O.; Cairncross, J. G.; Janzer, R. C.; Stupp, R. MGMT gene silencing and benefit from temozolomide in glioblastoma. *The New England journal of medicine* **2005**, *352* (10), 997–1003. DOI: 10.1056/NEJMoa043331.
- (17) Brennan, C. W.; Verhaak, R. G. W.; McKenna, A.; Campos, B.; Nounshmehr, H.; Salama, S. R.; Zheng, S.; Chakravarty, D.; Sanborn, J. Z.; Berman, S. H.; Beroukhi, R.; Bernard, B.; Wu, C.-J.; Genovese, G.; Shmulevich, I.; Barnholtz-Sloan, J.; Zou, L.; Vegesna, R.; Shukla, S. A.; Ciriello, G.; Yung, W. K.; Zhang, W.; Sougnez, C.; Mikkelsen, T.; Aldape, K.; Bigner, D. D.; van Meir, E. G.; Prados, M.; Sloan, A.; Black, K. L.; Eschbacher, J.; Finocchiaro, G.; Friedman, W.; Andrews, D. W.; Guha, A.; Iacocca, M.; O'Neill, B. P.; Foltz, G.; Myers, J.; Weisenberger, D. J.; Penny, R.; Kucherlapati, R.; Perou, C. M.; Hayes, D. N.; Gibbs, R.; Marra, M.; Mills, G. B.; Lander, E.; Spellman, P.; Wilson, R.; Sander, C.; Weinstein, J.; Meyerson, M.; Gabriel, S.; Laird, P. W.; Haussler, D.; Getz, G.; Chin, L. The somatic genomic landscape of glioblastoma. *Cell* **2013**, *155* (2), 462–477. DOI: 10.1016/j.cell.2013.09.034.
- (18) Gotink, K. J.; Verheul, H. M. W. Anti-angiogenic tyrosine kinase inhibitors: what is their mechanism of action? *Angiogenesis* **2010**, *13* (1), 1–14. DOI: 10.1007/s10456-009-9160-6. Published Online: Dec. 11, 2009.
- (19) Pan, C.-M.; Chan, K.-H.; Chen, C.-H.; Jan, C.-I.; Liu, M.-C.; Lin, C.-M.; Cho, D.-Y.; Tsai, W.-C.; Chu, Y.-T.; Cheng, C.-H.; Chuang, H.-Y.; Chiu, S.-C. MicroRNA-7 targets T-Box 2 to inhibit epithelial-mesenchymal transition and invasiveness in glioblastoma multiforme. *Cancer letters* **2020**, *493*, 133–142. DOI: 10.1016/j.canlet.2020.08.024. Published Online: Aug. 27, 2020.
- (20) Li, H.; Li, J.; Zhang, G.; Da, Q.; Chen, L.; Yu, S.; Zhou, Q.; Weng, Z.; Xin, Z.; Shi, L.; Ma, L.; Huang, A.; Qi, S.; Lu, Y. HMGB1-Induced p62 Overexpression Promotes Snail-Mediated Epithelial-Mesenchymal Transition in Glioblastoma Cells via the Degradation of GSK-3 β . *Theranostics* **2019**, *9* (7), 1909–1922. DOI: 10.7150/thno.30578. Published Online: Mar. 16, 2019.
- (21) Li, H.; Chen, L.; Li, J.-J.; Zhou, Q.; Huang, A.; Liu, W.-W.; Wang, K.; Gao, L.; Qi, S.-T.; Lu, Y.-T. miR-519a enhances chemosensitivity and promotes autophagy in glioblastoma by targeting STAT3/Bcl2 signaling pathway. *Journal of hematology & oncology* **2018**, *11* (1), 70. DOI: 10.1186/s13045-018-0618-0. Published Online: May. 29, 2018.
- (22) Rodrigues, B. R.; Queiroz-Hazarbassanov, N.; Lopes, M. H.; Bleggi-Torres, L. F.; Suzuki, S.; Cunha, I. W.; Sanematsu, P.; Martins, V. R. Nuclear unphosphorylated STAT3 correlates with a worse prognosis in human glioblastoma. *Pathology, research and practice* **2016**, *212* (6), 517–523. DOI: 10.1016/j.prp.2016.03.001. Published Online: Mar. 14, 2016.
- (23) Verhaak, R. G. W.; Hoadley, K. A.; Purdom, E.; Wang, V.; Qi, Y.; Wilkerson, M. D.; Miller, C. R.; Ding, L.; Golub, T.; Mesirov, J. P.; Alexe, G.; Lawrence, M.; O'Kelly, M.; Tamayo, P.; Weir, B. A.; Gabriel, S.; Winckler, W.; Gupta, S.; Jakkula, L.; Feiler, H. S.; Hodgson, J. G.; James, C. D.; Sarkaria, J. N.; Brennan, C.; Kahn, A.; Spellman, P. T.; Wilson, R. K.; Speed, T. P.; Gray, J. W.; Meyerson, M.; Getz, G.; Perou, C. M.; Hayes, D. N. Integrated genomic analysis identifies clinically relevant subtypes of glioblastoma characterized by abnormalities

in PDGFRA, IDH1, EGFR, and NF1. *Cancer cell* **2010**, *17* (1), 98–110. DOI: 10.1016/j.ccr.2009.12.020.

(24) Gill, B. J.; Pisapia, D. J.; Malone, H. R.; Goldstein, H.; Lei, L.; Sonabend, A.; Yun, J.; Samanamud, J.; Sims, J. S.; Banu, M.; Dovas, A.; Teich, A. F.; Sheth, S. A.; McKhann, G. M.; Sisti, M. B.; Bruce, J. N.; Sims, P. A.; Canoll, P. MRI-localized biopsies reveal subtype-specific differences in molecular and cellular composition at the margins of glioblastoma. *Proceedings of the National Academy of Sciences of the United States of America* **2014**, *111* (34), 12550–12555. DOI: 10.1073/pnas.1405839111. Published Online: Aug. 11, 2014.

(25) Wang, Q.; Hu, B.; Hu, X.; Kim, H.; Squatrito, M.; Scarpace, L.; deCarvalho, A. C.; Lyu, S.; Li, P.; Li, Y.; Barthel, F.; Cho, H. J.; Lin, Y.-H.; Satani, N.; Martinez-Ledesma, E.; Zheng, S.; Chang, E.; Sauv e, C.-E. G.; Olar, A.; Lan, Z. D.; Finocchiaro, G.; Phillips, J. J.; Berger, M. S.; Gabrusiewicz, K. R.; Wang, G.; Eskilsson, E.; Hu, J.; Mikkelsen, T.; DePinho, R. A.; Muller, F.; Heimberger, A. B.; Sulman, E. P.; Nam, D.-H.; Verhaak, R. G. W. Tumor Evolution of Glioma-Intrinsic Gene Expression Subtypes Associates with Immunological Changes in the Microenvironment. *Cancer cell* **2017**, *32* (1), 42. DOI: 10.1016/j.ccell.2017.06.003.

(26) Zhang, P.; Xia, Q.; Liu, L.; Li, S.; Dong, L. Current Opinion on Molecular Characterization for GBM Classification in Guiding Clinical Diagnosis, Prognosis, and Therapy. *Frontiers in molecular biosciences* **2020**, *7*, 562798. DOI: 10.3389/fmolb.2020.562798. Published Online: Sep. 8, 2020.

(27) Galldiks, N.; Stoffels, G.; Ruge, M. I.; Rapp, M.; Sabel, M.; Reifenberger, G.; Erdem, Z.; Shah, N. J.; Fink, G. R.; Coenen, H. H.; Langen, K.-J. Role of O-(2-18F-fluoroethyl)-L-tyrosine PET as a diagnostic tool for detection of malignant progression in patients with low-grade glioma. *Journal of nuclear medicine : official publication, Society of Nuclear Medicine* **2013**, *54* (12), 2046–2054. DOI: 10.2967/jnumed.113.123836. Published Online: Oct. 24, 2013.

(28) Galldiks, N.; Langen, K.-J. Anwendung der Aminos ure-PET in der Diagnostik und Therapie von zerebralen Gliomen. *Fortschritte der Neurologie-Psychiatrie* **2012**, *80* (1), 17–23. DOI: 10.1055/s-0031-1281851. Published Online: Dec. 12, 2011.

(29) Stupp, R.; Taillibert, S.; Kanner, A. A.; Kesari, S.; Steinberg, D. M.; Toms, S. A.; Taylor, L. P.; Lieberman, F.; Silvani, A.; Fink, K. L.; Barnett, G. H.; Zhu, J.-J.; Henson, J. W.; Engelhard, H. H.; Chen, T. C.; Tran, D. D.; Sroubek, J.; Tran, N. D.; Hottinger, A. F.; Landolfi, J.; Desai, R.; Caroli, M.; Kew, Y.; Honnorat, J.; Idbaih, A.; Kirson, E. D.; Weinberg, U.; Palti, Y.; Hegi, M. E.; Ram, Z. Maintenance Therapy With Tumor-Treating Fields Plus Temozolomide vs Temozolomide Alone for Glioblastoma: A Randomized Clinical Trial. *JAMA* **2015**, *314* (23), 2535–2543. DOI: 10.1001/jama.2015.16669.

(30) Medikonda, R.; Dunn, G.; Rahman, M.; Fecci, P.; Lim, M. A review of glioblastoma immunotherapy. *Journal of neuro-oncology* **2021**, *151* (1), 41–53. DOI: 10.1093/neuros/nyx321. Published Online: Apr. 6, 2020.

(31) Weller, M.; Butowski, N.; Tran, D. D.; Recht, L. D.; Lim, M.; Hirte, H.; Ashby, L.; Mechtler, L.; Goldlust, S. A.; Iwamoto, F.; Drappatz, J.; O'Rourke, D. M.; Wong, M.; Hamilton, M. G.; Finocchiaro, G.; Perry, J.; Wick, W.; Green, J.; He, Y.; Turner, C. D.; Yellin, M. J.; Keler, T.; Davis, T. A.; Stupp, R.; Sampson, J. H. Rindopepimut with temozolomide for patients with newly diagnosed, EGFRvIII-expressing glioblastoma (ACT IV): a randomised, double-blind, international phase 3 trial. *The Lancet. Oncology* **2017**, *18* (10), 1373–1385. DOI: 10.1016/S1470-2045(17)30517-X. Published Online: Aug. 23, 2017.

(32) Banchereau, J.; Steinman, R. M. Dendritic cells and the control of immunity. *Nature* **1998**, *392* (6673), 245–252. DOI: 10.1038/32588.

(33) Cintolo, J. A.; Datta, J.; Mathew, S. J.; Czerniecki, B. J. Dendritic cell-based vaccines: barriers and opportunities. *Future oncology (London, England)* **2012**, *8* (10), 1273–1299. DOI: 10.2217/fon.12.125.

- (34) Filley, A. C.; Dey, M. Dendritic cell based vaccination strategy: an evolving paradigm. *Journal of neuro-oncology* **2017**, *133* (2), 223–235. DOI: 10.1007/s11060-017-2446-4. Published Online: Apr. 22, 2017.
- (35) Liau, L. M.; Ashkan, K.; Tran, D. D.; Campian, J. L.; Trusheim, J. E.; Cobbs, C. S.; Heth, J. A.; Salacz, M.; Taylor, S.; D'Andre, S. D.; Iwamoto, F. M.; Dropcho, E. J.; Moshel, Y. A.; Walter, K. A.; Pillainayagam, C. P.; Aiken, R.; Chaudhary, R.; Goldlust, S. A.; Bota, D. A.; Duic, P.; Grewal, J.; Elinzano, H.; Toms, S. A.; Lillehei, K. O.; Mikkelsen, T.; Walbert, T.; Abram, S. R.; Brenner, A. J.; Brem, S.; Ewend, M. G.; Khagi, S.; Portnow, J.; Kim, L. J.; Loudon, W. G.; Thompson, R. C.; Avigan, D. E.; Fink, K. L.; Geoffroy, F. J.; Lindhorst, S.; Lutzky, J.; Sloan, A. E.; Schackert, G.; Krex, D.; Meisel, H.-J.; Wu, J.; Davis, R. P.; Duma, C.; Etame, A. B.; Mathieu, D.; Kesari, S.; Piccioni, D.; Westphal, M.; Baskin, D. S.; New, P. Z.; Lacroix, M.; May, S.-A.; Pluard, T. J.; Tse, V.; Green, R. M.; Villano, J. L.; Pearlman, M.; Petrecca, K.; Schulder, M.; Taylor, L. P.; Maida, A. E.; Prins, R. M.; Cloughesy, T. F.; Mulholland, P.; Bosch, M. L. First results on survival from a large Phase 3 clinical trial of an autologous dendritic cell vaccine in newly diagnosed glioblastoma. *Journal of translational medicine* **2018**, *16* (1), 142. DOI: 10.1186/s12967-018-1507-6. Published Online: May. 29, 2018.
- (36) Melcher, A.; Parato, K.; Rooney, C. M.; Bell, J. C. Thunder and lightning: immunotherapy and oncolytic viruses collide. *Molecular therapy : the journal of the American Society of Gene Therapy* **2011**, *19* (6), 1008–1016. DOI: 10.1038/mt.2011.65. Published Online: Apr. 19, 2011.
- (37) Lang, F. F.; Conrad, C.; Gomez-Manzano, C.; Yung, W. K. A.; Sawaya, R.; Weinberg, J. S.; Prabhu, S. S.; Rao, G.; Fuller, G. N.; Aldape, K. D.; Gumin, J.; Vence, L. M.; Wistuba, I.; Rodriguez-Canales, J.; Villalobos, P. A.; Dirven, C. M. F.; Tejada, S.; Valle, R. D.; Alonso, M. M.; Ewald, B.; Peterkin, J. J.; Tufaro, F.; Fueyo, J. Phase I Study of DNX-2401 (Delta-24-RGD) Oncolytic Adenovirus: Replication and Immunotherapeutic Effects in Recurrent Malignant Glioma. *Journal of clinical oncology : official journal of the American Society of Clinical Oncology* **2018**, *36* (14), 1419–1427. DOI: 10.1200/JCO.2017.75.8219. Published Online: Feb. 12, 2018.
- (38) Omuro, A.; Vlahovic, G.; Lim, M.; Sahebjam, S.; Baehring, J.; Cloughesy, T.; Voloschin, A.; Ramkissoon, S. H.; Ligon, K. L.; Latek, R.; Zvirtes, R.; Strauss, L.; Paliwal, P.; Harbison, C. T.; Reardon, D. A.; Sampson, J. H. Nivolumab with or without ipilimumab in patients with recurrent glioblastoma: results from exploratory phase I cohorts of CheckMate 143. *Neuro-oncology* **2018**, *20* (5), 674–686. DOI: 10.1093/neuonc/nox208.
- (39) Eshhar, Z.; Waks, T.; Gross, G.; Schindler, D. G. Specific activation and targeting of cytotoxic lymphocytes through chimeric single chains consisting of antibody-binding domains and the gamma or zeta subunits of the immunoglobulin and T-cell receptors. *Proceedings of the National Academy of Sciences of the United States of America* **1993**, *90* (2), 720–724. DOI: 10.1073/pnas.90.2.720.
- (40) Huston, J. S.; Levinson, D.; Mudgett-Hunter, M.; Tai, M. S.; Novotný, J.; Margolies, M. N.; Ridge, R. J.; Brucoleri, R. E.; Haber, E.; Crea, R. Protein engineering of antibody binding sites: recovery of specific activity in an anti-digoxin single-chain Fv analogue produced in *Escherichia coli*. *Proceedings of the National Academy of Sciences of the United States of America* **1988**, *85* (16), 5879–5883. DOI: 10.1073/pnas.85.16.5879.
- (41) Brocker, T.; Peter, A.; Traunecker, A.; Karjalainen, K. New simplified molecular design for functional T cell receptor. *European journal of immunology* **1993**, *23* (7), 1435–1439. DOI: 10.1002/eji.1830230705.
- (42) Cornel, A. M.; Mimpfen, I. L.; Nierkens, S. MHC Class I Downregulation in Cancer: Underlying Mechanisms and Potential Targets for Cancer Immunotherapy. *Cancers* **2020**, *12* (7). DOI: 10.3390/cancers12071760. Published Online: Jul. 2, 2020.

- (43) Moritz, D.; Wels, W.; Mattern, J.; Groner, B. Cytotoxic T lymphocytes with a grafted recognition specificity for ERBB2-expressing tumor cells. *Proceedings of the National Academy of Sciences of the United States of America* **1994**, *91* (10), 4318–4322. DOI: 10.1073/pnas.91.10.4318.
- (44) Gyobu, H.; Tsuji, T.; Suzuki, Y.; Ohkuri, T.; Chamoto, K.; Kuroki, M.; Miyoshi, H.; Kawarada, Y.; Katoh, H.; Takeshima, T.; Nishimura, T. Generation and targeting of human tumor-specific Tc1 and Th1 cells transduced with a lentivirus containing a chimeric immunoglobulin T-cell receptor. *Cancer research* **2004**, *64* (4), 1490–1495. DOI: 10.1158/0008-5472.can-03-2780.
- (45) Imai, C.; Mihara, K.; Andreansky, M.; Nicholson, I. C.; Pui, C.-H.; Geiger, T. L.; Campana, D. Chimeric receptors with 4-1BB signaling capacity provoke potent cytotoxicity against acute lymphoblastic leukemia. *Leukemia* **2004**, *18* (4), 676–684. DOI: 10.1038/sj.leu.2403302.
- (46) Kawalekar, O. U.; O'Connor, R. S.; Fraietta, J. A.; Guo, L.; McGettigan, S. E.; Posey, A. D.; Patel, P. R.; Guedan, S.; Scholler, J.; Keith, B.; Snyder, N. W.; Snyder, N.; Blair, I. A.; Blair, I.; Milone, M. C.; June, C. H. Distinct Signaling of Coreceptors Regulates Specific Metabolism Pathways and Impacts Memory Development in CAR T Cells. *Immunity* **2016**, *44* (2), 380–390. DOI: 10.1016/j.immuni.2016.01.021.
- (47) Carpenito, C.; Milone, M. C.; Hassan, R.; Simonet, J. C.; Lakhali, M.; Suhoski, M. M.; Varela-Rohena, A.; Haines, K. M.; Heitjan, D. F.; Albelda, S. M.; Carroll, R. G.; Riley, J. L.; Pastan, I.; June, C. H. Control of large, established tumor xenografts with genetically retargeted human T cells containing CD28 and CD137 domains. *Proceedings of the National Academy of Sciences of the United States of America* **2009**, *106* (9), 3360–3365. DOI: 10.1073/pnas.0813101106. Published Online: Feb. 11, 2009.
- (48) Hombach, A. A.; Abken, H. Costimulation by chimeric antigen receptors revisited the T cell antitumor response benefits from combined CD28-OX40 signalling. *International journal of cancer* **2011**, *129* (12), 2935–2944. DOI: 10.1002/ijc.25960. Published Online: Mar. 29, 2011.
- (49) Chmielewski, M.; Kopecky, C.; Hombach, A. A.; Abken, H. IL-12 release by engineered T cells expressing chimeric antigen receptors can effectively Muster an antigen-independent macrophage response on tumor cells that have shut down tumor antigen expression. *Cancer research* **2011**, *71* (17), 5697–5706. DOI: 10.1158/0008-5472.CAN-11-0103. Published Online: Jul. 8, 2011.
- (50) Kagoya, Y.; Tanaka, S.; Guo, T.; Anczurowski, M.; Wang, C.-H.; Saso, K.; Butler, M. O.; Minden, M. D.; Hirano, N. A novel chimeric antigen receptor containing a JAK-STAT signaling domain mediates superior antitumor effects. *Nature medicine* **2018**, *24* (3), 352–359. DOI: 10.1038/nm.4478. Published Online: Feb. 5, 2018.
- (51) Park, S.; Shevlin, E.; Vedvyas, Y.; Zaman, M.; Park, S.; Hsu, Y.-M. S.; Min, I. M.; Jin, M. M. Micromolar affinity CAR T cells to ICAM-1 achieves rapid tumor elimination while avoiding systemic toxicity. *Scientific reports* **2017**, *7* (1), 14366. DOI: 10.1038/s41598-017-14749-3. Published Online: Oct. 30, 2017.
- (52) Caruso, H. G.; Hurton, L. V.; Najjar, A.; Rushworth, D.; Ang, S.; Olivares, S.; Mi, T.; Switzer, K.; Singh, H.; Huls, H.; Lee, D. A.; Heimberger, A. B.; Champlin, R. E.; Cooper, L. J. N. Tuning Sensitivity of CAR to EGFR Density Limits Recognition of Normal Tissue While Maintaining Potent Antitumor Activity. *Cancer research* **2015**, *75* (17), 3505–3518. DOI: 10.1158/0008-5472.CAN-15-0139.
- (53) Liu, X.; Jiang, S.; Fang, C.; Yang, S.; Olalere, D.; Pequignot, E. C.; Cogdill, A. P.; Li, N.; Ramones, M.; Granda, B.; Zhou, L.; Loew, A.; Young, R. M.; June, C. H.; Zhao, Y. Affinity-Tuned ErbB2 or EGFR Chimeric Antigen Receptor T Cells Exhibit an Increased Therapeutic Index against Tumors in Mice. *Cancer research* **2015**, *75* (17), 3596–3607. DOI: 10.1158/0008-5472.CAN-15-0159.

- (54) Hartmann, J.; Schüßler-Lenz, M.; Bondanza, A.; Buchholz, C. J. Clinical development of CAR T cells-challenges and opportunities in translating innovative treatment concepts. *EMBO molecular medicine* **2017**, *9* (9), 1183–1197. DOI: 10.15252/emmm.201607485.
- (55) Zeng, J.; Zhang, J.; Yang, Y.-Z.; Wang, F.; Jiang, H.; Chen, H.-D.; Wu, H.-Y.; Sai, K.; Hu, W.-M. IL13RA2 is overexpressed in malignant gliomas and related to clinical outcome of patients. *American journal of translational research* **2020**, *12* (8), 4702–4714. DOI: None. Published Online: Aug. 15, 2020.
- (56) Brown, C. E.; Badie, B.; Barish, M. E.; Weng, L.; Ostberg, J. R.; Chang, W.-C.; Naranjo, A.; Starr, R.; Wagner, J.; Wright, C.; Zhai, Y.; Bading, J. R.; Ressler, J. A.; Portnow, J.; D'Apuzzo, M.; Forman, S. J.; Jensen, M. C. Bioactivity and Safety of IL13R α 2-Redirected Chimeric Antigen Receptor CD8+ T Cells in Patients with Recurrent Glioblastoma. *Clinical cancer research : an official journal of the American Association for Cancer Research* **2015**, *21* (18), 4062–4072. DOI: 10.1158/1078-0432.CCR-15-0428. Published Online: Jun. 9, 2015.
- (57) Brown, C. E.; Alizadeh, D.; Starr, R.; Weng, L.; Wagner, J. R.; Naranjo, A.; Ostberg, J. R.; Blanchard, M. S.; Kilpatrick, J.; Simpson, J.; Kurien, A.; Priceman, S. J.; Wang, X.; Harshbarger, T. L.; D'Apuzzo, M.; Ressler, J. A.; Jensen, M. C.; Barish, M. E.; Chen, M.; Portnow, J.; Forman, S. J.; Badie, B. Regression of Glioblastoma after Chimeric Antigen Receptor T-Cell Therapy. *The New England journal of medicine* **2016**, *375* (26), 2561–2569. DOI: 10.1056/NEJMoa1610497.
- (58) Ahmed, N.; Brawley, V.; Hegde, M.; Bielałowicz, K.; Kalra, M.; Landi, D.; Robertson, C.; Gray, T. L.; Diouf, O.; Wakefield, A.; Ghazi, A.; Gerken, C.; Yi, Z.; Ashoori, A.; Wu, M.-F.; Liu, H.; Rooney, C.; Dotti, G.; Gee, A.; Su, J.; Kew, Y.; Baskin, D.; Zhang, Y. J.; New, P.; Grilley, B.; Stojakovic, M.; Hicks, J.; Powell, S. Z.; Brenner, M. K.; Heslop, H. E.; Grossman, R.; Wels, W. S.; Gottschalk, S. HER2-Specific Chimeric Antigen Receptor-Modified Virus-Specific T Cells for Progressive Glioblastoma: A Phase 1 Dose-Escalation Trial. *JAMA oncology* **2017**, *3* (8), 1094–1101. DOI: 10.1001/jamaoncol.2017.0184.
- (59) Nishikawa, R.; Sugiyama, T.; Narita, Y.; Furnari, F.; Cavenee, W. K.; Matsutani, M. Immunohistochemical analysis of the mutant epidermal growth factor, deltaEGFR, in glioblastoma. *Brain tumor pathology* **2004**, *21* (2), 53–56. DOI: 10.1007/BF02484510.
- (60) O'Rourke, D. M.; Nasrallah, M. P.; Desai, A.; Melenhorst, J. J.; Mansfield, K.; Morrisette, J. J. D.; Martinez-Lage, M.; Brem, S.; Maloney, E.; Shen, A.; Isaacs, R.; Mohan, S.; Plesa, G.; Lacey, S. F.; Navenot, J.-M.; Zheng, Z.; Levine, B. L.; Okada, H.; June, C. H.; Brogdon, J. L.; Maus, M. V. A single dose of peripherally infused EGFRvIII-directed CAR T cells mediates antigen loss and induces adaptive resistance in patients with recurrent glioblastoma. *Science translational medicine* **2017**, *9* (399). DOI: 10.1126/scitranslmed.aaa0984.
- (61) Lin, Q.; Ba, T.; Ho, J.; Chen, D.; Cheng, Y.; Wang, L.; Xu, G.; Xu, L.; Zhou, Y.; Wei, Y.; Li, J.; Ling, F. First-in-Human Trial of EphA2-Redirected CAR T-Cells in Patients With Recurrent Glioblastoma: A Preliminary Report of Three Cases at the Starting Dose. *Frontiers in oncology* **2021**, *11*, 694941. DOI: 10.3389/fonc.2021.694941. Published Online: Jun. 21, 2021.
- (62) Akhavan, D.; Alizadeh, D.; Wang, D.; Weist, M. R.; Shepphird, J. K.; Brown, C. E. CAR T cells for brain tumors: Lessons learned and road ahead. *Immunological reviews* **2019**, *290* (1), 60–84. DOI: 10.1111/imr.12773.
- (63) Zhang, B.-L.; Qin, D.-Y.; Mo, Z.-M.; Li, Y.; Wei, W.; Wang, Y.-S.; Wang, W.; Wei, Y.-Q. Hurdles of CAR-T cell-based cancer immunotherapy directed against solid tumors. *Science China. Life sciences* **2016**, *59* (4), 340–348. DOI: 10.1007/s11427-016-5027-4. Published Online: Mar. 11, 2016.

- (64) Inda, M.-D.-M.; Bonavia, R.; Seoane, J. Glioblastoma multiforme: a look inside its heterogeneous nature. *Cancers* **2014**, *6* (1), 226–239. DOI: 10.3390/cancers6010226. Published Online: Jan. 27, 2014.
- (65) Bielamowicz, K.; Fousek, K.; Byrd, T. T.; Samaha, H.; Mukherjee, M.; Aware, N.; Wu, M.-F.; Orange, J. S.; Sumazin, P.; Man, T.-K.; Joseph, S. K.; Hegde, M.; Ahmed, N. Trivalent CAR T cells overcome interpatient antigenic variability in glioblastoma. *Neuro-oncology* **2018**, *20* (4), 506–518. DOI: 10.1093/neuonc/nox182.
- (66) Caruso, H.; Heimberger, A. B. Comment on "Trivalent CAR T cells overcome interpatient antigenic variability in glioblastoma". *Neuro-oncology* **2018**, *20* (7), 1003–1004. DOI: 10.1093/neuonc/noy045.
- (67) Tang, X.; Zhao, S.; Zhang, Y.; Wang, Y.; Zhang, Z.; Yang, M.; Zhu, Y.; Zhang, G.; Guo, G.; Tong, A.; Zhou, L. B7-H3 as a Novel CAR-T Therapeutic Target for Glioblastoma. *Molecular therapy oncolytics* **2019**, *14*, 279–287. DOI: 10.1016/j.omto.2019.07.002. Published Online: Jul. 23, 2019.
- (68) Nehama, D.; Di Ianni, N.; Musio, S.; Du, H.; Patané, M.; Pollo, B.; Finocchiaro, G.; Park, J. J. H.; Dunn, D. E.; Edwards, D. S.; Damrauer, J. S.; Hudson, H.; Floyd, S. R.; Ferrone, S.; Savoldo, B.; Pellegatta, S.; Dotti, G. B7-H3-redirected chimeric antigen receptor T cells target glioblastoma and neurospheres. *EBioMedicine* **2019**, *47*, 33–43. DOI: 10.1016/j.ebiom.2019.08.030. Published Online: Aug. 26, 2019.
- (69) Cui, J.; Zhang, Q.; Song, Q.; Wang, H.; Dmitriev, P.; Sun, M. Y.; Cao, X.; Wang, Y.; Guo, L.; Indig, I. H.; Rosenblum, J. S.; Ji, C.; Cao, D.; Yang, K.; Gilbert, M. R.; Yao, Y.; Zhuang, Z. Targeting hypoxia downstream signaling protein, CAIX, for CAR T-cell therapy against glioblastoma. *Neuro-oncology* **2019**, *21* (11), 1436–1446. DOI: 10.1093/neuonc/noz117.
- (70) Wykosky, J.; Gibo, D. M.; Stanton, C.; Debinski, W. Interleukin-13 receptor alpha 2, EphA2, and Fos-related antigen 1 as molecular denominators of high-grade astrocytomas and specific targets for combinatorial therapy. *Clinical cancer research : an official journal of the American Association for Cancer Research* **2008**, *14* (1), 199–208. DOI: 10.1158/1078-0432.CCR-07-1990.
- (71) Chow, K. K. H.; Naik, S.; Kakarla, S.; Brawley, V. S.; Shaffer, D. R.; Yi, Z.; Rainusso, N.; Wu, M.-F.; Liu, H.; Kew, Y.; Grossman, R. G.; Powell, S.; Lee, D.; Ahmed, N.; Gottschalk, S. T cells redirected to EphA2 for the immunotherapy of glioblastoma. *Molecular therapy : the journal of the American Society of Gene Therapy* **2013**, *21* (3), 629–637. DOI: 10.1038/mt.2012.210. Published Online: Oct. 16, 2012.
- (72) Pellegatta, S.; Savoldo, B.; Di Ianni, N.; Corbetta, C.; Chen, Y.; Patané, M.; Sun, C.; Pollo, B.; Ferrone, S.; DiMeco, F.; Finocchiaro, G.; Dotti, G. Constitutive and TNF α -inducible expression of chondroitin sulfate proteoglycan 4 in glioblastoma and neurospheres: Implications for CAR-T cell therapy. *Science translational medicine* **2018**, *10* (430). DOI: 10.1126/scitranslmed.aao2731.
- (73) Metellus, P.; Nanni-Metellus, I.; Delfino, C.; Colin, C.; Tchogandjian, A.; Coulibaly, B.; Fina, F.; Loundou, A.; Barrie, M.; Chinot, O.; Ouafik, L.; Figarella-Branger, D. Prognostic impact of CD133 mRNA expression in 48 glioblastoma patients treated with concomitant radiochemotherapy: a prospective patient cohort at a single institution. *Annals of surgical oncology* **2011**, *18* (10), 2937–2945. DOI: 10.1245/s10434-011-1703-6. Published Online: Apr. 9, 2011.
- (74) Zhu, X.; Prasad, S.; Gaedicke, S.; Hettich, M.; Firat, E.; Niedermann, G. Patient-derived glioblastoma stem cells are killed by CD133-specific CAR T cells but induce the T cell aging marker CD57. *Oncotarget* **2015**, *6* (1), 171–184. DOI: 10.18632/oncotarget.2767.

- (75) Wallstabe, L.; Mades, A.; Frenz, S.; Einsele, H.; Rader, C.; Hudecek, M. CAR T cells targeting $\alpha\text{v}\beta 3$ integrin are effective against advanced cancer in preclinical models. *Advances in cell and gene therapy* **2018**, *1* (2). DOI: 10.1002/acg2.11. Published Online: Jul. 10, 2018.
- (76) Gingras, M. C.; Roussel, E.; Bruner, J. M.; Branch, C. D.; Moser, R. P. Comparison of cell adhesion molecule expression between glioblastoma multiforme and autologous normal brain tissue. *Journal of neuroimmunology* **1995**, *57* (1-2), 143–153. DOI: 10.1016/0165-5728(94)00178-q.
- (77) Wang, D.; Starr, R.; Chang, W.-C.; Aguilar, B.; Alizadeh, D.; Wright, S. L.; Yang, X.; Brito, A.; Sarkissian, A.; Ostberg, J. R.; Li, L.; Shi, Y.; Gutova, M.; Aboody, K.; Badie, B.; Forman, S. J.; Barish, M. E.; Brown, C. E. Chlorotoxin-directed CAR T cells for specific and effective targeting of glioblastoma. *Science translational medicine* **2020**, *12* (533). DOI: 10.1126/scitranslmed.aaw2672.
- (78) Sharma, G.; Braga, C. B.; Chen, K.-E.; Jia, X.; Ramanujam, V.; Collins, B. M.; Rittner, R.; Mobli, M. Structural basis for the binding of the cancer targeting scorpion toxin, CITx, to the vascular endothelia growth factor receptor neuropilin-1. *Current research in structural biology* **2021**, *3*, 179–186. DOI: 10.1016/j.crstbi.2021.07.003. Published Online: Aug. 2, 2021.
- (79) Chow, J. P. H.; Fujikawa, A.; Shimizu, H.; Suzuki, R.; Noda, M. Metalloproteinase- and gamma-secretase-mediated cleavage of protein-tyrosine phosphatase receptor type Z. *The Journal of biological chemistry* **2008**, *283* (45), 30879–30889. DOI: 10.1074/jbc.M802976200. Published Online: Aug. 18, 2008.
- (80) Maeda, N.; Ichihara-Tanaka, K.; Kimura, T.; Kadomatsu, K.; Muramatsu, T.; Noda, M. A receptor-like protein-tyrosine phosphatase PTPzeta/RPTPbeta binds a heparin-binding growth factor midkine. Involvement of arginine 78 of midkine in the high affinity binding to PTPzeta. *The Journal of biological chemistry* **1999**, *274* (18), 12474–12479. DOI: 10.1074/jbc.274.18.12474.
- (81) Müller, S.; Lamszus, K.; Nikolich, K.; Westphal, M. Receptor protein tyrosine phosphatase zeta as a therapeutic target for glioblastoma therapy. *Expert opinion on therapeutic targets* **2004**, *8* (3), 211–220. DOI: 10.1517/14728222.8.3.211.
- (82) Fujikawa, A.; Chow, J. P. H.; Matsumoto, M.; Suzuki, R.; Kuboyama, K.; Yamamoto, N.; Noda, M. Identification of novel splicing variants of protein tyrosine phosphatase receptor type Z. *Journal of biochemistry* **2017**, *162* (5), 381–390. DOI: 10.1093/jb/mvx042.
- (83) Garwood, J.; Heck, N.; Reichardt, F.; Faissner, A. Phosphacan short isoform, a novel non-proteoglycan variant of phosphacan/receptor protein tyrosine phosphatase-beta, interacts with neuronal receptors and promotes neurite outgrowth. *The Journal of biological chemistry* **2003**, *278* (26), 24164–24173. DOI: 10.1074/jbc.M211721200. Published Online: Apr. 16, 2003.
- (84) Nishiwaki, T.; Maeda, N.; Noda, M. Characterization and developmental regulation of proteoglycan-type protein tyrosine phosphatase zeta/RPTPbeta isoforms. *Journal of biochemistry* **1998**, *123* (3), 458–467. DOI: 10.1093/oxfordjournals.jbchem.a021959.
- (85) Canoll, P. D.; Barnea, G.; Levy, J. B.; Sap, J.; Ehrlich, M.; Silvennoinen, O.; Schlessinger, J.; Musacchio, J. M. The expression of a novel receptor-type tyrosine phosphatase suggests a role in morphogenesis and plasticity of the nervous system. *Brain research. Developmental brain research* **1993**, *75* (2), 293–298. DOI: 10.1016/0165-3806(93)90035-9.
- (86) Maeda, N.; Nishiwaki, T.; Shintani, T.; Hamanaka, H.; Noda, M. 6B4 proteoglycan/phosphacan, an extracellular variant of receptor-like protein-tyrosine phosphatase zeta/RPTPbeta, binds pleiotrophin/heparin-binding growth-associated molecule (HB-GAM). *The Journal of biological chemistry* **1996**, *271* (35), 21446–21452. DOI: 10.1074/jbc.271.35.21446.

- (87) Müller, S.; Kunkel, P.; Lamszus, K.; Ulbricht, U.; Lorente, G. A.; Nelson, A. M.; Schack, D. von; Chin, D. J.; Lohr, S. C.; Westphal, M.; Melcher, T. A role for receptor tyrosine phosphatase zeta in glioma cell migration. *Oncogene* **2003**, *22* (43), 6661–6668. DOI: 10.1038/sj.onc.1206763.
- (88) Dutoit, V.; Herold-Mende, C.; Hilf, N.; Schoor, O.; Beckhove, P.; Bucher, J.; Dorsch, K.; Flohr, S.; Fritsche, J.; Lewandrowski, P.; Lohr, J.; Rammensee, H.-G.; Stevanovic, S.; Trautwein, C.; Vass, V.; Walter, S.; Walker, P. R.; Weinschenk, T.; Singh-Jasuja, H.; Dietrich, P.-Y. Exploiting the glioblastoma peptidome to discover novel tumour-associated antigens for immunotherapy. *Brain : a journal of neurology* **2012**, *135* (Pt 4), 1042–1054. DOI: 10.1093/brain/aws042. Published Online: Mar. 14, 2012.
- (89) Lorente, G.; Nelson, A.; Mueller, S.; Kuo, J.; Urfer, R.; Nikolich, K.; Foehr, E. D. Functional comparison of long and short splice forms of RPTPbeta: implications for glioblastoma treatment. *Neuro-oncology* **2005**, *7* (2), 154–163. DOI: 10.1215/S1152851704000547.
- (90) Shi, Y.; Ping, Y.-F.; Zhou, W.; He, Z.-C.; Chen, C.; Bian, B.-S.-J.; Zhang, L.; Chen, L.; Lan, X.; Zhang, X.-C.; Zhou, K.; Liu, Q.; Long, H.; Fu, T.-W.; Zhang, X.-N.; Cao, M.-F.; Huang, Z.; Fang, X.; Wang, X.; Feng, H.; Yao, X.-H.; Yu, S.-C.; Cui, Y.-H.; Zhang, X.; Rich, J. N.; Bao, S.; Bian, X.-W. Tumour-associated macrophages secrete pleiotrophin to promote PTPRZ1 signalling in glioblastoma stem cells for tumour growth. *Nature communications* **2017**, *8*, 15080. DOI: 10.1038/ncomms15080. Published Online: Jun. 1, 2017.
- (91) Xia, Z.; Ouyang, D.; Li, Q.; Li, M.; Zou, Q.; Li, L.; Yi, W.; Zhou, E. The Expression, Functions, Interactions and Prognostic Values of PTPRZ1: A Review and Bioinformatic Analysis. *Journal of Cancer* **2019**, *10* (7), 1663–1674. DOI: 10.7150/jca.28231. Published Online: Apr. 2, 2019.
- (92) Huang, P.; Ouyang, D.-J.; Chang, S.; Li, M.-Y.; Li, L.; Li, Q.-Y.; Zeng, R.; Zou, Q.-Y.; Su, J.; Zhao, P.; Pei, L.; Yi, W.-J. Chemotherapy-driven increases in the CDKN1A/PTN/PTPRZ1 axis promote chemoresistance by activating the NF- κ B pathway in breast cancer cells. *Cell communication and signaling : CCS* **2018**, *16* (1), 92. DOI: 10.1186/s12964-018-0304-4. Published Online: Nov. 29, 2018.
- (93) Liu, S.; Song, A.; Zhou, X.; Huo, Z.; Yao, S.; Yang, B.; Liu, Y.; Wang, Y. ceRNA network development and tumour-infiltrating immune cell analysis of metastatic breast cancer to bone. *Journal of bone oncology* **2020**, *24*, 100304. DOI: 10.1016/j.jbo.2020.100304. Published Online: Jul. 20, 2020.
- (94) Wei, X.; Yang, S.; Pu, X.; He, S.; Yang, Z.; Sheng, X.; Meng, X.; Chen, X.; Jin, L.; Chen, W.; Zhang, Y. Tumor-associated macrophages increase the proportion of cancer stem cells in lymphoma by secreting pleiotrophin. *American journal of translational research* **2019**, *11* (10), 6393–6402. Published Online: Oct. 15, 2019.
- (95) Sethi, G.; Kwon, Y.; Burkhalter, R. J.; Pathak, H. B.; Madan, R.; McHugh, S.; Atay, S.; Murthy, S.; Tawfik, O. W.; Godwin, A. K. PTN signaling: Components and mechanistic insights in human ovarian cancer. *Molecular carcinogenesis* **2015**, *54* (12), 1772–1785. DOI: 10.1002/mc.22249. Published Online: Nov. 21, 2014.
- (96) Makinoshima, H.; Ishii, G.; Kojima, M.; Fujii, S.; Higuchi, Y.; Kuwata, T.; Ochiai, A. PTPRZ1 regulates calmodulin phosphorylation and tumor progression in small-cell lung carcinoma. *BMC cancer* **2012**, *12*, 537. DOI: 10.1186/1471-2407-12-537. Published Online: Nov. 21, 2012.
- (97) Goldmann, T.; Otto, F.; Vollmer, E. A receptor-type protein tyrosine phosphatase PTP zeta is expressed in human cutaneous melanomas. *Folia histochemica et cytobiologica* **2000**, *38* (1), 19–20.

- (98) Zhu, R.; Jian, X.-C.; Liu, D.-Y.; Zhou, C.; Wang, Y. Expression of PTPRZ1 in oral squamous cell carcinoma originated from oral submucous fibrosis and its clinical significance. *Shanghai kou qiang yi xue = Shanghai journal of stomatology* **2017**, *26* (2), 198–203.
- (99) Xue, J.; Zhu, W.; Song, J.; Jiao, Y.; Luo, J.; Yu, C.; Zhou, J.; Wu, J.; Chen, M.; Ding, W.-Q.; Cao, J.; Zhang, S. Activation of PPAR α by clofibrate sensitizes pancreatic cancer cells to radiation through the Wnt/ β -catenin pathway. *Oncogene* **2018**, *37* (7), 953–962. DOI: 10.1038/onc.2017.401. Published Online: Oct. 23, 2017.
- (100) Magill, S. T.; Vasudevan, H. N.; Seo, K.; Villanueva-Meyer, J. E.; Choudhury, A.; John Liu, S.; Pekmezci, M.; Findakly, S.; Hilz, S.; Lastella, S.; Demaree, B.; Braunstein, S. E.; Bush, N. A. O.; Aghi, M. K.; Theodosopoulos, P. V.; Sneed, P. K.; Abate, A. R.; Berger, M. S.; McDermott, M. W.; Lim, D. A.; Ullian, E. M.; Costello, J. F.; Raleigh, D. R. Multiplatform genomic profiling and magnetic resonance imaging identify mechanisms underlying intratumor heterogeneity in meningioma. *Nature communications* **2020**, *11* (1), 4803. DOI: 10.1016/j.cell.2016.11.048. Published Online: Sep. 23, 2020.
- (101) Wu, C.-W.; Kao, H.-L.; Li, A. F.-Y.; Chi, C.-W.; Lin, W.-C. Protein tyrosine-phosphatase expression profiling in gastric cancer tissues. *Cancer letters* **2006**, *242* (1), 95–103. DOI: 10.1016/j.canlet.2005.10.046. Published Online: Dec. 7, 2005.
- (102) Lv, J.; Wang, J.; Shang, X.; Liu, F.; Guo, S. Survival prediction in patients with colon adenocarcinoma via multi-omics data integration using a deep learning algorithm. *Bioscience reports* **2020**. DOI: 10.1042/BSR20201482. Published Online: Dec. 1, 2020.
- (103) Foehr, E. D.; Lorente, G.; Kuo, J.; Ram, R.; Nikolich, K.; Urfer, R. Targeting of the receptor protein tyrosine phosphatase beta with a monoclonal antibody delays tumor growth in a glioblastoma model. *Cancer research* **2006**, *66* (4), 2271–2278. DOI: 10.1158/0008-5472.CAN-05-1221.
- (104) Maeda, N.; Noda, M. Involvement of receptor-like protein tyrosine phosphatase zeta/RPTPbeta and its ligand pleiotrophin/heparin-binding growth-associated molecule (HB-GAM) in neuronal migration. *The Journal of cell biology* **1998**, *142* (1), 203–216. DOI: 10.1083/jcb.142.1.203.
- (105) Milev, P.; Chiba, A.; Häring, M.; Rauvala, H.; Schachner, M.; Ranscht, B.; Margolis, R. K.; Margolis, R. U. High affinity binding and overlapping localization of neurocan and phosphacan/protein-tyrosine phosphatase-zeta/beta with tenascin-R, amphoterin, and the heparin-binding growth-associated molecule. *The Journal of biological chemistry* **1998**, *273* (12), 6998–7005. DOI: 10.1074/jbc.273.12.6998.
- (106) Peles, E.; Schlessinger, J.; Grumet, M. Multi-ligand interactions with receptor-like protein tyrosine phosphatase beta: implications for intercellular signaling. *Trends in biochemical sciences* **1998**, *23* (4), 121–124. DOI: 10.1016/s0968-0004(98)01195-5.
- (107) Fujikawa, A.; Sugawara, H.; Tanaka, T.; Matsumoto, M.; Kuboyama, K.; Suzuki, R.; Tanga, N.; Ogata, A.; Masumura, M.; Noda, M. Targeting PTPRZ inhibits stem cell-like properties and tumorigenicity in glioblastoma cells. *Scientific reports* **2017**, *7* (1), 5609. DOI: 10.1038/s41598-017-05931-8. Published Online: Jul. 17, 2017.
- (108) Ulbricht, U.; Eckerich, C.; Fillbrandt, R.; Westphal, M.; Lamszus, K. RNA interference targeting protein tyrosine phosphatase zeta/receptor-type protein tyrosine phosphatase beta suppresses glioblastoma growth in vitro and in vivo. *Journal of neurochemistry* **2006**, *98* (5), 1497–1506. DOI: 10.1111/j.1471-4159.2006.04022.x.
- (109) Lu, K. V.; Jong, K. A.; Kim, G. Y.; Singh, J.; Dia, E. Q.; Yoshimoto, K.; Wang, M. Y.; Cloughesy, T. F.; Nelson, S. F.; Mischel, P. S. Differential induction of glioblastoma migration and growth by two forms of pleiotrophin. *The Journal of biological chemistry* **2005**, *280* (29), 26953–26964. DOI: 10.1074/jbc.M502614200. Published Online: May. 20, 2005.

- (110) Kuboyama, K.; Fujikawa, A.; Suzuki, R.; Tanga, N.; Noda, M. Role of Chondroitin Sulfate (CS) Modification in the Regulation of Protein-tyrosine Phosphatase Receptor Type Z (PTPRZ) Activity: PLEIOTROPHIN-PTPRZ-A SIGNALING IS INVOLVED IN OLIGODENDROCYTE DIFFERENTIATION. *The Journal of biological chemistry* **2016**, *291* (35), 18117–18128. DOI: 10.1074/jbc.M116.742536. Published Online: Jul. 21, 2016.
- (111) Adamsky, K.; Schilling, J.; Garwood, J.; Faissner, A.; Peles, E. Glial tumor cell adhesion is mediated by binding of the FNIII domain of receptor protein tyrosine phosphatase beta (RPTPbeta) to tenascin C. *Oncogene* **2001**, *20* (5), 609–618. DOI: 10.1038/sj.onc.1204119.
- (112) Haas, T. A.; Plow, E. F. Integrin-ligand interactions: a year in review. *Current opinion in cell biology* **1994**, *6* (5), 656–662. DOI: 10.1016/0955-0674(94)90091-4.
- (113) Johnson, W. C.; Pagano, T. G.; Basson, C. T.; Madri, J. A.; Gooley, P.; Armitage, I. M. Biologically active Arg-Gly-Asp oligopeptides assume a type II beta-turn in solution. *Biochemistry* **1993**, *32* (1), 268–273. DOI: 10.1021/bi00052a034.
- (114) Schaffner, F.; Ray, A. M.; Dontenwill, M. Integrin $\alpha 5\beta 1$, the Fibronectin Receptor, as a Pertinent Therapeutic Target in Solid Tumors. *Cancers* **2013**, *5* (1), 27–47. DOI: 10.3390/cancers5010027. Published Online: Jan. 15, 2013.
- (115) Fujikawa, A.; Nagahira, A.; Sugawara, H.; Ishii, K.; Imajo, S.; Matsumoto, M.; Kuboyama, K.; Suzuki, R.; Tanga, N.; Noda, M.; Uchiyama, S.; Tomoo, T.; Ogata, A.; Masumura, M.; Noda, M. Small-molecule inhibition of PTPRZ reduces tumor growth in a rat model of glioblastoma. *Scientific reports* **2016**, *6*, 20473. DOI: 10.1038/srep20473. Published Online: Feb. 9, 2016.
- (116) Dutoit, V.; Migliorini, D.; Ranzanici, G.; Marinari, E.; Widmer, V.; Lobrinus, J. A.; Momjian, S.; Costello, J.; Walker, P. R.; Okada, H.; Weinschenk, T.; Herold-Mende, C.; Dietrich, P.-Y. Antigenic expression and spontaneous immune responses support the use of a selected peptide set from the IMA950 glioblastoma vaccine for immunotherapy of grade II and III glioma. *Oncoimmunology* **2018**, *7* (2), e1391972. DOI: 10.1080/2162402X.2017.1391972. Published Online: Nov. 7, 2017.
- (117) Gharbavi, M.; Danafar, H.; Amani, J.; Sharafi, A. Immuno-informatics analysis and expression of a novel multi-domain antigen as a vaccine candidate against glioblastoma. *International immunopharmacology* **2021**, *91*, 107265. DOI: 10.1016/j.intimp.2020.107265. Published Online: Dec. 25, 2020.
- (118) Hama, T.; Ogura, A.; Omori, A.; Murayama, M.; Kubota, M.; Sekiguchi, M.; Ishiguro, M.; Maruyama, M.; Hatanaka, H.; Sato, K. A 13-Mer peptide of a brain injury-derived protein supports neuronal survival and rescues neurons from injury caused by glutamate. *The Journal of biological chemistry* **1995**, *270* (49), 29067–29070. DOI: 10.1074/jbc.270.49.29067.
- (119) Hama, T.; Murayama, M.; Kato, R.; Ohtake, A.; Sato, K. Amphiphilic helix is essential for the activity of brain injury-derived neurotrophic peptide (BINP). *FEBS letters* **1996**, *396* (2-3), 143–146. DOI: 10.1016/0014-5793(96)01088-5.
- (120) Maruyama, M.; Sato, K.; Ohtake, A.; Ogura, A.; Hama, T. Characteristics of brain injury-derived neurotrophic peptide-binding sites on rat brain synaptosomes and neurons in culture. *Neuroscience* **1999**, *89* (1), 149–156. DOI: 10.1016/s0306-4522(98)00297-8.
- (121) Hama, T.; Maruyama, M. Development of an antibody against a 40,000 mol. wt brain injury-derived neurotrophic peptide-binding protein and identification of a 40,000 mol. wt brain injury-derived neurotrophic peptide-binding protein in hippocampal neurons. *Neuroscience* **2000**, *98* (3), 567–572. DOI: 10.1016/s0306-4522(00)00136-6.
- (122) Hama, T.; Maruyama, M.; Katoh-Semba, R.; Takizawa, M.; Iwashima, M.; Nara, K. Identification and molecular cloning of a novel brain-specific receptor protein that binds to brain injury-derived neurotrophic peptide. Possible role for neuronal survival. *The Journal of*

biological chemistry **2001**, 276 (34), 31929–31935. DOI: 10.1074/jbc.M100617200. Published Online: Jun. 8, 2001.

(123) Barradas, M.; Gonos, E. S.; Zebedee, Z.; Kolettas, E.; Petropoulou, C.; Delgado, M. D.; León, J.; Hara, E.; Serrano, M. Identification of a candidate tumor-suppressor gene specifically activated during Ras-induced senescence. *Experimental cell research* **2002**, 273 (2), 127–137. DOI: 10.1006/excr.2001.5434.

(124) Solovyeva, E. M.; Ibebunjo, C.; Utzinger, S.; Eash, J. K.; Dunbar, A.; Naumann, U.; Zhang, Y.; Serluca, F. C.; Demirci, S.; Oberhauser, B.; Black, F.; Rausch, M.; Hoersch, S.; Meyer, A. S. New insights into molecular changes in skeletal muscle aging and disease: Differential alternative splicing and senescence. *Mechanisms of ageing and development* **2021**, 197, 111510. DOI: 10.1016/j.mad.2021.111510. Published Online: May. 19, 2021.

(125) Silva, J.; Silva, J. M. A.; Barradas, M.; García, J. M.; Domínguez, G.; García, V.; Peña, C.; Gallego, I.; Espinosa, R.; Serrano, M.; Bonilla, F. Analysis of the candidate tumor suppressor Ris-1 in primary human breast carcinomas. *Mutation research* **2006**, 594 (1-2), 78–85. DOI: 10.1016/j.mrfmmm.2005.07.017. Published Online: Nov. 8, 2005.

(126) Nieto, M.; Barradas, M.; Criado, L. M.; Flores, J. M.; Serrano, M.; Llano, E. Normal cellular senescence and cancer susceptibility in mice genetically deficient in Ras-induced senescence-1 (Ris1). *Oncogene* **2007**, 26 (12), 1673–1680. DOI: 10.1038/sj.onc.1209978. Published Online: Sep. 11, 2006.

(127) Cheng, Z.; Guo, J.; Chen, L.; Luo, N.; Yang, W.; Qu, X. Overexpression of TMEM158 contributes to ovarian carcinogenesis. *Journal of experimental & clinical cancer research : CR* **2015**, 34, 75. DOI: 10.1186/s13046-015-0193-y. Published Online: Aug. 4, 2015.

(128) Tong, J.; Li, H.; Hu, Y.; Zhao, Z.; Li, M. TMEM158 Regulates the Canonical and Non-Canonical Pathways of TGF- β to Mediate EMT in Triple-Negative Breast Cancer. *Journal of Cancer* **2022**, 13 (8), 2694–2704. DOI: 10.7150/jca.65822. Published Online: May. 21, 2022.

(129) Fu, Y.; Yao, N.; Ding, D.; Zhang, X.; Liu, H.; Le Ma; Shi, W.; Zhu, C.; Tang, L. TMEM158 promotes pancreatic cancer aggressiveness by activation of TGF β 1 and PI3K/AKT signaling pathway. *Journal of cellular physiology* **2020**, 235 (3), 2761–2775. DOI: 10.1002/jcp.29181. Published Online: Sep. 17, 2019.

(130) Liu, L.; Zhang, J.; Li, S.; Yin, L.; Tai, J. Silencing of TMEM158 Inhibits Tumorigenesis and Multidrug Resistance in Colorectal Cancer. *Nutrition and cancer* **2020**, 72 (4), 662–671. DOI: 10.1080/01635581.2019.1650192. Published Online: Aug. 7, 2019.

(131) Mohammed, A. E. S.; Eguchi, H.; Wada, S.; Koyama, N.; Shimizu, M.; Otani, K.; Ohtaki, M.; Tanimoto, K.; Hiyama, K.; Gaber, M. S.; Nishiyama, M. TMEM158 and FBLP1 as novel marker genes of cisplatin sensitivity in non-small cell lung cancer cells. *Experimental lung research* **2012**, 38 (9-10), 463–474. DOI: 10.3109/01902148.2012.731625.

(132) Player, A.; Abraham, N.; Burrell, K.; Bengone, I. O.; Harris, A.; Nunez, L.; Willaims, T.; Kwende, S.; Walls, W. Identification of candidate genes associated with triple negative breast cancer. *Genes & cancer* **2017**, 8 (7-8), 659–672. DOI: 10.18632/genesandcancer.147.

(133) Li, H.-N.; Du, Y.-Y.; Xu, T.; Zhang, R.; Wang, G.; Lv, Z.-T.; Li, X.-R. TMEM158 May Serve as a Diagnostic Biomarker for Anaplastic Thyroid Carcinoma: An Integrated Bioinformatic Analysis. *Current medical science* **2020**, 40 (6), 1137–1147. DOI: 10.1007/s11596-020-2296-8. Published Online: Jan. 11, 2021.

(134) Weinberger, P.; Ponny, S. R.; Xu, H.; Bai, S.; Smallridge, R.; Copland, J.; Sharma, A. Cell Cycle M-Phase Genes Are Highly Upregulated in Anaplastic Thyroid Carcinoma. *Thyroid : official journal of the American Thyroid Association* **2017**, 27 (2), 236–252. DOI: 10.1089/thy.2016.0285. Published Online: Dec. 15, 2016.

- (135) Li, J.; Wang, X.; Chen, L.; Zhang, J.; Zhang, Y.; Ren, X.; Sun, J.; Fan, X.; Fan, J.; Li, T.; Tong, L.; Yi, L.; Chen, L.; Liu, J.; Shang, G.; Ren, X.; Zhang, H.; Yu, S.; Ming, H.; Huang, Q.; Dong, J.; Zhang, C.; Yang, X. TMEM158 promotes the proliferation and migration of glioma cells via STAT3 signaling in glioblastomas. *Cancer gene therapy* **2022**. DOI: 10.1038/s41417-021-00414-5. Published Online: Jan. 6, 2022.
- (136) <https://portal.gdc.cancer.gov/genes/ENSG00000249992>, 04.12.2018.
- (137) Blum, A.; Wang, P.; Zenklusen, J. C. SnapShot: TCGA-Analyzed Tumors. *Cell* **2018**, *173* (2), 530. DOI: 10.1016/j.cell.2018.03.059.
- (138) Comprehensive genomic characterization defines human glioblastoma genes and core pathways. *Nature* **2008**, *455* (7216), 1061–1068. DOI: 10.1038/nature07385. Published Online: Sep. 4, 2008.
- (139) <https://gtexportal.org/home/gene/TMEM158>, 09.09.2019.
- (140) The Genotype-Tissue Expression (GTEx) project. *Nature genetics* **2013**, *45* (6), 580–585. DOI: 10.1038/ng.2653.
- (141) <http://gepia.cancer-pku.cn/detail.php?gene=tmem158>, 29.09.2022.
- (142) Tang, Z.; Li, C.; Kang, B.; Gao, G.; Li, C.; Zhang, Z. GEPIA: a web server for cancer and normal gene expression profiling and interactive analyses. *Nucleic acids research* **2017**, *45* (W1), W98–W102. DOI: 10.1093/nar/gkx247.
- (143) Helsen, C. W.; Hammill, J. A.; Lau, V. W. C.; Mwawasi, K. A.; Afsahi, A.; Bezverbnaya, K.; Newhook, L.; Hayes, D. L.; Aarts, C.; Bojovic, B.; Denisova, G. F.; Kwiecien, J. M.; Brain, I.; Derocher, H.; Milne, K.; Nelson, B. H.; Bramson, J. L. The chimeric TAC receptor co-opts the T cell receptor yielding robust anti-tumor activity without toxicity. *Nature communications* **2018**, *9* (1), 3049. DOI: 10.1038/s41467-018-05395-y. Published Online: Aug. 3, 2018.
- (144) Allan, S. E.; Alstad, A. N.; Merindol, N.; Crellin, N. K.; Amendola, M.; Bacchetta, R.; Naldini, L.; Roncarolo, M. G.; Soudeyns, H.; Levings, M. K. Generation of potent and stable human CD4+ T regulatory cells by activation-independent expression of FOXP3. *Molecular therapy : the journal of the American Society of Gene Therapy* **2008**, *16* (1), 194–202. DOI: 10.1038/sj.mt.6300341. Published Online: Nov. 6, 2007.
- (145) Hammill, J. A.; VanSeggelen, H.; Helsen, C. W.; Denisova, G. F.; Eveleigh, C.; Tantaló, D. G. M.; Bassett, J. D.; Bramson, J. L. Designed ankyrin repeat proteins are effective targeting elements for chimeric antigen receptors. *Journal for immunotherapy of cancer* **2015**, *3*, 55. DOI: 10.1186/s40425-015-0099-4. Published Online: Dec. 15, 2015.
- (146) Przybylski, S.; Gasch, M.; Marschner, A.; Ebert, M.; Ewe, A.; Helmig, G.; Hilger, N.; Fricke, S.; Rudzok, S.; Aigner, A.; Burkhardt, J. Influence of nanoparticle-mediated transfection on proliferation of primary immune cells in vitro and in vivo. *PloS one* **2017**, *12* (5), e0176517. DOI: 10.1371/journal.pone.0176517. Published Online: May. 2, 2017.
- (147) Lu, J.; Zhang, X.; Shen, T.; Ma, C.; Wu, J.; Kong, H.; Tian, J.; Shao, Z.; Zhao, X.; Xu, L. Epigenetic Profiling of H3K4Me3 Reveals Herbal Medicine Jinfukang-Induced Epigenetic Alteration Is Involved in Anti-Lung Cancer Activity. *Evidence-based complementary and alternative medicine : eCAM* **2016**, *2016*, 7276161. DOI: 10.1155/2016/7276161. Published Online: Mar. 20, 2016.
- (148) Andreansky, S.; He, B.; van Cott, J.; McGhee, J.; Markert, J. M.; Gillespie, G. Y.; Roizman, B.; Whitley, R. J. Treatment of intracranial gliomas in immunocompetent mice using herpes simplex viruses that express murine interleukins. *Gene therapy* **1998**, *5* (1), 121–130. DOI: 10.1038/sj.gt.3300550.
- (149) Szatmári, T.; Lumniczky, K.; Désaknai, S.; Trajcevski, S.; Hídvégi, E. J.; Hamada, H.; Sáfrány, G. Detailed characterization of the mouse glioma 261 tumor model for experimental

glioblastoma therapy. *Cancer science* **2006**, 97 (6), 546–553. DOI: 10.1111/j.1349-7006.2006.00208.x.

(150) https://www.bioinformatics.org/sms/prot_mw.html, 29.09.2022.

(151) Bigner, D. D.; Bigner, S. H.; Pontén, J.; Westermark, B.; Mahaley, M. S.; Ruoslahti, E.; Herschman, H.; Eng, L. F.; Wikstrand, C. J. Heterogeneity of Genotypic and phenotypic characteristics of fifteen permanent cell lines derived from human gliomas. *Journal of neuropathology and experimental neurology* **1981**, 40 (3), 201–229. DOI: 10.1097/00005072-198105000-00001.

(152) Johnson, H.; White, F. M. Quantitative analysis of signaling networks across differentially embedded tumors highlights interpatient heterogeneity in human glioblastoma. *Journal of proteome research* **2014**, 13 (11), 4581–4593. DOI: 10.1021/pr500418w. Published Online: Jun. 24, 2014.

(153) Brown, D. V.; Daniel, P. M.; D'Abaco, G. M.; Gogos, A.; Ng, W.; Morokoff, A. P.; Mantamadiotis, T. Coexpression analysis of CD133 and CD44 identifies proneural and mesenchymal subtypes of glioblastoma multiforme. *Oncotarget* **2015**, 6 (8), 6267–6280. DOI: 10.18632/oncotarget.3365.

(154) Wang, J.-B.; Dong, D.-F.; Wang, M.-D.; Gao, K. IDH1 overexpression induced chemotherapy resistance and IDH1 mutation enhanced chemotherapy sensitivity in Glioma cells in vitro and in vivo. *Asian Pacific journal of cancer prevention : APJCP* **2014**, 15 (1), 427–432. DOI: 10.7314/apjcp.2014.15.1.427.

(155) Tönjes, M.; Barbus, S.; Park, Y. J.; Wang, W.; Schlotter, M.; Lindroth, A. M.; Pleier, S. V.; Bai, A. H. C.; Karra, D.; Piro, R. M.; Felsberg, J.; Addington, A.; Lemke, D.; Weibrecht, I.; Hovestadt, V.; Rolli, C. G.; Campos, B.; Turcan, S.; Sturm, D.; Witt, H.; Chan, T. A.; Herold-Mende, C.; Kemkemmer, R.; König, R.; Schmidt, K.; Hull, W.-E.; Pfister, S. M.; Jugold, M.; Hutson, S. M.; Plass, C.; Okun, J. G.; Reifenberger, G.; Lichter, P.; Radlwimmer, B. BCAT1 promotes cell proliferation through amino acid catabolism in gliomas carrying wild-type IDH1. *Nature medicine* **2013**, 19 (7), 901–908. DOI: 10.1038/nm.3217. Published Online: Jun. 23, 2013.

(156) Fabian Flemig. Einfluss PNGase-basierter Deglykosylierung von Glioblastomzellen auf CAR-T vermittelte Zytotoxizität:[unpublished bachelor's thesis], South Westphalia University of Applied Science, 2020.

(157) Zanetti-Domingues, L. C.; Tynan, C. J.; Rolfe, D. J.; Clarke, D. T.; Martin-Fernandez, M. Hydrophobic fluorescent probes introduce artifacts into single molecule tracking experiments due to non-specific binding. *PLoS one* **2013**, 8 (9), e74200. DOI: 10.1371/journal.pone.0074200. Published Online: Sep. 16, 2013.

(158) Lu, T.; Lin, Z.; Ren, J.; Yao, P.; Wang, X.; Wang, Z.; Zhang, Q. The Non-Specific Binding of Fluorescent-Labeled MiRNAs on Cell Surface by Hydrophobic Interaction. *PLoS one* **2016**, 11 (3), e0149751. DOI: 10.1371/journal.pone.0149751. Published Online: Mar. 1, 2016.

(159) Adiraj Iyer, M.; Eddington, D. T. Storing and releasing rhodamine as a model hydrophobic compound in polydimethylsiloxane microfluidic devices. *Lab on a chip* **2019**, 19 (4), 574–579. DOI: 10.1039/c9lc00039a.

(160) sciencegateway.org/tools/proteinmw.htm, 29.09.2022.

(161) Jäger, V.; Büssow, K.; Wagner, A.; Weber, S.; Hust, M.; Frenzel, A.; Schirrmann, T. High level transient production of recombinant antibodies and antibody fusion proteins in HEK293 cells. *BMC biotechnology* **2013**, 13, 52. DOI: 10.1186/1472-6750-13-52. Published Online: Jun. 26, 2013.

(162) Nelson, N.; Lopez-Pelaez, M.; Palazon, A.; Poon, E.; La Roche, M. de; Barry, S.; Valge-Archer, V.; Wilkinson, R. W.; Dovedi, S. J.; Smith, P. D. A cell-engineered system to assess

tumor cell sensitivity to CD8+ T cell-mediated cytotoxicity. *Oncoimmunology* **2019**, *8* (8), 1599635. DOI: 10.1080/2162402X.2019.1599635. Published Online: Apr. 26, 2019.

(163) Mineo, J.-F.; Bordron, A.; Quintin-Roué, I.; Loisel, S.; Ster, K. L.; Buhé, V.; Lagarde, N.; Berthou, C. Recombinant humanised anti-HER2/neu antibody (Herceptin) induces cellular death of glioblastomas. *British journal of cancer* **2004**, *91* (6), 1195–1199. DOI: 10.1038/sj.bjc.6602089.

(164) Achenbach, C. von; Weller, M.; Szabo, E. Epidermal growth factor receptor and ligand family expression and activity in glioblastoma. *Journal of neurochemistry* **2018**, *147* (1), 99–109. DOI: 10.1111/jnc.14538. Published Online: Aug. 16, 2018.

(165) Richards, K. N.; Zweidler-McKay, P. A.; van Roy, N.; Speleman, F.; Trevino, J.; Zage, P. E.; Hughes, D. P. M. Signaling of ERBB receptor tyrosine kinases promotes neuroblastoma growth in vitro and in vivo. *Cancer* **2010**, *116* (13), 3233–3243. DOI: 10.1002/cncr.25073.

(166) Yimchuen, W.; Kadonosono, T.; Ota, Y.; Sato, S.; Kitazawa, M.; Shiozawa, T.; Kuchimaru, T.; Taki, M.; Ito, Y.; Nakamura, H.; Kizaka-Kondoh, S. Strategic design to create HER2-targeting proteins with target-binding peptides immobilized on a fibronectin type III domain scaffold. *RSC advances* **2020**, *10* (26), 15154–15162. DOI: 10.1039/d0ra00427h. Published Online: Apr. 17, 2020.

(167) Biedler, J. L.; Helson, L.; Spengler, B. A. Morphology and growth, tumorigenicity, and cytogenetics of human neuroblastoma cells in continuous culture. *Cancer research* **1973**, *33* (11), 2643–2652.

(168) Kovalevich, J.; Langford, D. Considerations for the use of SH-SY5Y neuroblastoma cells in neurobiology. *Methods in molecular biology (Clifton, N.J.)* **2013**, *1078*, 9–21. DOI: 10.1007/978-1-62703-640-5_2.

(169) Zheng, L.; Hu, P.; Wolfe, B.; Gonsalves, C.; Ren, L.; Khawli, L. A.; Kaslow, H. R.; Epstein, A. L. Lym-1 Chimeric Antigen Receptor T Cells Exhibit Potent Anti-Tumor Effects against B-Cell Lymphoma. *International journal of molecular sciences* **2017**, *18* (12). DOI: 10.3390/ijms18122773. Published Online: Dec. 20, 2017.

(170) Schnalzger, T. E.; Groot, M. H. de; Zhang, C.; Mosa, M. H.; Michels, B. E.; Röder, J.; Darvishi, T.; Wels, W. S.; Farin, H. F. 3D model for CAR-mediated cytotoxicity using patient-derived colorectal cancer organoids. *The EMBO journal* **2019**, *38* (12). DOI: 10.15252/emboj.2018100928. Published Online: Apr. 29, 2019.

(171) Majzner, R. G.; Rietberg, S. P.; Sotillo, E.; Dong, R.; Vachharajani, V. T.; Labanieh, L.; Myklebust, J. H.; Kadapakkam, M.; Weber, E. W.; Tousley, A. M.; Richards, R. M.; Heitzeneder, S.; Nguyen, S. M.; Wiebking, V.; Theruvath, J.; Lynn, R. C.; Xu, P.; Dunn, A. R.; Vale, R. D.; Mackall, C. L. Tuning the Antigen Density Requirement for CAR T-cell Activity. *Cancer discovery* **2020**, *10* (5), 702–723. DOI: 10.1158/2159-8290.CD-19-0945. Published Online: Mar. 19, 2020.

(172) Brown, C. E.; Aguilar, B.; Starr, R.; Yang, X.; Chang, W.-C.; Weng, L.; Chang, B.; Sarkissian, A.; Brito, A.; Sanchez, J. F.; Ostberg, J. R.; D'Apuzzo, M.; Badie, B.; Barish, M. E.; Forman, S. J. Optimization of IL13R α 2-Targeted Chimeric Antigen Receptor T Cells for Improved Anti-tumor Efficacy against Glioblastoma. *Molecular therapy : the journal of the American Society of Gene Therapy* **2018**, *26* (1), 31–44. DOI: 10.1016/j.ymthe.2017.10.002. Published Online: Oct. 5, 2017.

(173) Lin, E. C.; Ratnikov, B. I.; Tsai, P. M.; Carron, C. P.; Myers, D. M.; Barbas, C. F.; Smith, J. W. Identification of a region in the integrin beta3 subunit that confers ligand binding specificity. *The Journal of biological chemistry* **1997**, *272* (38), 23912–23920. DOI: 10.1074/jbc.272.38.23912.

- (174) Whilding, L. M.; Halim, L.; Draper, B.; Parente-Pereira, A. C.; Zabinski, T.; Davies, D. M.; Maher, J. CAR T-Cells Targeting the Integrin $\alpha\beta6$ and Co-Expressing the Chemokine Receptor CXCR2 Demonstrate Enhanced Homing and Efficacy against Several Solid Malignancies. *Cancers* **2019**, *11* (5). DOI: 10.3390/cancers11050674. Published Online: May. 14, 2019.
- (175) Cobb, D. A.; Rossi, J. de; Liu, L.; An, E.; Lee, D. W. Targeting of the $\alpha\beta3$ integrin complex by CAR-T cells leads to rapid regression of diffuse intrinsic pontine glioma and glioblastoma. *Journal for immunotherapy of cancer* **2022**, *10* (2). DOI: 10.1136/jitc-2021-003816.
- (176) Fu, X.; Rivera, A.; Tao, L.; Zhang, X. Genetically modified T cells targeting neovasculature efficiently destroy tumor blood vessels, shrink established solid tumors and increase nanoparticle delivery. *International journal of cancer* **2013**, *133*(10), 2483–2492. DOI: 10.1002/ijc.28269. Published Online: Jul. 11, 2013.
- (177) Whilding, L. M.; Parente-Pereira, A. C.; Zabinski, T.; Davies, D. M.; Petrovic, R. M. G.; Kao, Y. V.; Saxena, S. A.; Romain, A.; Costa-Guerra, J. A.; Violette, S.; Itamochi, H.; Ghaem-Maghani, S.; Vallath, S.; Marshall, J. F.; Maher, J. Targeting of Aberrant $\alpha\beta6$ Integrin Expression in Solid Tumors Using Chimeric Antigen Receptor-Engineered T Cells. *Molecular therapy : the journal of the American Society of Gene Therapy* **2017**, *25* (1), 259–273. DOI: 10.1016/j.ymthe.2016.10.012. Published Online: Jan. 4, 2017.
- (178) Schittenhelm, J.; Schwab, E. I.; Sperveslage, J.; Tatagiba, M.; Meyermann, R.; Fend, F.; Goodman, S. L.; Sipos, B. Longitudinal expression analysis of $\alpha\beta3$ integrins in human gliomas reveals upregulation of integrin $\alpha\beta3$ as a negative prognostic factor. *Journal of neuropathology and experimental neurology* **2013**, *72* (3), 194–210. DOI: 10.1097/NEN.0b013e3182851019.
- (179) Ruoslahti, E. RGD and other recognition sequences for integrins. *Annual review of cell and developmental biology* **1996**, *12*, 697–715. DOI: 10.1146/annurev.cellbio.12.1.697.
- (180) Isal, S.; Pierson, J.; Imbert, L.; Clement, A.; Collet, C.; Pinel, S.; Veran, N.; Reinhard, A.; Poussier, S.; Gauchotte, G.; Frezier, S.; Karcher, G.; Marie, P.-Y.; Maskali, F. PET imaging of ^{68}Ga -NODAGA-RGD, as compared with ^{18}F -fluorodeoxyglucose, in experimental rodent models of engrafted glioblastoma. *EJNMMI research* **2018**, *8* (1), 51. DOI: 10.1186/s13550-018-0405-5. Published Online: Jun. 15, 2018.
- (181) Durante, S.; Dunet, V.; Gorostidi, F.; Mitsakis, P.; Schaefer, N.; Delage, J.; Prior, J. O. Head and neck tumors angiogenesis imaging with ^{68}Ga -NODAGA-RGD in comparison to ^{18}F -FDG PET/CT: a pilot study. *EJNMMI research* **2020**, *10* (1), 47. DOI: 10.1186/s13550-020-00638-w. Published Online: May. 7, 2020.
- (182) Gabathuler, R. Approaches to transport therapeutic drugs across the blood-brain barrier to treat brain diseases. *Neurobiology of disease* **2010**, *37* (1), 48–57. DOI: 10.1016/j.nbd.2009.07.028. Published Online: Aug. 5, 2009.
- (183) Zhang, C.; Burger, M. C.; Jennewein, L.; Genßler, S.; Schönfeld, K.; Zeiner, P.; Hattingen, E.; Harter, P. N.; Mittelbronn, M.; Tonn, T.; Steinbach, J. P.; Wels, W. S. ErbB2/HER2-Specific NK Cells for Targeted Therapy of Glioblastoma. *Journal of the National Cancer Institute* **2016**, *108* (5). DOI: 10.1093/jnci/djv375. Published Online: Dec. 6, 2015.
- (184) Jiang, H.; Gao, H.; Kong, J.; Song, B.; Wang, P.; Shi, B.; Wang, H.; Li, Z. Selective Targeting of Glioblastoma with EGFRvIII/EGFR Bitargeted Chimeric Antigen Receptor T Cell. *Cancer immunology research* **2018**, *6* (11), 1314–1326. DOI: 10.1158/2326-6066.CIR-18-0044. Published Online: Sep. 10, 2018.
- (185) Niisato, K.; Fujikawa, A.; Komai, S.; Shintani, T.; Watanabe, E.; Sakaguchi, G.; Katsuura, G.; Manabe, T.; Noda, M. Age-dependent enhancement of hippocampal long-term potentiation and impairment of spatial learning through the Rho-associated kinase pathway in

protein tyrosine phosphatase receptor type Z-deficient mice. *The Journal of neuroscience : the official journal of the Society for Neuroscience* **2005**, 25 (5), 1081–1088. DOI: 10.1523/JNEUROSCI.2565.04.2005.

(186) Tamura, H.; Fukada, M.; Fujikawa, A.; Noda, M. Protein tyrosine phosphatase receptor type Z is involved in hippocampus-dependent memory formation through dephosphorylation at Y1105 on p190 RhoGAP. *Neuroscience letters* **2006**, 399 (1-2), 33–38. DOI: 10.1016/j.neulet.2006.01.045. Published Online: Feb. 28, 2006.

(187) Tanga, N.; Kuboyama, K.; Kishimoto, A.; Kihara, M.; Kiyonari, H.; Watanabe, T.; Fujikawa, A.; Noda, M. Behavioral and neurological analyses of adult mice carrying null and distinct loss-of-receptor function mutations in protein tyrosine phosphatase receptor type Z (PTPRZ). *PloS one* **2019**, 14 (6), e0217880. DOI: 10.1371/journal.pone.0217880. Published Online: Jun. 13, 2019.

(188) Eill, G. J.; Sinha, A.; Morawski, M.; Viapiano, M. S.; Matthews, R. T. The protein tyrosine phosphatase RPTP ζ /phosphacan is critical for perineuronal net structure. *The Journal of biological chemistry* **2020**, 295 (4), 955–968. DOI: 10.1074/jbc.RA119.010830. Published Online: Dec. 10, 2019.

(189) Narentuya, Takeda-Uchimura, Y.; Foyez, T.; Zhang, Z.; Akama, T. O.; Yagi, H.; Kato, K.; Komatsu, Y.; Kadomatsu, K.; Uchimura, K. GlcNAc6ST3 is a keratan sulfate sulfotransferase for the protein-tyrosine phosphatase PTPRZ in the adult brain. *Scientific reports* **2019**, 9 (1), 4387. DOI: 10.1038/s41598-019-40901-2. Published Online: Mar. 13, 2019.

(190) García-Pérez, D.; Laorden, M. L.; Milanés, M. V. Acute Morphine, Chronic Morphine, and Morphine Withdrawal Differently Affect Pleiotrophin, Midkine, and Receptor Protein Tyrosine Phosphatase β/ζ Regulation in the Ventral Tegmental Area. *Molecular neurobiology* **2017**, 54 (1), 495–510. DOI: 10.1007/s12035-015-9631-2. Published Online: Jan. 7, 2016.

(191) Fernández-Calle, R.; Vicente-Rodríguez, M.; Pastor, M.; Gramage, E.; Di Geronimo, B.; Zapico, J. M.; Coderch, C.; Pérez-García, C.; Lasek, A. W.; Pascual-Teresa, B. de; Ramos, A.; Herradón, G. Pharmacological inhibition of Receptor Protein Tyrosine Phosphatase β/ζ (PTPRZ1) modulates behavioral responses to ethanol. *Neuropharmacology* **2018**, 137, 86–95. DOI: 10.1016/j.neuropharm.2018.04.027. Published Online: May. 9, 2018.

(192) Fujikawa, A.; Noda, Y.; Yamamoto, H.; Tanga, N.; Sakaguchi, G.; Hattori, S.; Song, W.-J.; Sora, I.; Nabeshima, T.; Katsuura, G.; Noda, M. Mice deficient in protein tyrosine phosphatase receptor type Z (PTPRZ) show reduced responsivity to methamphetamine despite an enhanced response to novelty. *PloS one* **2019**, 14 (8), e0221205. DOI: 10.1371/journal.pone.0221205. Published Online: Aug. 20, 2019.

(193) Fernández-Calle, R.; Gramage, E.; Zapico, J. M.; Pascual-Teresa, B. de; Ramos, A.; Herradón, G. Inhibition of RPTP β/ζ blocks ethanol-induced conditioned place preference in pleiotrophin knockout mice. *Behavioural brain research* **2019**, 369, 111933. DOI: 10.1016/j.bbr.2019.111933. Published Online: May. 1, 2019.

(194) Ashizawa, T.; Miyata, H.; Iizuka, A.; Komiyama, M.; Oshita, C.; Kume, A.; Nogami, M.; Yagoto, M.; Ito, I.; Oishi, T.; Watanabe, R.; Mitsuya, K.; Matsuno, K.; Furuya, T.; Okawara, T.; Otsuka, M.; Ogo, N.; Asai, A.; Nakasu, Y.; Yamaguchi, K.; Akiyama, Y. Effect of the STAT3 inhibitor STX-0119 on the proliferation of cancer stem-like cells derived from recurrent glioblastoma. *International journal of oncology* **2013**, 43 (1), 219–227. DOI: 10.3892/ijo.2013.1916. Published Online: Apr. 23, 2013.

(195) Miettinen, P. J.; Ebner, R.; Lopez, A. R.; Derynck, R. TGF-beta induced transdifferentiation of mammary epithelial cells to mesenchymal cells: involvement of type I receptors. *The Journal of cell biology* **1994**, 127 (6 Pt 2), 2021–2036. DOI: 10.1083/jcb.127.6.2021.

- (196) Weller, M.; Fontana, A. The failure of current immunotherapy for malignant glioma. Tumor-derived TGF-beta, T-cell apoptosis, and the immune privilege of the brain. *Brain research. Brain research reviews* **1995**, *21* (2), 128–151. DOI: 10.1016/0165-0173(95)00010-0.
- (197) Liu, R.-Y.; Zeng, Y.; Lei, Z.; Wang, L.; Yang, H.; Liu, Z.; Zhao, J.; Zhang, H.-T. JAK/STAT3 signaling is required for TGF- β -induced epithelial-mesenchymal transition in lung cancer cells. *International journal of oncology* **2014**, *44* (5), 1643–1651. DOI: 10.3892/ijo.2014.2310. Published Online: Feb. 21, 2014.
- (198) Xu, Y.-Y.; Guo, M.; Yang, L.-Q.; Zhou, F.; Yu, C.; Wang, A.; Pang, T.-H.; Wu, H.-Y.; Zou, X.-P.; Zhang, W.-J.; Wang, L.; Xu, G.-F.; Huang, Q. Regulation of CD44v6 expression in gastric carcinoma by the IL-6/STAT3 signaling pathway and its clinical significance. *Oncotarget* **2017**, *8* (28), 45848–45861. DOI: 10.18632/oncotarget.17435.
- (199) So, J. Y.; Smolarek, A. K.; Salerno, D. M.; Maehr, H.; Uskokovic, M.; Liu, F.; Suh, N. Targeting CD44-STAT3 signaling by Gemini vitamin D analog leads to inhibition of invasion in basal-like breast cancer. *PloS one* **2013**, *8* (1), e54020. DOI: 10.1371/journal.pone.0054020. Published Online: Jan. 11, 2013.
- (200) Cho, S. H.; Park, Y. S.; Kim, H. J.; Kim, C. H.; Lim, S. W.; Huh, J. W.; Lee, J. H.; Kim, H. R. CD44 enhances the epithelial-mesenchymal transition in association with colon cancer invasion. *International journal of oncology* **2012**, *41* (1), 211–218. DOI: 10.3892/ijo.2012.1453. Published Online: Apr. 30, 2012.
- (201) Bates, R. C.; Edwards, N. S.; Burns, G. F.; Fisher, D. E. A CD44 survival pathway triggers chemoresistance via lyn kinase and phosphoinositide 3-kinase/Akt in colon carcinoma cells. *Cancer research* **2001**, *61* (13), 5275–5283.
- (202) Corbetta, C.; Di Ianni, N.; Bruzzone, M. G.; Patanè, M.; Pollo, B.; Cantini, G.; Cominelli, M.; Zucca, I.; Pisati, F.; Poliani, P. L.; Finocchiaro, G.; Pellegatta, S. Altered function of the glutamate-aspartate transporter GLAST, a potential therapeutic target in glioblastoma. *International journal of cancer* **2019**, *144* (10), 2539–2554. DOI: 10.1002/ijc.31985. Published Online: Jan. 5, 2019.
- (203) Lyons, S. A.; Chung, W. J.; Weaver, A. K.; Ogunrinu, T.; Sontheimer, H. Autocrine glutamate signaling promotes glioma cell invasion. *Cancer research* **2007**, *67* (19), 9463–9471. DOI: 10.1158/0008-5472.CAN-07-2034.
- (204) Ishiuchi, S.; Tsuzuki, K.; Yoshida, Y.; Yamada, N.; Hagimura, N.; Okado, H.; Miwa, A.; Kurihara, H.; Nakazato, Y.; Tamura, M.; Sasaki, T.; Ozawa, S. Blockage of Ca(2+)-permeable AMPA receptors suppresses migration and induces apoptosis in human glioblastoma cells. *Nature medicine* **2002**, *8* (9), 971–978. DOI: 10.1038/nm746. Published Online: Aug. 12, 2002.
- (205) Fedorov, V. D.; Themeli, M.; Sadelain, M. PD-1- and CTLA-4-based inhibitory chimeric antigen receptors (iCARs) divert off-target immunotherapy responses. *Science translational medicine* **2013**, *5* (215), 215ra172. DOI: 10.1126/scitranslmed.3006597.
- (206) Hawthorne, V. S.; Huang, W.-C.; Neal, C. L.; Tseng, L.-M.; Hung, M.-C.; Yu, D. ErbB2-mediated Src and signal transducer and activator of transcription 3 activation leads to transcriptional up-regulation of p21Cip1 and chemoresistance in breast cancer cells. *Molecular cancer research : MCR* **2009**, *7* (4), 592–600. DOI: 10.1158/1541-7786.MCR-08-0316.
- (207) <https://www.ebi.ac.uk/Tools/msa/clustalo/#:~:text=Clustal%20Omega%20is%20a%20new,our%20pairwise%20sequence%20alignment%20tools,29.09.2022.>
- (208) <https://www.uniprot.org/uniprotkb?query=tmem158,29.09.2022.>

8 Appendix

8.1 Maps of lentiviral packaging vectors

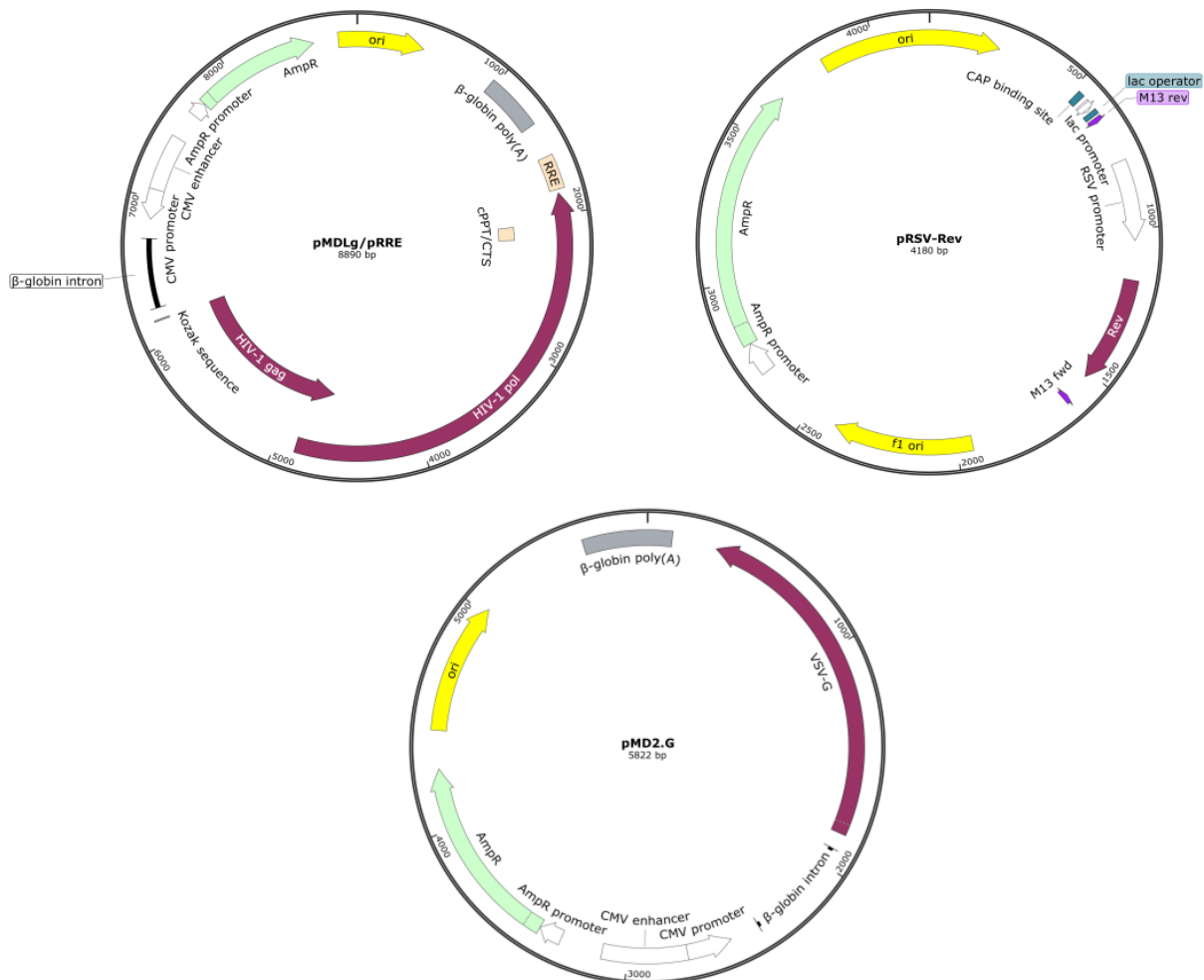


Figure 17: Genetic maps of vectors used for production of lentiviral particles. The vectors encode the genes for production of infectious but replication deficient viral particles, namely HIV-1 gag and -pol (pMDLg/pRRE), as well as Rev (pRSV-Rev). The produced viral particles are pseudotyped by the VSV-G envelope, encoded on the pMD2.G vector. Maps were downloaded from www.addgene.org. Abbreviations: Amp^r, Ampicillin resistance; CAP, catabolite activator protein; CMV, cytomegalovirus; cPPT/CTS, central polypurine tract/central termination sequence; HIV-1, human immunodeficiency virus 1; lac, lactose (promoter/operator); ori, origin of replication, RRE, Rev response element; RSV, respiratory syncytial virus; VSV-G, vesicular stomatitis virus glycoprotein G.

8.2 Expression of TMEM158 and PTPRZ1 in glioma and non-glioma tumor entities and overall survival in GBM

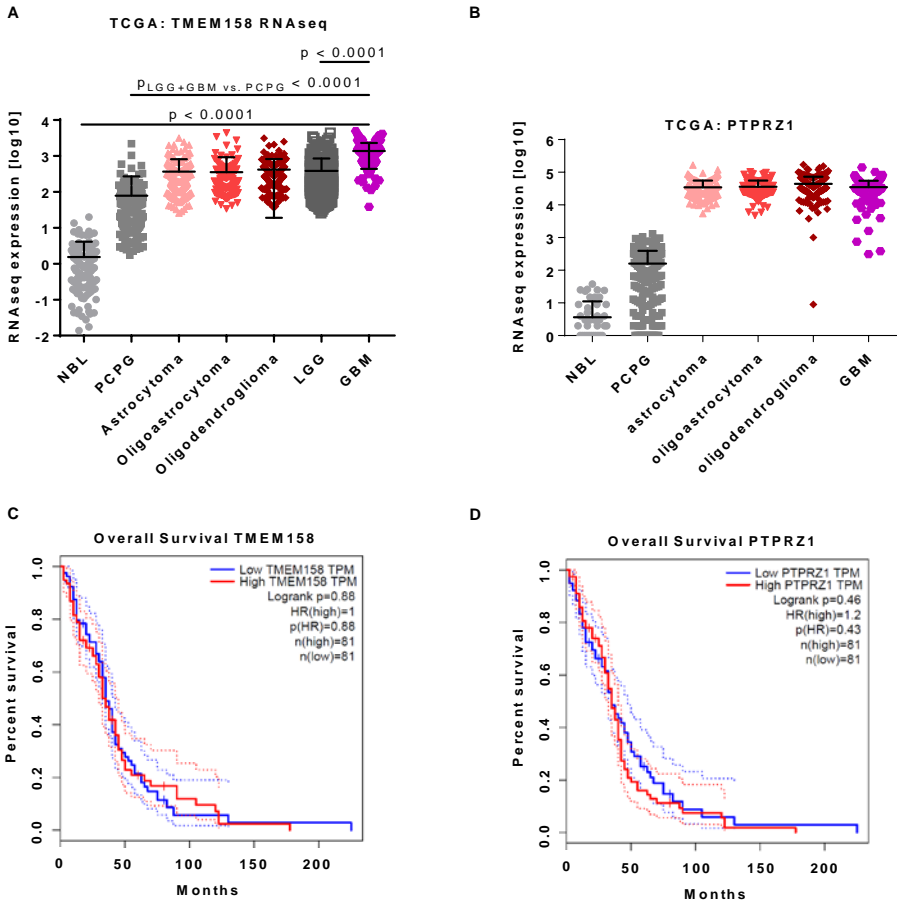


Figure 18: Expression of TMEM158 and PTPRZ1 in brain tumor entities and survival of GBM patients. A/B) Expression of TMEM158 (A) or PTPRZ1 (B) in different brain tumor entities is shown. Illustrated are sub-cohorts of TCGA datasets including clinical subtype for astrocytoma (n=197), oligoastrocytoma (n=134) and oligodendroglioma (n=198). In addition, neuroblastoma (NBL) samples from the TARGET panel and from the TCGA (GBM/LGG), as well as from paraganglioma (PCPG) datasets are shown. Gene expression values are depicted as log10-transformed and means \pm 95 % confidence intervals (CI). Statistical significance was determined by a T-test. The analysis was performed by Dr. Jana Burkhardt. **C/D)** Overall survival of GBM patients, expressing low (< median) or high (> median) of the *TMEM158* (C) or *PTPRZ1* (D). Hazard ratio and corresponding p-values are indicated as well.

8.3 Titration of anti-TMEM158 Western blot antibodies

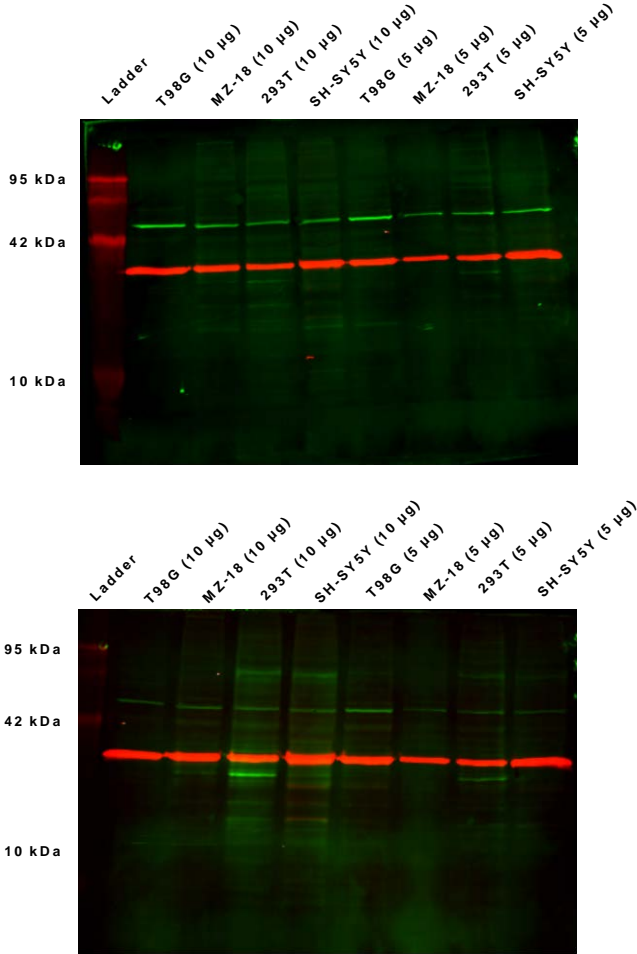


Figure 19: Western Blot of GBM and non-GBM cell lines stained for TMEM158 and GAPDH. Bands shown in green represent TMEM158, while red bands indicate GAPDH, which was used as loading control. Blots were stained with either 1:1500 (left) or 1:3000 (right) dilution of the anti-TMEM158 antibody (ab98335).

8.4 Western Blot of TMEM158 before and after deglycosylation

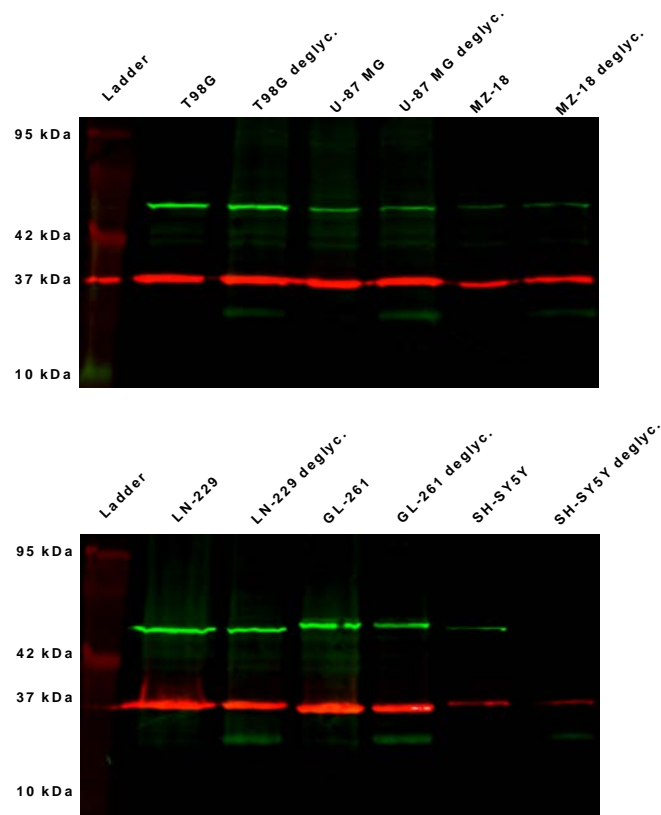


Figure 20: Western blot of deglycosylated and untreated total protein stained for TMEM158. Total protein, isolated from indicated cell lines was deglycosylated using PNGase F according to protocol from New England BioLabs, Frankfurt, Germany. Bands shown in green represent TMEM158, while red bands indicate GAPDH, which was used as loading control. Blots were stained at a 1:1500 antibody dilution against TMEM158 (ab98335) and 1:3000 against GAPDH (GA1R). Experiment was performed by Fabian Flemig¹⁵⁶.

8.5 Histograms of flow cytometry measurements of BINP and scBINP stained T98G cells at different time points after staining

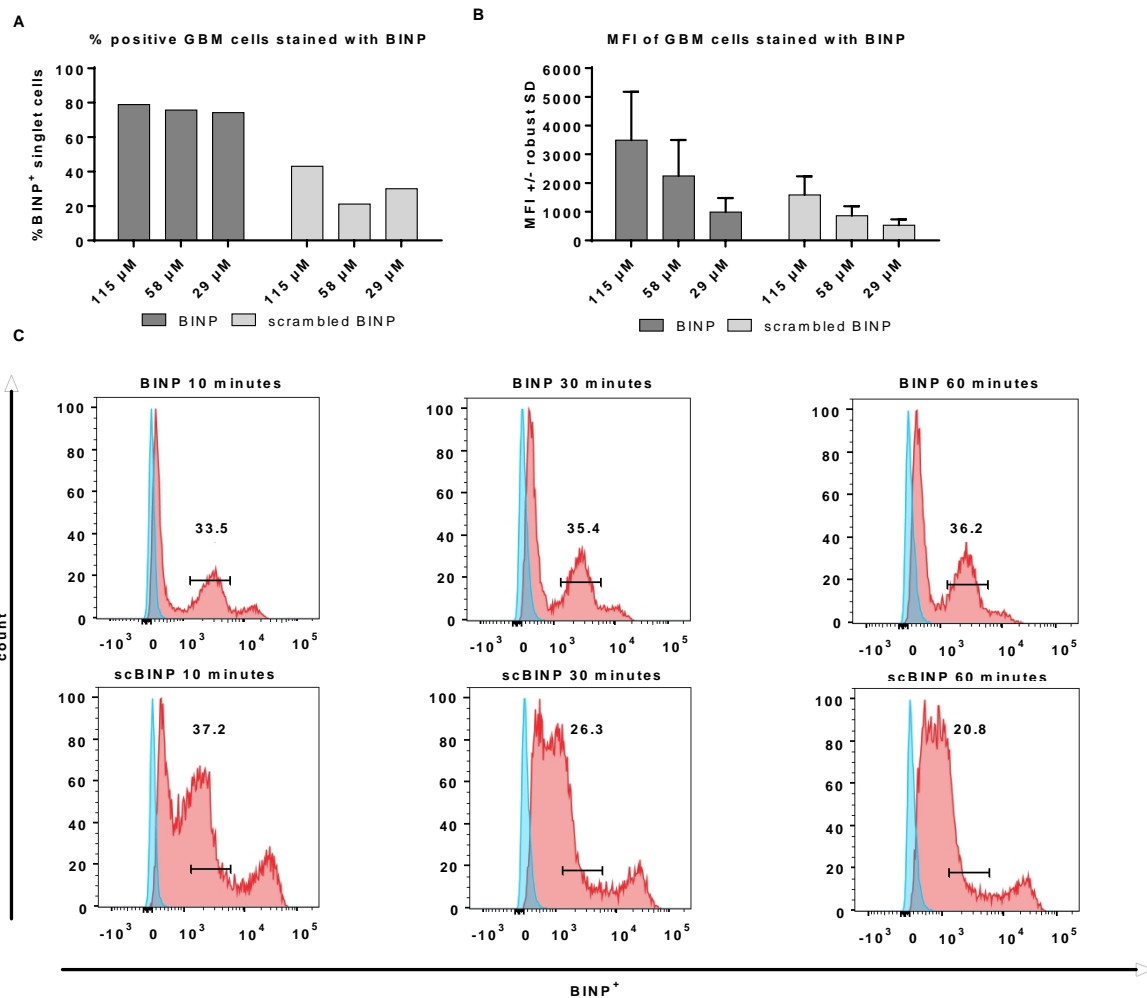


Figure 21: Titration of BINP concentration for flow cytometry staining and stability of fluorescence signal after staining. A)/B) Titration of BINP and scrambled peptide binding to T98G cells. Cells were stained with indicated concentrations of Rhodamine B labeled BINP or scrambled peptide. Shown is the percentage of positive stained T98G cells (A) and the median fluorescence intensity (MFI, B) of singlet cells. Data was measured once. **C)** Flow cytometry staining of T98G with BINP, measured at different time points. Cells were stained with either Rhodamine B-labeled BINP or -scrambled BINP (scBINP) at a concentration of 57.6 μM and measuring several times at different time points starting about 10 minutes after staining. Shown is the percentage of positive stained viable singlet T98G cells of a representative experiment.

8.6 Flow cytometry analysis of TMEM158 knockdown

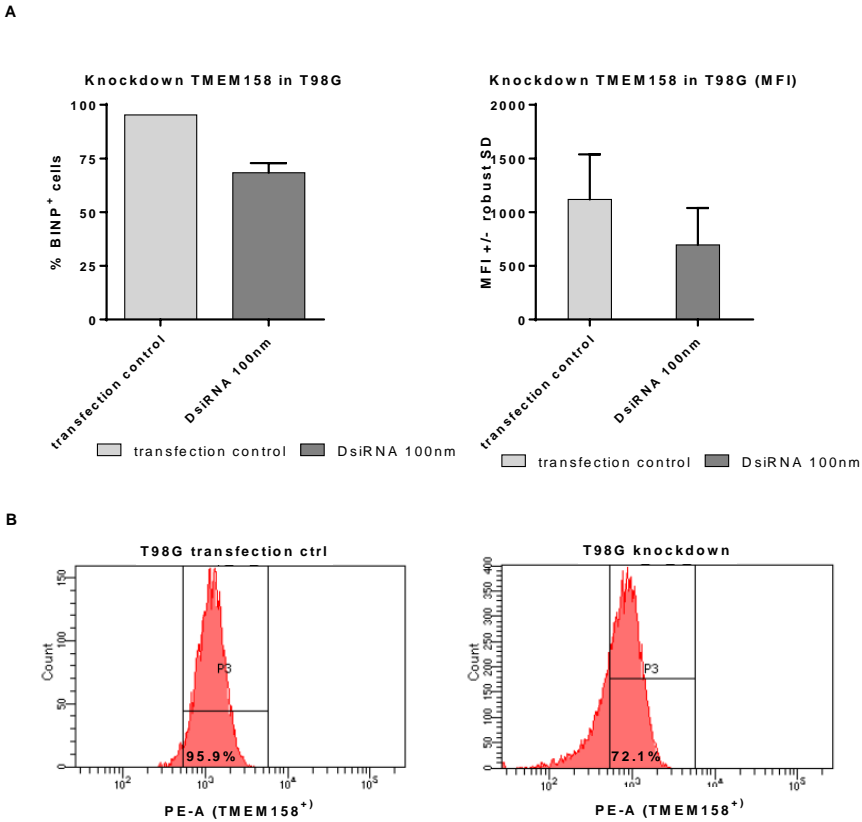


Figure 22: Flow cytometric analysis of TMEM158 knockdown. Cells were either transfected with only PEI as transfection control or PEI and 100 nM of DsiRNA against TMEM158 and stained with BINP at a concentration of 57.6 μ M. **A)** Bar graphs showing percentage (left) or MFI (right) of BINP⁺ T98G cells with and without knockdown. **B)** Histograms showing percentage of BINP⁺ T98G cells with (left) and without knockdown (right).

8.7 Cytotoxicity of BINP-WT-CAR-T cells against non-brain tumor cell lines

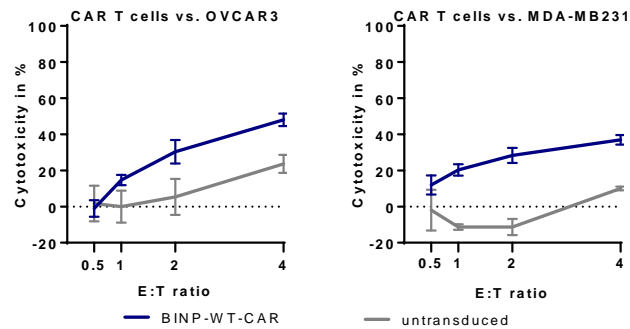


Figure 23: Cytotoxicity of BINP-WT-CAR-T cells against non-brain tumor entities. Bioluminescence of cells was measured after 24 hours of co-culture, shortly after addition of D-luciferin. Cytotoxicity was calculated from the difference of bioluminescence between wells with tumor cells only and wells containing both tumor and T cells. The ratio between T and tumor cells is designated as effector-to-target (E:T) ratio. In this experiment E:T ratios of 0.5 to 4 were analyzed. Shown is an experiment with T cells from one donor in technical triplicates. Data is presented as mean \pm SD cytotoxicity. Cytotoxicity of BINP-WT-CAR-T cells against OVCAR3 (ovarian carcinoma, left) or MDA-MB231 (triple-negative breast cancer, right) at different effector-to-target ratios. The experiment was performed by Dr. Jana Burkhardt at McMaster University, Hamilton, Canada.

8.8 Murine model of GBM and targeting by BINP-CAR-T cells

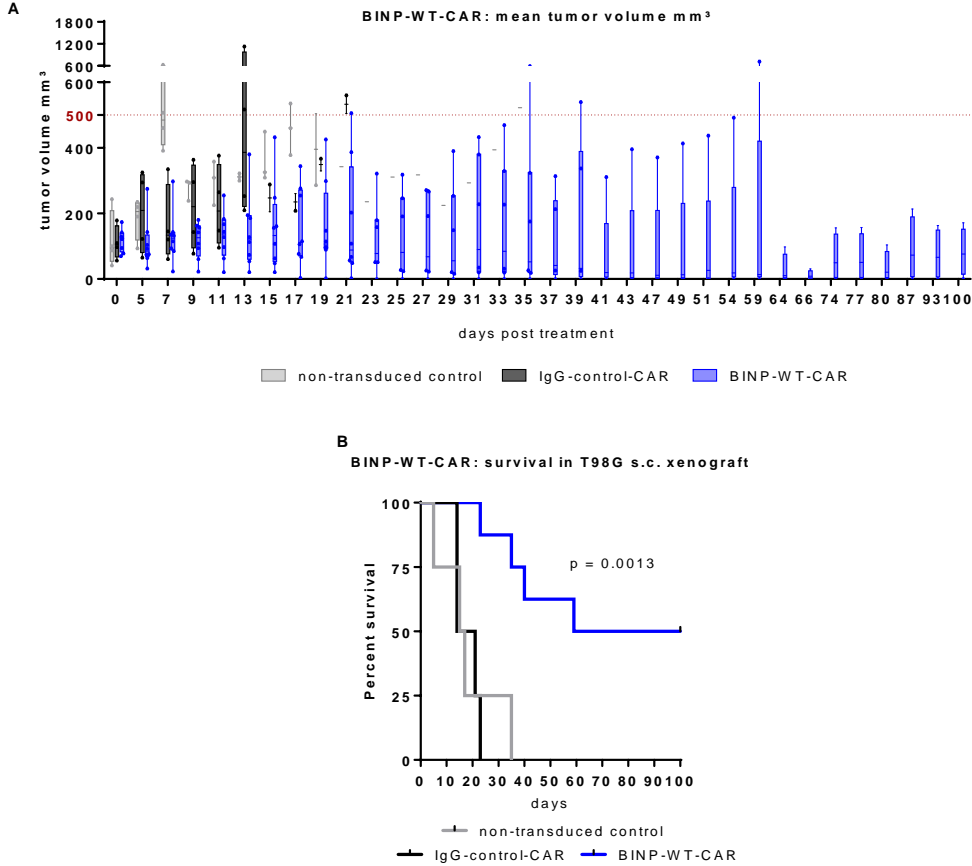


Figure 24: Function of BINP-WT-CAR-T cells in a murine glioblastoma model. A) Change of tumor volume during treatment. Shown is the mean tumor volume of NRG mice after injection of BINP-WT-CAR-T cells compared to non-transduced T cells or IgG-control-CAR-T cells. Eight mice received human BINP-WT-CAR-T cells by intratumoral application, four mice were injected with non-transduced (NT) human T cells and four mice received IgG-control-CAR-T cells from the same donor. Tumor volume was measured by caliper at indicated days. **B)** Survival was analyzed by Kaplan-Meier statistics with log-rank test. The experiment was performed by Dr. Jana Burkhardt at McMaster University, Hamilton, Canada.

8.9 Modelling of BINP binding to TMEM158

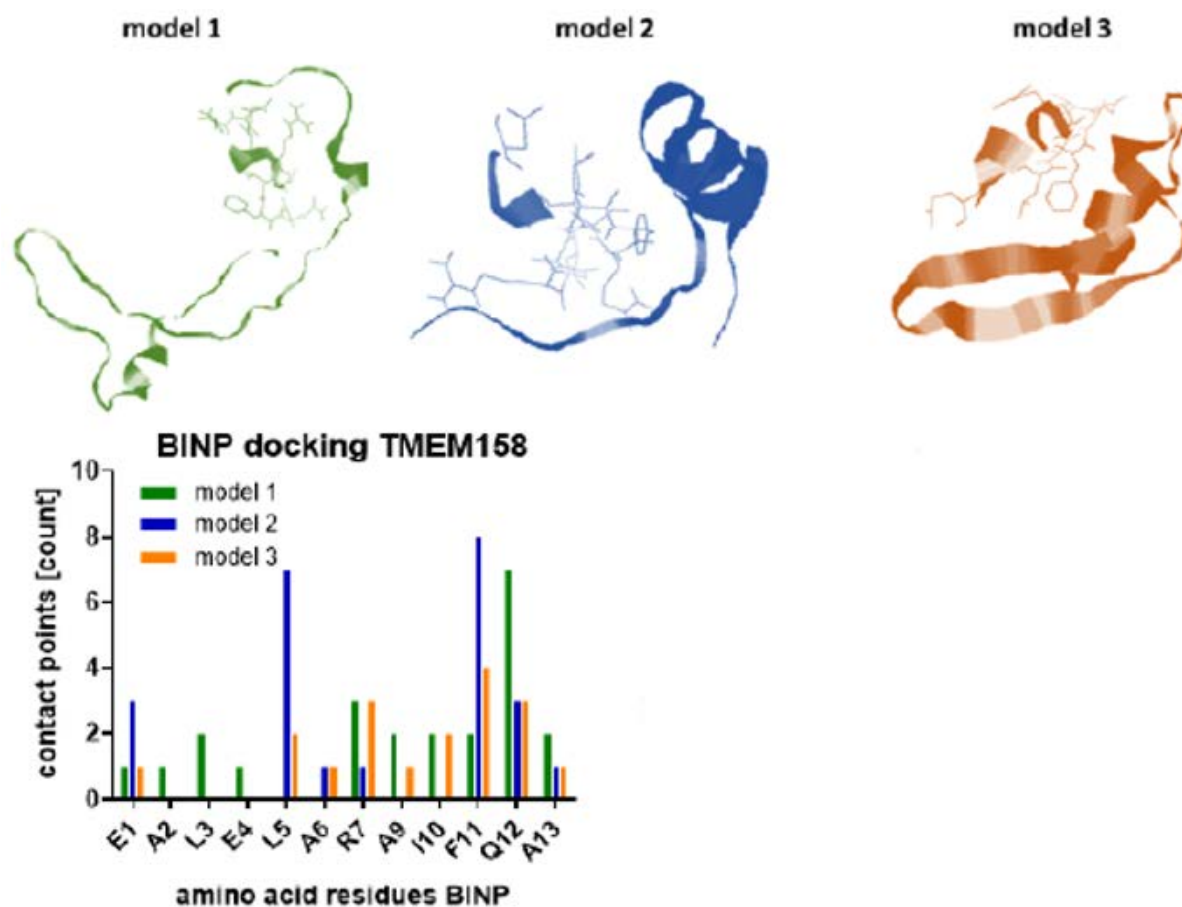


Figure 25: Modeling of BINP binding to TMEM158. The BINP model was generated using PEP-FOLD3 by Dr. Galina Denisova (McMaster University, Hamilton, Canada). Homology modeling of the extracellular domain of human TMEM158 was performed using the SWISS-MODEL workspace and repository. Docking of BINP to TMEM158 was done by ClusPro with subsequent analysis via the CSU algorithm to calculate likelihood of amino acid contacts. Shown is the molecule structure of BINP and TMEM158 when bound according to the 3 most likely models (upper illustration) or the number of contacts with TMEM158 per amino acid of BINP for each of the three binding models (lower graph).

8.11 Murine model of GBM and targeting by anti-PTPRZ1-CAR-T cells

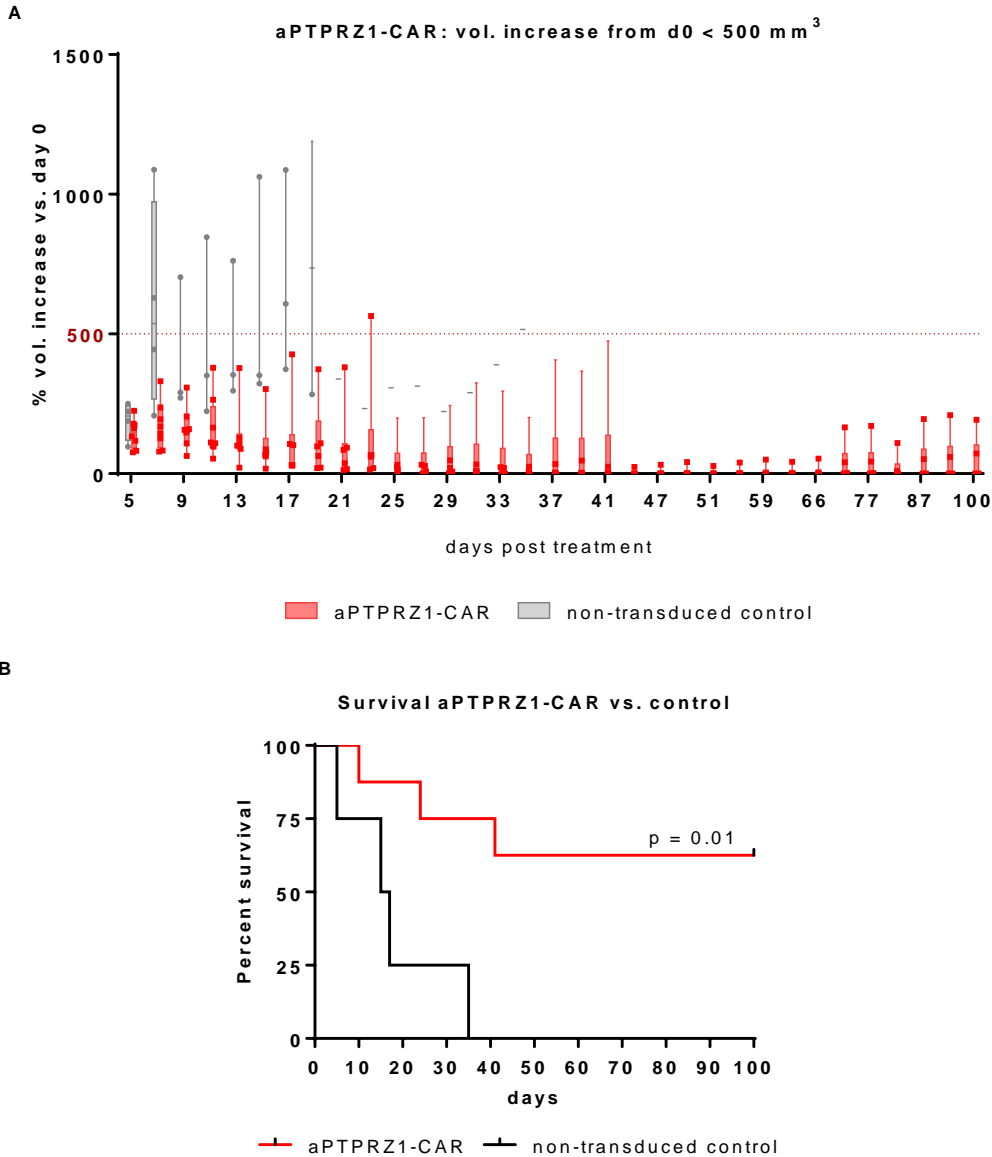


Figure 27: Function of anti-PTPRZ1-CAR-T cells in a murine glioblastoma model. A) Change of tumor volume during treatment. Shown is the mean tumor volume of NRG mice after injection of anti-PTPRZ1-CAR-T cells compared to non-transduced T cells. Eight mice per group received either human anti-PTPRZ1-CAR-T cells or non-transduced (NT) human T cells from the same donor by intratumoral application. Tumor volume was measured by caliper at indicated days. **B)** Survival was analyzed by Kaplan-Meier statistics with log-rank test. The experiment was performed by Dr. Jana Burkhardt at McMaster University, Hamilton, Canada.

9 List of Tables

Table 1: Cycling parameters for RT-qPCR	36
Table 2: Cycling parameters for site-directed mutagenesis	44

10 List of Figures

Figure 1: Structure of different CAR generations. Upper scheme: Elements of a first-generation CAR, consisting of an extracellular domain that binds to a target antigen, an intracellular domain that mediates activation of the immune cell after antigen binding and a transmembrane domain that links the extra and the intracellular domain. Lower scheme: Differences in structure of the five different CAR generations. Additional co-stimulatory domains were added to the first-generation CAR to increase proliferation and persistence of CAR cells and to protect them against the immunosuppressive tumor microenvironment to some extent. CAR, chimeric antigen receptor; CM, co-stimulatory molecule; IL-12, Interleukin-12; IL-2R β , Interleukin-2 receptor β ; ITAM, immunoreceptor tyrosine-based activation motif; JAK, Janus kinase; STAT, Signal transducer and activator of transcription¹.
..... 15

Figure 2: Isoforms of PTPRZ1 and Phosphacan. Shown is the structure of the two main transmembrane variants of PTPRZ1 as well as the two different soluble isoforms, called PTPRZ-S or phosphacan. 19

Figure 3: Predicted structure of TMEM158. Shown is a prediction of intracellular, transmembrane and extracellular domains of TMEM158 based on the sequence. The signaling peptide is highlighted in red and a possible glycosylation site is shown in green. The figure was created using the Protter webtool¹. Abbreviations: PTM, post-translational modification 23

Figure 4: Scheme and cloning of recombinant TMEM158. A) Expression cassettes of recombinant TMEM158-hFc. Shown is a scheme of the expression cassette of the extracellular part of TMEM158, fused to a human Fc-Tag. **B)** Agarose gel loaded with restriction digested plasmids for cloning of TMEM158-hFc into pCCL backbone. Indicated plasmids were cut with *Ascl* and *NheI*. Bands indicated by the red arrow were cut out of the gel using a scalpel for purification of the digested plasmids and ligation. Undigested plasmids were also loaded on the gel to determine separation of the lower border of the bands from cut and uncut plasmids as orientation for cutting out the bands. Abbreviations: EF1 α , elongation factor-1 alpha (promoter); SP, signaling peptide (TMEM158); TEV, Tobacco etch virus (protease cleavage site); hFc, human fraction crystallizable (antibody fragment) 47

Figure 5: Cloning of BINP-CAR-T constructs A) Expression cassettes of BINP-CARs. Shown are the control vectors and the second-generation CAR constructs consisting of a CD8a transmembrane domain, intracellular signaling domains of CD28 and CD3 ζ (light red) as well as the BINP-IgG4 domain (dark red) for antigen binding. The CAR-cassette was cloned into a lentiviral pCCL vector. **B)** Scheme of the BINP-CAR protein on a T cell, binding to TMEM158 on the surface of a target cell. The BINP-CAR is illustrated in red and TMEM158 is shown in blue. **C)** Agarose gel loaded with restriction digested plasmids for re-cloning of BINP-WT-CAR. Both plasmids were cut with *Ascl* and *BamHI*. Bands indicated by the red arrow were cut out of the gel using a scalpel for purification of the digested plasmids and ligation. Undigested plasmids were also loaded on the gel to determine separation of the lower border of the bands from cut and uncut plasmids as orientation for cutting out the bands. 50

Figure 6: Titration of the viral particles per μ l of concentrated supernatant on 293T cells. A log₄ dilution series of the concentrated supernatant from virus production was generated and added to individual wells of a 24-well plate, each containing 30,000 293T cells. Cells were

harvested and stained using an antibody (CD271 (LNGFR) -Viobright FITC antibody) against the Δ NGFR marker protein 48 hours after infection. **A)** Flow cytometric quantification of transduced 293T cells. Percentage of Δ NGFR⁺ cells was determined using flow cytometry. Slope and intercept of the linear part of the curve (lowest three data points in this example) were calculated by linear regression and used for calculating the number of viral particles per μ l and per ml. **B)** Formula for calculation of the number of viral particles per ml. Abbreviations: BINP, brain injury-derived neurotrophic peptide; CAR, chimeric antigen receptor; Δ NGFR, truncated p75 nerve growth factor receptor (missing large parts of the cytoplasmatic tail).... 53

Figure 7: Gene-expression of TMEM158, influence on survival and correlation with cancer stem cell marker. **A)** Comparison of TMEM158 gene-expression between low-grade glioma (LGG) (n=518), GBM (n=163) and normal brain tissue (n=207). Significance was determined by analysis of variance (ANOVA) with a p-value cut-off of 0.01 and a fold-change threshold of 2. **B)** Overall survival and **C)** Disease-free survival of GBM- and low-grade glioma patients, expressing low (< median) or high (> median) TMEM158. Hazard ratio and corresponding p-values are indicated as well. **D)** Co-expression of TMEM158 and two cancer stem cell markers. Pearson correlation between TMEM158 gene expression and either PROM1 (left) or CD44 (right) expression was calculated using data from the TCGA GBM dataset. Abbreviations: FPKM, Fragments per kilo base of transcript per million mapped fragments; HR, Hazard ratio; TPM, transcripts per million..... 57

Figure 8: Gene-expression of TMEM158 in a local cohort and differences between subgroups. TMEM158 gene-expression, measured by RT-qPCR. **A)** Comparison between GBM and normal brain tissue as well as GBM cell lines. GBM samples (n=80, including 5 grade 4 astrocytomas, formerly designated as secondary GBM) and normal brain tissue (n=10) from local patients are compared with different GBM and a neuroblastoma cell line. **B)** Comparison between indicated subgroups of the same dataset. All samples were measured in technical quadruplicates and their mean expression levels were normalized to RPL32 expression. Fold change was calculated for all Δ Ct values and are depicted as $\log_{10}(2^{\Delta C_t}) \pm SD$. **C)** Overall survival of GBM patients from the University Hospital Leipzig with high (> median expression) or low (< median expression) TMEM158 expression is illustrated as Kaplan-Maier plot. Statistical significance was calculated by log-rank test. **D)** Clinical characteristics of the patient cohort analyzed by RT-qPCR. Samples were obtained from patients during surgery and expression of Ki-67, IDH mutation- and MGMT methylation status were measured by RT-qPCR. Clinical metadata is shown as total number (Gender, Age, Location and IDH status) or as mean \pm SD (Karnofsky index, Ki-67, MGMT, OS and PFS). Gender and age of two donors of normal tissue is not included, since data was not accessible. Abbreviations: M, male; F, female; IDH, isocitrate dehydrogenase; WT, wild type; OS, overall survival; PFS, progression-free survival. 60

Figure 9: Gene-expression of PTPRZ1, influence on survival and correlation with cancer stem cell marker. **A)** Comparison of PTPRZ1 gene-expression between low-grade gliomas (LGG) (n=518), GBM (n=163) and normal brain tissue (n=207). Significance was determined by analysis of variance (ANOVA) with a p-value cut-off of 0.01 and a fold-change threshold of 2. **B)** Overall survival and **C)** Disease-free survival of GBM- and low-grade glioma patients, expressing low (< median) or high (> median) PTPRZ1. Hazard ratio (HR) and corresponding p-values are indicated as well. **D)** Co-expression of PTPRZ1 and two cancer stem cell markers. Pearson correlation between PTPRZ1 gene-expression and either PROM1 (left) or CD44 (right) expression was calculated using data from the TCGA GBM dataset. Abbreviations: FPKM, Fragments per kilo base of transcript per million mapped fragments; HR, Hazard ratio; TPM, transcripts per million. 61

Figure 10: Gene-expression of PTPRZ1 in a local cohort and differences between subgroups. PTPRZ1 gene-expression was measured by RT-qPCR. **A)** mRNA expression in

GBM samples (n=80, including 5 grade 4 astrocytomas, formerly designated as secondary GBM) and normal brain tissue (n=10) from local patients are compared with different GBM and a neuroblastoma cell line. **B)** Comparison between indicated subgroups of the same dataset. All samples were measured in technical quadruplicates and their mean expression levels were normalized to *RPL32* expression. Fold change was calculated for all ΔCt values and are depicted as $\log_{10}(2^{\Delta Ct}) \pm SD$. **C)** Overall survival of local GBM patients from the University Hospital Leipzig with high (> median expression) or low (< median expression) *TMEM158* expression is illustrated as Kaplan-Maier plot. Statistical significance was calculated by log-rank test. 63

Figure 11: Protein expression and knockdown of TMEM158 in different cell lines. A) Western blot analysis of TMEM158 in GBM cell lines and the neuroblastoma cell line SH-SY5Y. Blots were stained at a 1:1500 antibody dilution against TMEM158 (ab98335) and 1:3000 against GAPDH (GA1R). Bands shown in green represent TMEM158, while red bands indicate GAPDH, which was used as loading control. **B)** DsiRNA knockdown of TMEM158. T98G cells were either transfected with only PEI as control or PEI and 100 nM of DsiRNA directed against TMEM158. Signal intensities were determined densitometrically and are written above the corresponding band in relative intensities (top). The ratio of both fluorescence intensities was calculated and is shown in the lower graph (N=1). Abbreviations: DsiRNA, double stranded small interfering RNA; GAPDH, Glyceraldehyde 3-phosphate dehydrogenase; GBM, glioblastoma; PEI, polyethylenimine; TMEM158, transmembrane protein 158. 64

Figure 12: Flow cytometry analysis of BINP binding to TMEM158. A) - C) BINP binding to different GBM and non-GBM cell lines. Cells were stained with BINP at a concentration of 57.6 μM . Cells stained with a scrambled version of BINP served as control. Shown is the percentage of positive stained T98G cells (A), MFI (B) of Rhodamine B-positive cells (PE channel) or histograms (C) of life singlet cells. Data is illustrated as mean \pm SD and was measured in biological triplicates, except for the staining of U-87 MG and SH-SY5Y with scrambled BINP, which was measured in biological duplicates (A/B). Histograms show one representative example of the performed experiments (C). **D)** Gating of T98G cells stained with BINP. Cells were stained with BD Horizon™ Fixable Viability Stain 450 for exclusion of dead cells and Rhodamine-B labeled BINP at a concentration of 115.2 μM . Cell debris and larger cell conglomerates were excluded by the gate shown in the upper left picture. Doublet cells (upper right) and dead cells (lower left) were excluded as well. Living singlet cells were analyzed as shown in the histogram (lower right). Shown is one representative example of samples analyzed in A) – C). Abbreviations: FSC, forward scatter; MFI, median fluorescence intensity; PE, Phycoerythrin; SSC, side scatter. 68

Figure 13: Flow cytometry analysis of integrin $\alpha V\beta 3$ in GBM cells and in cells from a neuroblastoma cell line. Shown is the percentage of positive stained cells (left) and the median fluorescence intensity (MFI, right) of singlet cells. Data was measured two times with technical duplicates each and is illustrated as mean \pm SD. 69

Figure 14: Size and binding of recombinant TMEM158. A) Western Blot of recombinant TMEM158 protein. The protein was produced in HEK293T cells and purified using magnetic protein A beads, which bind the hFc part. Bands shown in green represent recombinant TMEM158, while red bands indicate GAPDH, which was used as loading control. **B)** Binding of BINP to recombinant TMEM158-hFc. Proteins were immobilized on high-binding polystyrene plates overnight and stained with Rhodamine B-labeled BINP or -scrambled (sc) BINP on the following day. Fluorescence intensity was measured in technical triplicates and is shown as mean \pm SD at indicated (sc)BINP concentrations. The BINP and scBINP curves were normalized by subtracting the negative control curve (no immobilized TMEM158 protein). Three independent experiments were performed and are shown as individual graphs (upper,

middle and lower row). Abbreviations: hFc, human fraction crystallizable (antibody fragment).
..... 70

Figure 15: Transduction rates of BINP-CAR-T cells A) – C) Transduction rates of CAR- and control-T cells. T cells were transduced at an MOI of 4, except for the BINP-F11A-CAR-T cells of donor 2, which was transduced at MOI 3.5 because of a low virus titer. Cells of each group were stained with an antibody (CD271 (LNGFR) -Viobright FITC antibody) against the Δ NGFR protein, which is co-expressed with the CARs and served as detection marker. Percentage of cells positive for the Δ NGFR was determined by flow cytometry (numbers depicted in each graph). Cells from donor 1 (A/B) and 2 (C) are shown as histograms. Abbreviations: aHER2, anti-human epidermal growth factor receptor 2; BINP, brain injury-derived neurotrophic peptide; CAR, chimeric antigen receptor; Δ NGFR, truncated p75 nerve growth factor receptor (missing large parts of the cytoplasmatic tail). 73

Figure 16: Cytotoxicity of BINP-CAR-T cells A) Cytotoxicity of BINP-CAR-T cells from donor 1 (transduction rates see Fig. 15A) against T98G at different time points and different effector-to-target ratios. Bioluminescence of cells was measured at indicated time points, shortly after addition of D-luciferin. Cytotoxicity was calculated from the difference of bioluminescence between wells with tumor cells only and wells containing both tumor- and T cells. The ratio between T- and tumor cells is designated as effector-to-target (E:T) ratio. In this experiment E:T ratios of 0.5 to 8 were analyzed. Shown is an experiment with T cells from one donor in technical triplicates. Data is presented as mean \pm SD cytotoxicity. **B) / C)** Cytotoxicity of BINP-CAR-T cells from donor 1 (B, transduction rates see Fig. 15B) or from donor 2 (C, transduction rates see Fig. 15C) against the GBM cell lines T98G and U-87 MG and towards the neuroblastoma cell line SH-SY5Y. T cells and tumor cells were co-cultivated at E:T ratios of 0.5 to 4. Bioluminescence of cells was measured at indicated time points, shortly after addition of D-luciferin. Shown is one of two experiments performed with cells from different donors in technical triplicates. Data is shown as mean \pm SD cytotoxicity. Statistical significance was calculated by Tukey's multiple comparison test and are illustrated as * for p<0.05, ** for p<0.01, *** for p<0.001, **** for p<0.0001 for comparison of a group with the pCCL-control or as Δ for p<0.05, $\Delta\Delta$ for p<0.01, $\Delta\Delta\Delta$ for p<0.001, $\Delta\Delta\Delta\Delta$ for p<0.0001 for comparison of a group with the BINP-WT-CAR. Due to lack of space, significance is only depicted for selected conditions. 78

Figure 17: Genetic maps of vectors used for production of lentiviral particles. The vectors encode the genes for production of infectious but replication deficient viral particles, namely HIV-1 gag and -pol (pMDLg/pRRE), as well as Rev (pRSV-Rev). The produced viral particles are pseudotyped by the VSV-G envelope, encoded on the pMD2.G vector. Maps were downloaded from www.addgene.org. Abbreviations: AmpR, Ampicillin resistance; CAP, catabolite activator protein; CMV, cytomegalovirus; cPPT/CTS, central polypurine tract/central termination sequence; HIV-1, human immunodeficiency virus 1; lac, lactose (promoter/operator); ori, origin of replication, RRE, Rev response element; RSV, respiratory syncytial virus; VSV-G, vesicular stomatitis virus glycoprotein G..... 113

Figure 18: Expression of TMEM158 and PTPRZ1 in brain tumor entities and survival of GBM patients. A)/B) Expression of TMEM158 (A) or PTPRZ1 (B) in different brain tumor entities is shown. Illustrated are sub-cohorts of TCGA datasets including clinical subtype for astrocytoma (n=197), oligoastrocytoma (n=134) and oligodendroglioma (n=198). In addition, neuroblastoma (NBL) samples from the TARGET panel and from the TCGA (GBM/LGG), as well as from paraganglioma (PCPG) datasets are shown. Gene expression values are depicted as log₁₀-transformed and means \pm 95 % confidence intervals (CI). Statistical significance was determined by a T-test. The analysis was performed by Dr. Jana Burkhardt. **C/D)** Overall survival of GBM patients, expressing low (< median) or high (> median) of the TMEM158 (C) or PTPRZ1 (D). Hazard ratio and corresponding p-values are indicated as well..... 114

Figure 19: Western Blot of GBM and non-GBM cell lines stained for TMEM158 and GAPDH. Bands shown in green represent TMEM158, while red bands indicate GAPDH, which was used as loading control. Blots were stained with either 1:1500 (left) or 1:3000 (right) dilution of the anti-TMEM158 antibody (ab98335). 115

Figure 20: Western blot of deglycosylated and untreated total protein stained for TMEM158. Total protein, isolated from indicated cell lines was deglycosylated using PNGase F according to protocol from New England BioLabs, Frankfurt, Germany. Bands shown in green represent TMEM158, while red bands indicate GAPDH, which was used as loading control. Blots were stained at a 1:1500 antibody dilution against TMEM158 (ab98335) and 1:3000 against GAPDH (GA1R). Experiment was performed by Fabian Flemig¹⁵⁶. 116

Figure 21: Titration of BINP concentration for flow cytometry staining and stability of fluorescence signal after staining. A/B) Titration of BINP and scrambled peptide binding to T98G cells. Cells were stained with indicated concentrations of Rhodamine B labeled BINP or scrambled peptide. Shown is the percentage of positive stained T98G cells (A) and the median fluorescence intensity (MFI, B) of singlet cells. Data was measured once. **C) Flow cytometry staining of T98G with BINP, measured at different time points.** Cells were stained with either Rhodamine B-labeled BINP or -scrambled BINP (scBINP) at a concentration of 57.6 μ M and measuring several times at different time points starting about 10 minutes after staining. Shown is the percentage of positive stained viable singlet T98G cells of a representative experiment. 117

Figure 22: Flow cytometric analysis of TMEM158 knockdown. Cells were either transfected with only PEI as transfection control or PEI and 100 nM of DsiRNA against TMEM158 and stained with BINP at a concentration of 57.6 μ M. **A) Bar graphs showing percentage (left) or MFI (right) of BINP⁺ T98G cells with and without knockdown.** **B) Histograms showing percentage of BINP⁺ T98G cells with (left) and without knockdown (right).** 118

Figure 23: Cytotoxicity of BINP-WT-CAR-T cells against non-brain tumor entities. Bioluminescence of cells was measured after 24 hours of co-culture, shortly after addition of D-luciferin. Cytotoxicity was calculated from the difference of bioluminescence between wells with tumor cells only and wells containing both tumor and T cells. The ratio between T and tumor cells is designated as effector-to-target (E:T) ratio. In this experiment E:T ratios of 0.5 to 4 were analyzed. Shown is an experiment with T cells from one donor in technical triplicates. Data is presented as mean \pm SD cytotoxicity. Cytotoxicity of BINP-WT-CAR-T cells against OVCAR3 (ovarian carcinoma, left) or MDA-MB231 (triple-negative breast cancer, right) at different effector-to-target ratios. The experiment was performed by Dr. Jana Burkhardt at McMaster University, Hamilton, Canada..... 119

Figure 24: Function of BINP-WT-CAR-T cells in a murine glioblastoma model. A) Change of tumor volume during treatment. Shown is the mean tumor volume of NRG mice after injection of BINP-WT-CAR-T cells compared to non-transduced T cells or IgG-control-CAR-T cells. Eight mice received human BINP-WT-CAR-T cells by intratumoral application, four mice were injected with non-transduced (NT) human T cells and four mice received IgG-control-CAR-T cells from the same donor. Tumor volume was measured by caliper at indicated days. **B) Survival was analyzed by Kaplan-Meier statistics with log-rank test.** The experiment was performed by Dr. Jana Burkhardt at McMaster University, Hamilton, Canada. 120

Figure 25: Modeling of BINP binding to TMEM158. The BINP model was generated using PEP-FOLD3 by Dr. Galina Denisova (McMaster University, Hamilton, Canada). Homology modeling of the extracellular domain of human TMEM158 was performed using the SWISS-MODEL workspace and repository. Docking of BINP to TMEM158 was done by ClusPro with subsequent analysis via the CSU algorithm to calculate likelihood of amino acid contacts. Shown is the molecule structure of BINP and TMEM158 when bound according to the 3 most

likely models (upper illustration) or the number of contacts with TMEM158 per amino acid of BINP for each of the three binding models (lower graph). 121

Figure 26: Alignment of the human, the rat and the murine TMEM158 protein sequence.

Human protein sequence of TMEM158 was aligned with the corresponding murine and rat sequence using Clustal Omega²⁰⁷. Protein sequences from Uniprot²⁰⁸ were used for the alignment. Shown are the individual amino acids predicted to be involved in binding between TMEM158 and BINP, according to 3 calculated *in silico* models (red, blue or underlined). Homology of all 3 organisms is indicated by asterisk below each individual amino acid. 122

Figure 27: Function of anti-PTPRZ1-CAR-T cells in a murine glioblastoma model. A)

Change of tumor volume during treatment. Shown is the mean tumor volume of NRG mice after injection of anti-PTPRZ1-CAR-T cells compared to non-transduced T cells. Eight mice per group received either human anti-PTPRZ1-CAR-T cells or non-transduced (NT) human T cells from the same donor by intratumoral application. Tumor volume was measured by caliper at indicated days. **B)** Survival was analyzed by Kaplan-Meier statistics with log-rank test. The experiment was performed by Dr. Jana Burkhardt at McMaster University, Hamilton, Canada. 123

11 Declaration of independent work

Erklärung über die eigenständige Abfassung der Arbeit

Hiermit erkläre ich, dass ich die vorliegende Arbeit selbstständig und ohne unzulässige Hilfe oder Benutzung anderer als der angegebenen Hilfsmittel angefertigt habe. Ich versichere, dass Dritte von mir weder unmittelbar noch mittelbar eine Vergütung oder geldwerte Leistungen für Arbeiten erhalten haben, die im Zusammenhang mit dem Inhalt der vorgelegten Dissertation stehen, und dass die vorgelegte Arbeit weder im Inland noch im Ausland in gleicher oder ähnlicher Form einer anderen Prüfungsbehörde zum Zweck einer Promotion oder eines anderen Prüfungsverfahrens vorgelegt wurde. Alles aus anderen Quellen und von anderen Personen übernommene Material, das in der Arbeit verwendet wurde oder auf das direkt Bezug genommen wird, wurde als solches kenntlich gemacht. Insbesondere wurden alle Personen genannt, die direkt an der Entstehung der vorliegenden Arbeit beteiligt waren. Die aktuellen gesetzlichen Vorgaben in Bezug auf die Zulassung der klinischen Studien, die Bestimmungen des Tierschutzgesetzes, die Bestimmungen des Gentechnikgesetzes und die allgemeinen Datenschutzbestimmungen wurden eingehalten. Ich versichere, dass ich die Regelungen der Satzung der Universität Leipzig zur Sicherung guter wissenschaftlicher Praxis kenne und eingehalten habe.

.....

Datum

.....

Unterschrift

13 List of publications

Paper (in preparation):

Christoph Bach, Fabian Flemig, Galina Denisova, Christopher Baker, Holger Kirsten, Wolf Müller, Jürgen Meixensberger, Jonathan Bramson, Jana Burkhardt, Frank Gaunitz (2023): “Development of a CAR-T-cell therapy, targeting TMEM158 for treatment of glioblastoma”

Jana Burkhardt*, Christoph Bach*, Carla Lotta Mertineit, Galina Denisova, Christopher Baker, Holger Kirsten, Wolf Müller, Jürgen Meixensberger, Jonathan Bramson, Frank Gaunitz (2023): “Development of CAR-T cells targeting PTPRZ1 for treatment of glioblastoma”

*: these authors contributed equally

Poster:

Christoph Bach, Daniela Rudolf, Galina Denisova, Jonathan Bramson, Jana Burkhardt (2018): “New neuronal lineage tumor antigen and therapeutic targeting thereof”; Immuno-Oncology Summit Europe, London